Silicon Photonic Mach-Zehnder Modulator Architectures for High Order Modulation Formats

Alireza Samani

Department of Electrical & Computer Engineering

McGill University, Montreal, Canada

December 2018

A thesis submitted to McGill University in partial fulfillment of the requirements for the degree of Doctor of Philosophy in Electrical Engineering

Abstract

Global internet traffic has been growing exponentially in the past several years. This increase is fueled by video streaming services (e.g. Netflix, YouTube), cloud-based storages (e.g. Dropbox, google drive), and machine-to-machine (e.g. Internet of Things) applications. Since 2008 most Internet traffic has originated or been terminated in datacenters and the datacenter traffic is forecasted to grow three-fold in the next five years to reach 20.6 zettabytes by 2021.

On-Off-Keying (OOK) has been the main modulation format employed in short reach optical interconnects. The simplicity of the transmitter and receiver architectures have been an important factor in the success of OOK for short reach optical links. Recently deployed, 100 Gb/s systems utilize OOK modulation in 4 × 25 Gb/s configuration. However, as we move towards 400 Gb/s and 1 Tb/s systems, OOK requires a proportional increase in the bandwidth. Hence, a more efficient modulation format is required to avoid such complexity.

Silicon photonics (SiP) has recently become a popular choice for datacenter interconnects. Taking advantage of years of complementary metal oxide semiconductor research and development, SiP provides a low cost and high yield platform for datacenter optical interconnects.

In this thesis, 3 different SiP Mach-Zehnder modulator (MZM) structures to generate higher order modulation formats are presented. First, the feasibility of utilizing coherent transmission systems as opposed to intensity modulation/direct detection systems for 400 Gb/s and 1 Tb/s systems are discussed and an Inphase-Quadrature modulator is presented. We discuss the advantages and disadvantages of using coherent systems for short reach applications.

Next, we investigate and compare the performance advantages of generating 4-level Pulse Amplitude Modulation (PAM-4) using various structures of MZM optically, instead of generating PAM-4 in the electrical domain using digital to analog convertors (DACs) for 400 Gb/s systems. The two variants of optical-DACs are a Dual Parallel Mach-Zehnder modulator (DP-MZM) with one series push pull travelling wave MZM on each arm and a single MZM having two electrodes in series that we name Multi-Electrode MZM (ME-MZM). We present the optical design of the modulators and investigate the effects of non-linearities of the MZM transfer function and PN junction phase-shifters on performance of the PAM-4 generation. Then, the DC, small signal and large signal characterization of each modulator are presented. We parametrically examine the transmission performance of each modulator and present an optimized modulator design for optical generation and transmission of 112 Gb/s PAM-4 without using digital signal processing.

Résumé

Le trafic IP mondial a connu une croissance exponentielle au cours des dernières années. Cette augmentation est alimentée par les services de streaming vidéo (Netflix, YouTube par exemple), les solutions de stockage en nuage (Dropbox, Google Drive par exemple) et les applications de machine à machine (par exemple, l'Internet des objets). Depuis 2008, la majeure partie du trafic Internet provient ou se termine dans des centres de données, et ce trafic devrait être multiplié par trois au cours des cinq prochaines années pour atteindre 20,6 zettaoctets d'ici 2021.

Le On-Off-Keying (OOK) est le principal format de modulation employé dans les interconnexions optiques à courte portée. La simplicité de l'architecture de l'émetteur et du récepteur a été un facteur important dans le succès du format OOK pour les liens optiques à courte portée. Les systèmes 100 Gb/s récemment déployés utilisent la modulation OOK dans une configuration 4 × 25 Gb/s. Cependant, au fur et à mesure que nous nous rapprochons des systèmes à 400 Gb/s et 1 Tb/s, le format OOK exige une augmentation proportionnelle de la bande passante. Par conséquent, un format de modulation plus efficace est nécessaire pour éviter une telle complexité.

La photonique sur silicium (SiP) est récemment devenue un choix populaire pour les interconnexions de centres de données. Tirant parti de nombreuses années de recherche et de développement sur les semi-conducteurs à oxydes métalliques, la technologie SiP constitue une plate-forme à faible coût et à haut rendement pour les interconnexions optiques de centres de données.

Dans cette thèse, 3 différentes structures de modulateur Mach-Zehnder (MZM) sur la plate-forme SiP permettant de générer des formats de modulation d'ordre supérieur sont présentées. Premièrement, la possibilité d'utiliser des systèmes de transmission cohérents pour des systèmes à 400 Gb/s et 1 Tb/s, par opposition aux systèmes à modulation d'intensité et détection directe, est discutée et un modulateur En-phase-Quadrature est présenté. Nous discutons des avantages et des inconvénients de l'utilisation de systèmes cohérents pour des applications à courte portée.

Ensuite, nous étudions et comparons les avantages en termes de performance de la génération de modulation d'amplitude d'impulsion à 4 niveaux (PAM-4) à l'aide de diverses structures de MZM dans le domaine optique, par opposition à la génération de signaux PAM-4 dans le domaine électrique à l'aide de convertisseurs numérique-analogique (DAC), pour les systèmes à 400 Gb/s. Les deux variantes de DAC optiques sont un modulateur Mach-Zehnder double-parallèle (DP-MZM) avec MZM à onde progressive de type series-push-pull dans chaque bras, et un seul MZM doté de deux électrodes en série que nous appelons MZM multi-électrodes (ME-MZM). Nous présentons la conception optique des modulateurs et examinons les effets des non-linéarités de la fonction de transfert du MZM et des modulateurs de phase à jonction PN sur la performance de la génération du format PAM-4. Ensuite, la caractérisation en courant continu, à faible signal et à large signal de chaque modulateur est présentée. Nous examinons de manière paramétrique les performances en transmission de chaque modulateur et présentons un design de modulateur optimisé pour la génération et la transmission optique de 112 Gb/s PAM-4 sans traitement numérique du signal.

Acknowledgements

First and foremost, I would like to express my sincere and utmost gratitude to my supervisor, Professor David Plant for his guidance and supervision during my Master's and PhD studies in Photonic Systems Group. Besides all the insightful technical advice and guidance, he provided us with an environment that stimulates innovation and gave us opportunities to work with world class scientist and engineers. David, thank you for your patience, your optimism and for believing in me. I truly grew in your lab, your kind nature and encouragement changed my temperament and my outlook, and I am always grateful for that. Thank you for all you have done for me, and I hope someday I can follow in your steps and have a positive impact on so many lives.

I would like to thank Dr. Michael Ayliffe for the guidance and encouragements he provided me during my research projects and my internship at Lumentum. His positive attitude and outlook, truly inspired me. No words can express what I have learned from him. I would also like to extend my thanks to Professor Lukas Chrostowski, I am grateful for his efforts on building the SiEPIC program and giving me the opportunity to be part of a growing and successful program.

I would also like to thank my colleagues. Eslam El-Fiky, thank you for being a friend I could always count on, a critic that always helped me improve, and a partner that was always there when I needed help with experiments. Maxime Jacques, working with you was one of the most pleasant experiences of my graduate studies. Thank you for being my dragon boat partner, hockey critic, and maple syrup supplier. Your work ethics, open-mindedness, and dedication are truly unique, and I have no doubt you will go on to do great things. Eslam and Maxime, it was a pleasure and an honor to spend this time with you and I hope our path will reunite again.

I would like to thank my colleagues David Patel, Mohamed Osman and Mathieu Chagnon for all their support along the way, during the experiments and tape-out deadlines. Mathieu, I am sincerely thankful for all the advice you gave me and long nights you spent with me in the lab. You are truly the best engineer I have ever had the pleasure of working with. I cannot skip other colleagues that helped me along the way: Farhad Shokraneh, Thang Hoang, Rui Li, Yannick D'Mello, Oscar Wang, Venkat Veerasubramanian, Nicolas Abadia, Ghulam Saber, Reza Nazemi, and Amar Kumar. To the new crew, Olivier Carpentier, thank you for all your support in the last few months of my studies. I am always amazed by how bright you are, keep up the good work and I hope we stay connected.

I am immensely grateful to my family for their support and love. I would like to express my deep appreciation and pay humble respects to my parents Saeideh Setoudeh and Dr. Nozar Samani for their support and guidance since my early years at school. This journey would never have been possible without your sacrifice, unconditional support and prayers. Thank you for believing in me, and for advice on research and life, and thank you for always reviewing my papers, thesis and proposals. You made me grow, you made me learn. Pedram, I am lucky to have a supportive and loving brother like you. Thank you for always paving the way for me. Living with you and going to McGill with you was the best part of this journey. Last but not least, Nicole, you have been and always will be the catalyst in my life, you are an essential element of my happiness. Thank you for your limitless support and love and for being there to help me through hard times. Thank you all, I love you unconditionally.

Associated Publications

This thesis represents my original research, and it has not been submitted for a degree or diploma at any other institution. As evidence of my original research and contributions to the existing body of knowledge, my Ph.D. work has currently resulted in 8 first-authored publications, comprising five journal articles [1–5] including one invited paper, and two refereed conference proceedings [7,8]. In addition, I also have 12 co-authored journal papers [9-13] and 7 co-authored conference proceedings [14-19] through the collaboration with my colleagues in the Photonic Systems Group at McGill University, and other industrial and academic institutions.

Journal Articles Directly Related to This Thesis

1. **A. Samani**, V. Veerasubramanian, E. El-Fiky, D. Patel and D. V. Plant, "A Silicon Photonic PAM-4 Modulator Based on Dual-Parallel Mach–Zehnder Interferometers," *IEEE Photonics Journal*, vol. 8, no. 1, pp. 1-10, Feb. 2016.

   I conceived the idea, performed the simulation and analysis, conducted the experiments, and wrote the paper. The co-authors contributed in revising the manuscript.

2. **A. Samani*,** D. Patel*, M. Chagnon, E. El-Fiky, R. Li, M. Jacques, N. Abadía, V. Veerasubramanian and D. Plant, "Experimental parametric study of 128 Gb/s PAM-4

transmission system using a multi-electrode silicon photonic Mach Zehnder modulator", *Optics Express*, vol. 25, no. 12, p. 13252, 2017.

D. Patel and I conceived the idea and contributed equally in the design and simulation of the device. Together we built the experimental setup and performed the characterization of the device and the transmission experiment. I wrote the manuscript. The other co-authors contributed in editing the paper and discussing the idea.

3. **A. Samani**, E. El-Fiky, M. Osman, R. Li, D. Patel, T. Hoang, M. Jacques, M. Chagnon, N. Abadía, and D. Plant, "Silicon Photonic Mach-Zehnder Modulator Architectures for on Chip PAM-4 Signal Generation and Transmission" *Journal of Lightwave Technology*, (Submitted, Manuscript ID: JLT-22637-2018, July 4th, 2018). (**Invited**).

   I conceived the idea, performed the simulation and analysis of the devices presented and conducted the experiments, and wrote the paper. Other authors contributed by developing the digital signal processing and discussing the idea.

4. **A. Samani**, E. El-Fiky, M. Osman, D. Patel, M. Jacques, R. Li, D. Plant. "180 Gb/s Single Carrier Single Polarization 16-QAM Transmission using an O-Band Silicon Photonic IQM" *Optics Express*, (Submitted, Manuscript ID: 346077, September 30th, 2018).

   I conceived the idea, performed the numerical analysis and the experiments, and wrote the paper. The co-authors contributed in discussing the idea, building the coherent test bed for the experiment and revising the manuscript.

5. **A. Samani**, M. Chagnon, D. Patel, V. Veerasubramanian, S. Ghosh, M. Osman, Q. Zhong and D. Plant, "A Low-Voltage 35-GHz Silicon Photonic Modulator-Enabled 112-Gb/s Transmission System", *IEEE Photonics* Journal, vol. 7, no. 3, pp. 1-13, 2015.

I conceived the idea, performed the simulation and analysis of the device and conducted the experiments, and wrote the paper. Other authors contributed by developing the digital signal processing and discussing the idea.

Conference Proceedings Directly Related to This Thesis

6. **A. Samani**, M. Chagnon, E. Elfiky, D. Patel, M. Jacques, V. Veerasubramanian, and D. Plant, "Silicon Photonics Modulator Architectures for Multi-Level Signal Generation and Transmission," 2017 Optical Fiber Communications Conference and Exposition (OFC), paper Tu2H.4. Los Angeles, CA, USA. (**Top Scored**).

   I conceived the idea, performed the design and analysis of the devices presented and conducted the experiments, and wrote the paper. Other authors contributed by developing the digital signal processing and discussing the idea.

7. **A. Samani**, D. Patel, S. Ghosh, V. Veerasubramanian, Q. Zhong, W. Shi, D. V Plant, "OOK and PAM optical modulation using single drive push pull silicon Mach-Zehnder modulator", International Group IV Photonics Conference, 27 – 29 August 2014, Paris, France.

   I conceived the idea, performed the design and analysis of the devices presented and conducted the experiments, and wrote the paper. Other authors contributed building the experimental setup and contributing to the experimental work.

Journal Articles Not Directly Related to This Thesis

8. D. Patel*, **A. Samani***, V. Veerasubramanian, S. Ghosh and D. V. Plant, "Silicon Photonic Segmented Modulator-Based Electro-Optic DAC for 100 Gb/s PAM-4 Generation," *IEEE Photonics Technology Letters*, vol. 27, no. 23, pp. 2433-2436, Dec.1, 1 2015.
9. M. Jacques, **A. Samani**, D. Patel, E. El-Fiky, M. Morsy-Osman, T. Hoang, M. Saber, L. Xu, J. Sonkoly, M. Ayliffe and D. Plant, "Modulator material impact on chirp, DSP, and performance in coherent digital links: comparison of the lithium niobate, indium phosphide, and silicon platforms", *Optics Express*, vol. 26, no. 17, p. 22471, 2018.
10. Z. Xing, **A. Samani**, M. Xiang, E. El-Fiky, T. Hoang, D. Patel, R. Li, M. Qiu, M. Saber, M. Morsy-Osman and D. Plant, "100 Gb/s PAM4 transmission system for datacenter interconnects using a SiP ME-MZM based DAC-less transmitter and a VSB self-coherent receiver", *Optics Express*, vol. 26, no. 18, p. 23969, 2018.
11. E. El-Fiky, M. Osman, **A. Samani**, C. Gamache, M. Ayliffe, J. Li, M. Jacques, Y. Wang, A. Kumar and D. Plant, "First demonstration of a 400 Gb/s 4λ CWDM TOSA for datacenter optical interconnects", *Optics Express*, vol. 26, no. 16, p. 19742, 2018.
12. R. Li, D. Patel, **A. Samani**, E. El-Fiky, Z. Xing, M. Morsy-Osman and D. Plant, "Silicon Photonic Ring-Assisted MZI for 50 Gb/s DAC-Less and DSP-Free PAM-4 Transmission", *IEEE Photonics Technology Letters*, vol. 29, no. 12, pp. 1046-1049, 2017.
13. R. Li, D. Patel, **A. Samani**, E. El-Fiky, Z. Xing, M. Sowailem, Q. Zhong and D. Plant, "An 80 Gb/s Silicon Photonic Modulator Based on the Principle of Overlapped Resonances", *IEEE Photonics Journal*, vol. 9, no. 3, pp. 1-11, 2017.

14. R. Li, D. Patel, **A. Samani**, E. El-Fiky, Y. Wang, Z. Xing, L. Xu and D. Plant, "Analysis and Experimental Study of a Silicon Photonic Single MRM-Assisted MZI PAM-4 Modulator", *IEEE Photonics Journal*, vol. 9, no. 6, pp. 1-7, 2017.
15. E. El-Fiky, M. Osman, M. Sowailem, **A. Samani**, D. Patel, R. Li, M. Saber, Y. Wang, N. Abadia, Y. D'Mello and D. Plant, "200 Gb/s transmission using a dual-polarization O-Band silicon photonic intensity modulator for Stokes vector direct detection applications", *Optics Express*, vol. 25, no. 24, p. 30336, 2017.
16. R. Li, D. Patel, E. El-Fiky, **A. Samani**, Z. Xing, Y. Wang and D. Plant, "Silicon photonic dual-drive MIM based 56 Gb/s DAC-less and DSP-free PAM-4 transmission", *Optics Express*, vol. 26, no. 5, p. 5395, 2018.
17. E. El-Fiky, M. Chagnon, M. Sowailem, **A. Samani**, M. Morsy-Osman and D. Plant, "168-Gb/s Single Carrier PAM4 Transmission for Intra-Data Center Optical Interconnects", *IEEE Photonics Technology Letters*, vol. 29, no. 3, pp. 314-317, 2017.
18. D. Patel, S. Ghosh, M. Chagnon, **A. Samani**, V. Veerasubramanian, M. Osman and D. Plant, 'Design, analysis, and transmission system performance of a 41 GHz silicon photonic modulator', *Optics Express*, vol. 23, no. 11, p. 14263, 2015.
19. R. Li, D. Patel, E. El-Fiky, **A. Samani**, Z. Xing, M. Morsy-Osman and D. Plant, "High-speed low-chirp PAM-4 transmission based on push-pull silicon photonic microring modulators", *Optics Express*, vol. 25, no. 12, p. 13222, 2017.
20. D. Patel, V. Veerasubramanian, S. Ghosh, **A. Samani**, Q. Zhong and D. Plant, 'High-speed compact silicon photonic Michelson interferometric modulator', *Optics Express*, vol. 22, no. 22, p. 26788, 2014.

21. M. Jacques, S. Bouvier, D. Denis, D. Patel, **A. Samani**, M. Saber, F. Mounaim, J. Gauthier and D. Plant, "Analysis, Modeling, and Mitigation of Parasitic Resonances in Integrated Metallic Seal Rings", *IEEE Transactions on Components, Packaging and Manufacturing Technology*, vol. 8, no. 6, pp. 1082-1091, 2018.

22. T. Hoang, M. Sowailem, Q. Zhuge, M. Osman, **A. Samani**, C. Paquet, S. Paquet, I. Woods and D. Plant, "Enabling High-Capacity Long-Reach Direct Detection Transmission With QAM-PAM Stokes Vector Modulation", *Journal of Lightwave Technology*, vol. 36, no. 2, pp. 460-467, 2018. (**Invited**)

23. M. Chagnon, M. Morsy-Osman, D. Patel, V. Veerasubramanian, **A. Samani** and D. Plant, "Digital Signal Processing for Dual-Polarization Intensity and Interpolarization Phase Modulation Formats Using Stokes Detection," in Journal of Lightwave Technology, vol. 34, no. 1, pp. 188-195, Jan.1, 1 2016. (**Invited**)

24. Q. Zhong, V. Veerasubramanian, Y. Wang, W. Shi, D. Patel, S. Ghosh, **A. Samani**, L. Chrostowski, R. Bojko and D. Plant, 'Focusing-curved subwavelength grating couplers for ultra-broadband silicon photonics optical interfaces', Opt. Express, vol. 22, no. 15, p. 18224, 2014.

25. N. Abadía, F. Bello, C. Zhong, P. Flanigan, D. McCloskey, C. Wolf, A. Krichevsky, D. Wolf, F. Zong, **A. Samani**, D. Plant and J. Donegan, "Optical and thermal analysis of the light-heat conversion process employing an antenna-based hybrid plasmonic waveguide for HAMR", *Optics Express*, vol. 26, no. 2, p. 1752, 2018.

Conference Proceedings NOT Directly Related to This Thesis

26. R. Li, **A. Samani**, E. El-Fiky, D. Patel, Q. Zhong, and D. V. Plant, "56-Gbps OOK Transmission Using Silicon Microring Assisted Mach-Zehnder Interferometer," Conference on Lasers and Electro-Optics 2016, paper STu4G.4.
27. E. Elfiky, **A. Samani**, D. Patel, and D. Plant, "A High Extinction Ratio, Broadband, and Compact Polarization Beam Splitter Enabled by Cascaded MMIs on Silicon-on-Insulator," in Optical Fiber Communication Conference 2016, paper W2A.8.
28. R. Li, D. Patel, E. El-Fiky, **A. Samani**, Z. Xing, L. Xu, D. Plant, "A C-band push-pull dual-ring silicon photonic modulator for 20 km SSMF transmission without CD compensation" Conference on Lasers and Electro-Optics (CLEO) 2017, San Jose, CA, USA.
29. D. Patel, V. Veerasubramanian, **A. Samani**, S. Ghosh, M. Chagnon, M. Osman, D.V. Plant, "A 41 GHz slow-wave series push-pull silicon photonic modulator," 2015 Conference in Lasers and Electro-Optics (CLEO), pp.1-2, 10-15 May 2015.
30. D. Patel, V. Veerasubramanian, S. Ghosh, **A. Samani**, and D V Plant, "A Lumped Michelson Interferometric Modulator in Silicon," Conference on Lasers and Electro-Optics, 8-13 June, 2014, San Jose, California, USA.
31. E. El-Fiky, P. De Heyn, M. Osman, A. Srinivasan, **A. Samani**, M. Pantouvaki, M. Sowailem, J. Van Campenhout, D. Plant, "112 Gb/s PAM4 Transmission over 2 km SMF Using a C-band GeSi Electro-Absorption Modulator", 2018 Optical Fiber Communications Conference (OFC), San Diego, CA, USA.
32. D. Patel, V. Veerasubramanian, S. Ghosh, W. Shi, **A. Samani**, Q. Zhong, and D. V Plant, "A 4 × 4 fully non-blocking switch on SOI based on interferometric thermo-optic phase shifters," Optical Interconnects Conference, 4 - 7 May, 2014, Coronado, California USA

33. M. Chagnon, M. Osman, D. Patel, V. Veerasubramanian, **A. Samani** and D. V. Plant, "1λ,6 bits/symbol, 280 and 350 Gb/s direct detection transceiver using intensity modulation, polarization multiplexing, and inter-polarization phase modulation," Optical Fiber Communications Conference and Exhibition (OFC), 2015, Los Angeles, CA, 2015, pp. 1-3. (**post deadline paper**).

34. Q. Zhong, D. Patel, **A. Samani**, V. Veerasubramanian, S. Ghosh, W. Shi, Y. Wang, L. Chrostowski, and D. V. Plant., "Advanced Silicon Photonics Components for Short Reach Optical Interconnects", Photonic North Conference 2014, Ottawa, Canada.

*Authors have equal contribution.

Table of Contents

List of Figures

List of Tables

List of Abbreviations

ADC	Analog to Digital Convertor
ASE	Amplified Spontaneous Emission
BER	Bit Error Rate
BERT	Bit Error Rate Tester
BGM	Bragg Grating Modulator
BPG	Bit Pattern Generator
CMOS	Complementary Metal Oxide Semiconductor
CPS	Coplanar Stripline
CPW	Coplanar Waveguide
DAC	Digital to Analog Convertor
DCA	Digital Communication Analyzer
DD	Dual Drive
DMT	Discrete Multi Tone
DNL	Differential Non-Linearity
DP-MZM	Dual-Parallel Mach-Zehnder Modulator
DR	Dynamic Range

DSO	Digital Sampling Oscilloscope
EDFA	Erbium Doped Fiber Amplifier
ENF	Excess Noise Factor
ER	Extinction Ratio
ESA	Electrical Spectrum Analyzer
FEC	Forward Error Correction
FIR	Finite Impulse Response
FOM	Figure of Merit
GC	Grating Coupler
HD	Hard Decision
ICR	Integrated Coherent Receivers
IM/DD	Intensity Modulation/ Direct Detect
IMD3	3rd order Intermodulation Distortion
IME	Institute of Microelectronics
INL	Integral Non-Linearity
IQ	Inphase-Quadrature
IQM	Inphase-Quadrature Modulators
ISI	Inter Symbol Interference
LCA	Lightwave Component Analyzer
LSB	Least Significant Bit
ME-MZM	Multi-Electrode Mach-Zehnder Modulator
MIM	Michelson Modulator
MMI	Multi-Mode Interference

MSB	Most Significant Bit
MPD	Monitor Photodetector
MPW	multi project wafer
MZI	Mach Zehnder Interferometer
MZM	Mach Zehnder Modulator
NRZ	Non-Return to Zero
OOK	On-off keying
PAM	Pulse Amplitude Modulation
PD	Photo-Detector
PDFA	Praseodymium-Doped Fiber Amplifier
PDK	Product Development Kit
PIC	Photonic Integrated Circuits
PPG	Pulse Pattern Generator
PRBS	Pseudorandom Bit Sequence
QAM	Quadrature Amplitude Modulation
QPSK	Quadrature Phase Shift Keying
QSFP	Quad Small Form-Factor Pluggable
RF	Radio Frequency
RLM	Ratio of Level Separation Mismatch
ROSA	Receiver Optical Sub Assembly
RRM	Ring Resonator Modulator
RTO	Real Time Oscilloscope
SD	Soft-Decision

SFDR	Spurious Free Dynamic Range
SHD	Second Harmonic Distortion
SiP	Silicon Photonics
SMF	Single Mode Fiber
SNR	Signal to Noise Ratio
SOI	Silicon on Insulator
SPP	Series Push Pull
SVR	Stokes Vector Receiver
TDL	Tunable Delay Line
TIA	Transimpedance Amplifier
TOSA	Transmitter Optical Sub Assembly
TWMZM	Travelling Wave Mach Zehnder Modulator
VCSEL	Vertical-Cavity Surface-Emitting Lasers
VECP	Vertical Eye Closure Penalty
VNA	Vector Network Analyzer
WDM	Wavelength Division Multiplexing

Chapter 1

Introduction

1.1 Motivation

Global internet traffic has been growing exponentially in the past several years. This increase is fueled by video streaming services (e.g. Netflix, YouTube), cloud-based storages (e.g. Dropbox, google drive), and machine-to-machine (e.g. Internet of Things) applications. Furthermore, emerging technologies such as artificial intelligence and augmented reality continue to transform how people interact with each other, and with their surroundings through Internet.

Since 2008 most Internet traffic has originated or been terminated in datacenters [1]. The datacenter traffic is forecasted to grow three-fold in the next five years to reach 20.6 zettabytes by 2021, where more than 70% of this data traffic stays within the datacenter [2]. This has attracted substantial worldwide research and commercialization efforts toward improving the performance of intra- and inter-data center optical communications systems. Intra-data center systems operate over shorter distances ranging from 0.5 m to 40 km (nominal distance of 10 km) in the O-band (1260-1360 nm), and inter-data center systems operate over distances ranging from 40 km to 160 km in the C-band (1530-1565 nm). While both systems share similar constraints such as power consumption, footprint and the cost of optical components, the different operating wavelengths of the two systems is a substantial challenge that requires very different approaches for addressing the demand for intra- and inter data center applications.

1.1.1 Higher Order Modulation Formats

Since the inception of the fiber optics communication, On-Off Keying (**OOK**) has been the main modulation format employed in short reach optical interconnects. OOK can be described as a simple form of amplitude modulation where digital data (0 and 1) are presented in the form of absence or presence of light. The simplicity of the transmitter and receiver architectures have been an important factor in the success of OOK for short reach optical links. Recently deployed 100 Gb/s systems utilize OOK modulation in 4 × 25 Gb/s wavelength division multiplex (**WDM**) configuration [3]. However, as we move towards 400 Gb/s and 1 Tb/s systems, OOK requires a proportional increase in the bandwidth, and hence a more efficient modulation format is required to avoid such complexity. This has created new challenges in developing power efficient, low cost transmitter optical sub-assemblies (**TOSAs**), and receiver optical sub-assemblies (**ROSAs**) for data centers which would fit into a compact quad small form-factor pluggable (**QSFP**), since any change in modulation format usually creates further complexities in developing the TOSA and ROSA. Consequently, various modulation formats with higher spectral efficiency such as discrete multi-tone (**DMT**) [4-5], 4-level pulse amplitude modulation (**PAM-4**) [4] and quadrature phase shift keying (**QPSK**) [6-8] have been studied to replace OOK. Recently, the 200 Gb/s and 400 Gb/s IEEE Ethernet standard has been released, and the PAM-4 modulation format has been selected for 400 Gb/s systems using 4 lanes of 100 Gb/s configuration [9]. PAM-4 is another form of amplitude modulation where the 4 levels of amplitude are used to present data. PAM-4 provides up to double the spectral efficiency of OOK, and hence requires a less extreme increase in transceiver component's bandwidth. Unlike QPSK, PAM-4 is a direct detect format and as such requires minimal change to the ROSA compared to OOK, however on the TOSA, a more significant update is required to generate the PAM-4 signal. Additionally, the use of a stronger forward error correction (**FEC**) code has been included in the standard which further reduces the bandwidth constraints on individual components.

On the other hand, with the conclusion of 400 Gb/s Ethernet IEEE standard, the topic of 1 Tb/s and 1.6 Tb/s data center optical interconnects has attracted immense interest and discussion in the community. To cope with such increases in data rate, other dimensions must be exploited such as polarization and complex modulation. Dual-polarization intensity modulation / direct-detection has been proposed and experimentally demonstrated using Stokes vector direct-detection [10-16]. However, the traditional coherent system offers higher bit rates and better sensitivity compared to Stokes vector receiver (**SVR**) based systems [17-21]. The complexity of SVR systems is lower than coherent systems since the SVR has a coherent receiver front-end without the local oscillator, however only a coherent receiver can be used for a true 4D modulation. Moreover, coherent transmission systems have been accepted for inter-data center reaches and are expected to compete with the direct detection systems for shorter reaches in the near future. The higher spectral efficiency of higher order complex modulation formats such as 16 level– Quadrature Amplitude Modulation (**16QAM**) and 64 level QAM (**64QAM**), can enable transmission of higher bit rate while requiring less stringent bandwidth specification for individual components of the transceiver.

1.1.2 Rise of Silicon Photonics

In recent years silicon photonics (**SiP**) has become a popular choice for intra- and inter- data center interconnects. SiP provides several advantages such as low fabrication cost, high fabrication yields, germanium epitaxy and compatibility with the complementary metal-oxide semiconductor (**CMOS**) process [22-28]. Because of the high index contrast between Si and SiO_2, SiP optical components enjoy a relatively smaller footprint compared to other integrated photonics platforms, this results in easier integration of SiP photonic integrated circuits (**PICs**) which is desirable to fit in small pluggable transceiver packages such as in the Quad Small Form-factor Pluggable (**QSFP**) modules used in datacenter interconnects. Over the past two decades substantial research has gone into developing passive devices such as polarization rotators, splitters, waveguide crossings, etc. [29-36]. More recently active SiP devices such as High bandwidth silicon photonics modulators and high responsivity and high bandwidth silicon-germanium photodetectors have been reported [37-42], further solidifying the potential of SiP for next generation communication systems. By employing these components, SiP integrated coherent receivers (**ICR**) [43-45] and inphase-quadrature modulators (**IQMs**) have been demonstrated [46-51]. In addition, in recent years, several publicly available foundries have offered their services to academic institutions and commercial entities, paving the way for a fabless business model. As a result, 100 Gb/s SiP transceivers have now been commercialized and the quest for developing SiP based 400 Gb/s transceivers has begun.

Over the past few years, there has been significant work on PAM-4 generation using indium-phosphide (**InP**) modulators [52-53], vertical-cavity surface-emitting lasers (**VCSEL**)s [54-57], silicon photonic ring modulators [58-66], silicon-germanium electrooptic modulators [67-68], silicon hybrid modulators [69], and SiP TWMZMs [70-83]. Similarly, high bandwidth silicon-germanium photodetectors capable of single wavelength 100 Gb/s PAM-4 detection have been recently reported [84] demonstrating the capability and feasibility of SiP based intensity modulation/ direct detect (**IM/DD**) systems for 400 Gb/s intra-data center applications. In the majority of the presented works, PAM-4 is generated in the electrical domain either by passive power combination of two OOK signals or using electrical digital to analog convertors (**DACs**) and digital signal processing (**DSP**) [85-88]. Conversely for bit rates above 400 Gb/s, IM/DD can not be efficiently used due to limited spectral efficiency of PAM-4. As a result, researches have explored coherent modulation using SiP platform and have demonstrated ICRs and IQMs employing passive and active SiP components [43-51]. However, most of the work for both IM/DD and coherent systems have been done in the C-band while short reach transmission systems typically operate in the O-band and the reported bitrates have not been sufficient for 400 Gb/s and 800 Gb/s system.

1.1.3 Silicon Photonics Modulators

The electro-optic effect in silicon was first studied and presented in the seminal paper by Soref and Bennet [89] in the 1980s. They investigated the effects of carrier concentration on the refractive index of a silicon waveguide and discovered that the effective refractive index ($\boldsymbol{n_{eff}}$) of a silicon waveguide can be manipulated by changing the carrier density in the waveguide. As a result, by doping the silicon waveguide, and creating a PN junction, it is possible to change the n_{eff} of the waveguide by applying an external electric field to change the carrier concentration in the waveguide by pushing the PN junction into depletion or injection mode. This electrooptic effect in silicon is often referred to as plasma dispersion effect. Because of this discovery, SiP modulators have been studied extensively in the literature and are now commercially used in short reach applications.

More recently germanium-on-silicon electro absorption modulators have been demonstrated [67-68]. These modulators benefit from the germanium epitaxy on silicon-on-insulator platform and have been shown to operate at very low drive voltages. However, the main shortcoming of these types of modulators are their operating wavelengths. Due to the strong absorption properties of germanium at telecom wavelengths (i.e. O-band and C-band) these modulators can only operate at wavelengths beyond C-band (i.e. 1600 nm and above). Hence, these types of modulators are not the best candidates for short reach optical communication systems.

Plasma dispersion-based SiP modulators can be divided in three main categories: a) resonance-based modulators, such as ring resonator modulators (**RRMs**), b) interferometric modulators, such as Mach-Zehnder modulators (**MZMs**) and Michelson Modulators (**MIMs**) and c) grating assisted modulators, such as Bragg grating modulators (**BGMs**) [90]. High speed RRMs offer very small footprint and ultra-low modulation power consumption. However, these modulators suffer from limited optical bandwidth and strict wavelength dependence and consequently a dire need for thermal stabilization [91]. More recently, to cope with the temperature instability, RRMs have been used in Mach-Zehnder interferometers, and have shown to have excellent potential for switching and short reach communication applications [65]. On the other hand, similar to other photonic platforms such as InP and LiNbO3, travelling wave Mach-Zehnder Modulators (**TWMZM**) have been the most popular and most studied modulator types on SiP. MZMs offer higher temperature stability and fabrication tolerance compared to the other types of modulators. TWMZMs have traditionally been used for short reach communication systems. However, as we move towards 400 Gb/s systems and the replacement of OOK with PAM-4, it is necessary to re-evaluate TWMZM's potential and suitability for PAM-4. In this thesis; we focus on single drive series push-pull (**SPP**) TWMZM based architectures for PAM-4 and IQ modulations. More specifically we study various modifications to the SPP-TWMZM structure to optimize it for PAM-4 and IQ modulation. The detailed optical and microwave design and characterization of the SiP SPP-TWMZM is presented in my master's thesis [71]. We modify and optimize the design of the modulator for higher order modulation formats. We specifically focus on structures that enable the generation of PAM-4 signal on-chip, in optical domain as opposed to using electrical DACs to generate the PAM-4 signal in electrical domain. Furthermore, we evaluate the feasibility of SiP modulators for short reach coherent transmission systems in O-band.

1.2 Thesis Organization

This thesis is organized in seven chapters. Chapter 1 provides the introduction to the research topic, the motivation behind the research, and outlines the scope and the extent of this thesis.

Chapter 2 briefly presents and discusses the series push-pull (**SPP**)-TWMZM design which is the basis of the other architectures presented in this dissertation. We present the optical and microwave design of the SPP-TWMZM and discuss the advantages of SPP configuration. the layout and operation principle of the device is presented in the next sections and we present an optimized design for 400 Gb/s applications and discuss limitations of this conventional design for higher order modulation formats.

Chapter 3, details the design of an O-band SiP dual parallel MZM (**DP-MZM**) for Inphase-Quadrature modulation. The presented modulator uses the SPP-TWMZM presented in Chapter 2 as a building block. We present the necessary modifications to the modulator design for O-band operation. Further, we present the design and characterisation of a low loss resistive thermo-optic tuner used for biasing the modulator. Next, we present the small and large signal characterisation of the device. Finally, the modulator is used in a coherent transmission system. A bit rate of 180

Gb/s with 16QAM modulation is achieved over 20 km of single mode fiber without any chromatic dispersion compensation. This chapter shows the potential of coherent transmission for short reach intra-data centre application.

In Chapter 4, the same DP-MZM structure presented in the previous chapter is used for PAM-4 modulation. The modulator is designed to operate in C-band. The optical and microwave design of the modulator is presented. We explore the performance of this device in an intensity modulation/direct detection system, employing PAM-4. Differential and integral non-linearity of the device are investigated, and a driving scheme and biasing method, to improve the linearity and PAM operation of the device is presented. We operate the device at 50 Gbaud PAM-4 on a single wavelength. We characterize the chirp parameter of the device under various voltages and show that the measured -0.5 chirp parameter counteracts the dispersion of SMF at C-band.

In Chapter 5, we present an experimental study and analysis of a SiP multi electrode Mach-Zehnder modulator (**ME-MZM**) and compare its performance with a single-electrode TWMZM. Utilizing the functionality of the ME-MZM structure plus digital-signal-processing, we report: 1) the C- band transmission of 84 Gb/s OOK modulated data below the KP4 forward error correction threshold with 2 Vpp drive voltage over a distance of 2 km; 2) the transmission of a 128 Gb/s optical 4-level pulse amplitude modulated signal over 1 km of fiber; and 3) the generation of a 168 Gb/s PAM-4 signal using two electrical OOK signals. By comparing the transmission system performance measurements for the ME-MZM with measurements performed using a similar series push-pull TWMZM, we show that the ME-MZM provides a clear advantage in achieving higher baud PAM-4 generation and transmission compared to a TWMZM.

In Chapter 6, we assess the performance of all three modulator structures presented in previous chapters for PAM-4 O-band operation. We investigate and compare the performance advantages of generating PAM-4 using various structures of MZM optically as opposed to generating PAM-4 in the electrical domain using conventional DACs and MZMs. First, we present the optical design of the modulators and investigate the effects of non-linearities of the MZM transfer function and PN junction phase-shifters on performance of the PAM-4 generation. Next, we examine the effects of microwave loss and 3-dB bandwidth (**BW**) on the overall performance of the modulators. We use the simple figure of merit BW/V_π, to compare the performance of the modulators for specific baudrates and drive-voltages, where V_π is the voltage applied to the modulator to achieve π phase shift. Finally, we parametrically examine the transmission performance of each modulator and present an optimized modulator design for DAC -less and DSP less 112 Gb/s PAM-4 transmission.

Chapter 7 summarizes the conclusions drawn from the analysis, experimental characterization and transmission experiments of the SiP TWMZM, DP-MZM and ME-MZM. Future extensions of the work and possible improvements are also discussed.

1.3 Original contribution

In summary, the original contributions of this dissertation are the presentation of the modulator architectures for on-chip generation of higher order modulations formats. They are summarized hereafter:

Inphase-Quadrature (IQ) Modulation in O-Band Using SiP Dual Parallel Mach-Zehnder Modulators

- IQ modulation has traditionally been achieved using DP-MZMs. However coherent transmission systems have been predominantly used for long haul communication systems. In this thesis, we explore the feasibility of IQ modulation in O-Band for short reach communication applications. As next generation short reach communication systems move towards 1 Tb/s and higher order modulation formats, the quest for finding inexpensive, and efficient platform is heating up. The compact footprint and low fabrication cost of SiP IQ transmitters, are two compelling arguments for exploring coherent systems on SiP. We present the detailed design of an O-band IQ modulator as well as low loss resistive thermos-optic tuners for biasing the modulators. We report the DC and small signal characterization of the device and investigate the performance of the device in a coherent transmission system. We then examine the performance of the modulator in a coherent transmission system. A bit rate of 180 Gb/s with 16QAM modulation is achieved over 20 km of single mode fiber without any chromatic dispersion compensation. To the best of our knowledge, this is the highest reported single wavelength, single polarization bitrate with an O-band silicon photonic modulator.

On-Chip generation of PAM-4 using Dual Parallel Mach Zehnder modulators.

- PAM-4 has been selected as the modulation format for 400 Gb/s intra-data center applications. In this thesis, we present an alternative solution for generating PAM-4 in optical domain using DP-MZMs. We present, the design of the DP-MZM and discuss the biasing method for generating optical PAM-4 signals using two binary electrical drive signals. This was the first time a DP-MZM was used as an optical DAC for generating PAM-4 on-chip. A driving scheme and biasing method, to improve the linearity and PAM-4 operation of the device is presented. The measured second harmonic distortion and two-tone third order intermodulation spurious free dynamic range are 77 dB. $Hz^{1/2}$ and 82 dB.$Hz^{3/2}$, respectively. We further investigate the performance of the device in a short reach transmission system. We report a successful 100 Gb/s single wavelength transmission of PAM-4 over 2 km of single mode fiber below the hard decision (**HD**) pre forward error correction (**Pre-FEC**) threshold of 4.4×10^{-3}.

On Chip Generation of PAM-4 using Multi Electrode Mach-Zehnder Modulators

- We present a multi-electrode Mach-Zehnder modulator for on-chip generation of PAM-4 using binary electrical drive signals. We present the analytical study of the modulator, and its small and large signal characterization. The linearity of the transfer function of the ME-MZM along with the PN junction phase shifters are investigated. We next experimentally demonstrate the generation of 168 Gb/s PAM-4 signals using the ME-MZM driven by two OOK electrical signals which are conditioned using minimal digital signal processing. We report successful transmission of 128 Gb/s PAM-4 over 2 km of fiber below the KP4 forward error correction (**FEC**) threshold of 2.0×10^{-4} in C-band.
- Furthermore, we investigate the transmission performance of the ME-MZM and the DP-MZM compared to a conventional TWMZM over various lengths of fiber. This allows us to quantitatively compare the PAM-4 signal generation in optical domain achieved by utilizing the ME-MZM, versus DP-MZM and TWMZM. We show that ME-MZM can achieve higher bit rate transmission due to the higher bandwidth of each segment compared to a DP-MZM and TWMZM with similar bandwidth. We present an optimized design in the form of 2 segments ME-MZM with 3 mm long phase shifters and experimentally show that this modulator provides a clear improvement in transmission system performance compared to the other presented modulators. Additionally, we show that generating PAM-4 signal in optical domain using modified MZM structures such as ME-MZM and DP-MZM result in better transmission performance compared to using the

traditional single electrode TWMZM. Finally, we achieve the highest sub HD FEC threshold symbol rate presented for an O-band SiP modulator without DSP.

Chapter 2

Series Push-Pull Travelling Wave Mach Zehnder Modulator

TWMZMs have traditionally been the most popular modulators for optical communication systems. A TWMZM operates by accumulating phase modulation monolithically using a radio frequency (**RF**) modulating wave that propagates at the same speed and direction as the optical wave. Amplitude modulation is then achieved using the interferometric structure of the TWMZM. In this chapter, we present a SiP TWMZM based on the SPP-TWMZM design presented in [70] and my master's dissertation [71] which is used as a building block of the modulator architectures presented in the subsequent chapters. First, we briefly discuss the electro-optic effect in silicon called plasma dispersion. Next, we discuss the optical design and operation of the SiP SPP-TWMZM. The presented modulator in this chapter is designed for C-band as a proof of concept for feasibility of SiP modulators for 400 Gb/s systems. In subsequent chapters we will discuss modulators designed to operate at O-band.

2.1 Series Push-Pull Travelling Wave Mach-Zehnder Modulator

This section briefly covers the fabrication detail and the design of the SPP-TWMZM. Both the TWMZMs presented in this section was fabricated in a 220 nm silicon-on-insulator (**SOI**) technology on a 300 mm SOI wafer with 2 µm buried oxide via a Multi Project Wafer (**MPW**) shuttle run at the Institute of Microelectronics (**IME**) Singapore A*STAR. The modulators in this chapter were designed to operate near the 1550 nm wavelength.

2.1.1 PN Junction Phase Shifter Design

As previously mentioned, modulation in SiP platform is based on the plasma dispersion effect. Plasma dispersion effect states that the refractive index of Si waveguides can be changed by changing the carrier concentration in the waveguide. Therefore, to achieve phase-shift in SiP, PN junctions are embedded in Si waveguide by doping the waveguide. By applying an external voltage to the PN junction and driving it to depletion or injection mode, the refractive index of the Si waveguide changes and as a result the group velocity of the optical wave travelling in the SiP waveguides changes. By implementing the PN doped SiP waveguides in an interferometric structure like Mach-Zehnder interferometer (**MZI**) to create constructive and destructive interferences amplitude modulation can be achieved. Conversely, doping the waveguides results in higher optical losses. The change in refractive index at 1550 nm wavelength formulated by Soref and Bennet can be expressed as follows [89],[92]:

$$\Delta n = -5.4\times10^{-22}\Delta N^{1.011} - 1.53\times10^{-18}\Delta P^{0.838} \qquad (1)$$

The change in absorption is described by:

$$\Delta\alpha = 8.88\times10^{-21}\times\Delta N^{1.167} + 5.84\times10^{-20}\Delta P^{1.109} \qquad (2)$$

where ΔN and ΔP are carrier concentration of electrons and holes, respectively. It can be seen from the above equations that higher dopant concentration does not necessarily result in higher modulation efficiency given they result in higher optical losses. Many studies have focused on optimizing the doping concentrations in Si waveguides to achieve the highest modulation efficiency [93-94]. Since the presented modulators were fabricated in a MPW run, we had access to fixed doping dosages. Therefore, doping concentration optimization was beyond our control. Six different doping concentrations available in the process offered by IME are used in the design of the TWMZM. The PN junction in the waveguide is formed using the lightly doped P and N levels with concentration of $5 \times 10^{17}/cm^3$ and $3 \times 10^{17}/cm^3$. To form the ohmic contacts, highly doped P++ and N++ levels with concentration of $1 \times 10^{20}/cm^3$ are used. To reduce the series resistance from electric vias to the waveguide core intermediate P+ and N+ doping levels with concentrations of $2 \times 10^{18}/cm^3$ and $3 \times 10^{18}/cm^3$ are used. Figure. 1(a) illustrates the cross section of the PN junctions. In the SPP scheme [80], the PN junctions are connected in series with opposite polarity as shown in Fig. 1. The series connection of the PN junctions' results in reduced total capacitance at the expense of higher total resistance. The width of the waveguides is set to 500 nm to ensure single mode operation at C-band (~1550 nm). For operation at O-band (~1310 nm) the width of the waveguides needs to be reduced to prevent the excitation of higher order modes in the waveguide.

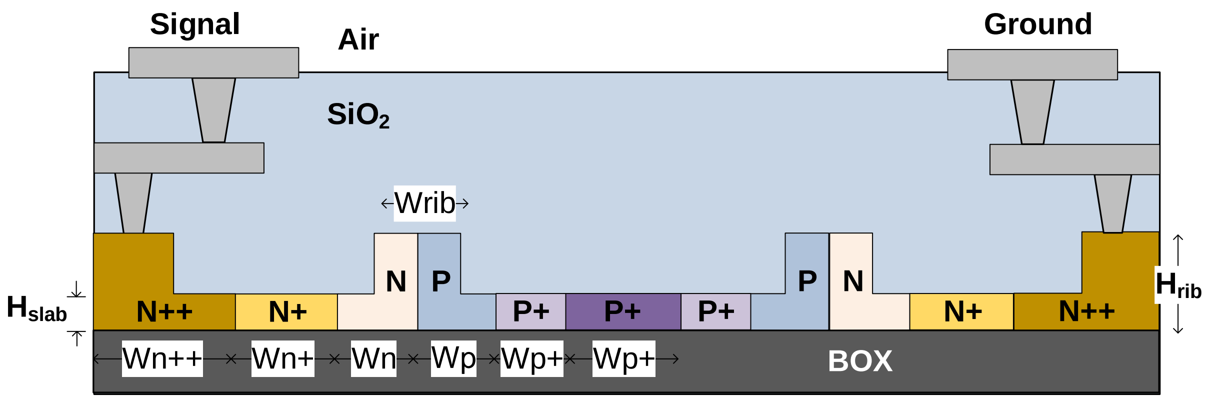

Fig. 1. The PN junction cross-section of the modulator, with dimensions: Wrib = 0.5 μm Wn++ = 5.2 μm, Wn+ =0.81 μm, Wn = 0.39 μm, Wp = 0.37 μm, Wp+ = 0.83 μm, Wp++ = 27.6 μm, Hrib = 0.22 μm, Hslab= 0.09 μm.

To prevent current flowing along the waveguides, 1.5 μm long intrinsic (undoped) sections are imbedded along the waveguide for every 9 μm of doped section, resulting in 85% fill factor. This however results in lower phase shifter efficiency. $V\pi L\pi$ figure of merit is often used to present the efficiency of a phase shifter. $V\pi L\pi$ presents the required drive voltage to achieve a full π phase shift per unit length. PN junction phase shifters are often operated in reverse bias, since the RC constant of the PN junctions in reverse bias allow for higher bandwidth operation of the device, and the optical losses of the waveguide are lower in depletion mode compared to injection mode.

2.1.2 Modulator Structure and Operation

Conventionally SiP TWMZM have dual-drive (**DD**) configuration, where a pair of differential drive voltages are used to drive each arm of the TWMZM. On the other hand, SPP scheme allows the modulator to be driven by a single RF input compared to two differential drive signals needed in conventional dual drive schemes at the expense of slightly larger drive voltages [70]. Figure 2 (a) and (b) show the simplified schematic of SPP-TWMZM and DD-TWMZM respectively.

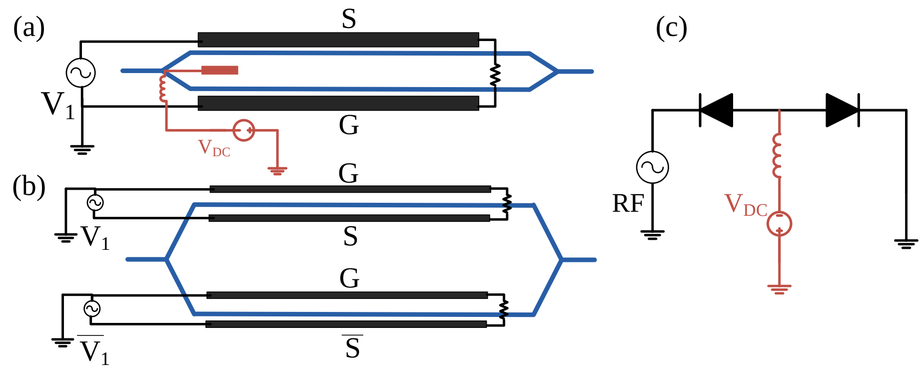

Fig. 2. Simplified Schematic of (a) SPP-TWMZM, and (b) DD-TWMZM. (c) equivalent circuit model of the SPP configuration.

In SPP the PN junctions are biased using an external DC source. The DC bias is applied to the common P++ doped region between the two PN junctions using an on-chip inductive line to ensure that the PN junctions operate in reverse bias. Travelling wave electrodes are used to drive the two arms of the modulator in a push-pull fashion. Figure 2 (c) shows the equivalent circuit model of the SPP configuration. This biasing scheme isolates DC current from the 50 Ω electrode impedance matching termination. In DD-TWMZM, the bias is applied separately to each arm using a Bias-Tee that combines both RF drive voltage and DC bias. In DD configuration each arm is driven separately using $Data$ and $\overline{Data}$ in a push-pull manner.

The performance of TWMZMs is presented using three main metrics. First, the Vπ of the device, which represents the voltage required to achieve a π phase shift. Second the 3-dB electro-optic (**EO**) bandwidth (**BW**) of the device, which presents the modulators frequency response that lies within 3 dB of the response at 1 GHz. And finally, the optical insertion loss of the device, which presents the ratio of input optical signal power to the output signal power when the modulator is biased at the top of transmission curve. Like any engineering problem, the main challenge is to optimize the trade off between Vπ, 3-dB BW and insertion loss. The main objective of an ideal TWMZM is to lower Vπ while maintaining a specific 3-dB BW required for the target bitrate.

For 400 Gb/s applications in form of 4 × 100 Gb/s, the target EO 3-dB BW is 35 GHz. In a SiP TWMZM the Vπ can be lowered by using longer phase shifters, however this results in longer travelling wave electrodes and consequently lower 3-dB BW in addition to higher insertion loss. Hence an important step in design of a SiP TWMZM is to optimize the travelling wave electrodes for the target BW. Three important criteria should be considered to maximize the EO frequency response of the modulator: (a) microwave losses of the electrodes should be minimized, (b) electrode's characteristic impedance with the PN junctions included should match the impedance of RF source, driver and termination (usually 50 Ω) and (c) the difference between the optical group velocity and microwave phase velocity should be minimized [70-71]. Microwave losses are the most important factor determining the BW of a SiP TWMZM. The PN junctions embedded in the waveguides of the TWMZM affect the BW of the TWMZM in two main aspects. In SiP TWMZMs (both SPP and DD) the PN junctions are placed in between the travelling wave electrodes. As a result, the capacitance of the PN junctions contribute to the microwave losses of the electrodes, as well as the characteristic of the electrodes. Therefore, minimizing the capacitance of the PN junctions can significantly improve the BW of the modulator. The capacitance of the PN junctions are determined by the doping concentration and the geometry of the waveguides. However, given the optical constraints of the SiP waveguides (optical losses and single mode operation), changing the capacitance by changing PN junction parameters is not a feasible option. As a result, one must look at the operation and the design of the SiP modulator. As shown in Fig. 2(c), in SPP configuration the two PN junctions are connected in series. As a result, the capacitance of the PN junctions are halved in an ideal case (two capacitances connected in series). Taking advantage of this reduced capacitance, PN junction loaded travelling wave electrodes in SPP configuration can be designed with lower microwave loss, and consequently higher BW compared to DD configuration, while maintaining the targeted 50 Ω characteristic impedance. The next challenge in designing a TWMZM is optimizing the Vπ and BW of the modulator. Increasing the length of the phase-shifters result in lower Vπ values. However, this requires longer electrodes. The longer the electrodes are the higher the microwave losses will be. Furthermore, when the length of the TWMZM increases, the optical and microwave velocity mismatch plays a more significant role in the performance of the modulator. Velocity mismatch results in lower BW and higher inter-symbol interference (**ISI**). Therefore, the main objective of the SiP TWMZM design will the optimization of the microwave losses, velocity mismatch and Vπ. In addition to the capacitance of the PN junction, the electrode metal type and geometry, the sheet resistance and permittivity of the substrate affect the microwave performance of the travelling wave electrodes. My master's thesis [71] and [70] focus on design, optimization and characterization of a SiP SPP TWMZM for 400 Gb/s applications and present a detailed analytical study and experimental characterization of a SiP SPP TWMZM. The presented travelling wave electrode design and SPP TWMZM in [70] are the basis of the subsequent SiP modulator architectures presented in this thesis. Figure 3 shows the layout of the SPP modulator.

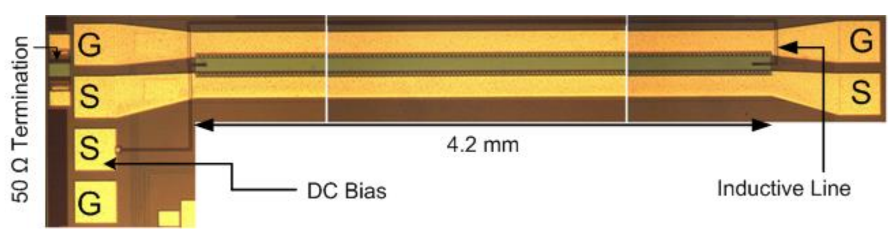

Fig. 3. Micrograph of the SPP TWMZM.

The IME process offers two aluminum metal layers. The first layer is used to form the inductive line for the DC connection, while the top layer is used to form the travelling wave electrodes. The travelling wave electrodes are in the coplanar strip-line (**CPS**) configuration with strip width of 60 μm. The spacing between the two strips is set at 37 μm. This width and spacing results in 50 Ω characteristic impedance when the PN junctions are biased at -3 V. The length of the phase shifter on each arm of the TWMZM shown in Fig. 3 is 4.2 mm and the total electrode length is 4.7 mm. The $V_\pi L_\pi$ of the phase shifter is 3.15 V-cm, and the small signal V_π is 7.5 V. The 3 dB bandwidth the modulator is measure to be 35 GHz at – 3 V bias voltage.

Chapter 3

Inphase-Quadrature (IQ) Modulation Using Dual Parallel Mach-Zehnder Modulators

In this chapter, we present inphase-quadrature (**IQ**) modulation in the O-band using dual parallel Mach-Zehnder modulators on the SiP platform. Coherent transmission has traditionally been used for long haul systems, where power consumption restrictions are not as stringent as short reach communications. However, the higher modulation efficiency of the coherent modulation formats, have made them an attractive alternative for 1Tb/s intra-data center applications. Moreover, coherent transmission systems have been accepted for inter-data center reaches and are expected to compete with the direct detection systems for shorter reaches in the near future. More recently conventional O-band dual drive Mach-Zehnder modulators were employed for QPSK modulation, however these approaches require further modification of transmitter and achieve transmission only at low baud rates compared to utilizing DP-MZMs [95]. To assess the performance of SiP IQMs for short-reach applications, there is a clear need to study O-band transmission performance using the SiP IQ modulators to generate high baud rate high order QAM formats. In the subsequent sections, the detailed design of the IQ modulator (**IQM**) is discussed. We discuss a low loss resistive thermo-optic heater used for biasing the modulator. We then report the DC and small signal characterization of the device and investigate the performance of the device in a coherent transmission system.

3.1 Device Design and Fabrication

In this section, we present the design and characterization of the IQM. Figure 4 shows the schematic of the IQM. The modulator was fabricated in a multi project wafer run at IME A*STAR on a silicon-on-insulator (SOI) wafer with a 220-nm thick silicon layer, a 2 μm thick buried oxide layer, and a high resistivity 750 Ω-cm silicon substrate. The IQM consists of two-child SPP TWMZMs connected in parallel using compact low loss Y splitter/combiners [96]. We use strip waveguide S-bends to separate each arm of the MZMs after the Y splitters. The arms of the child MZMs are separated by 31 μm, while the arms of the parent MZI are separated by 305 μm. The two arms of the child MZMs are designed to be the same length, hence creating a balanced MZI. On the other hand, one arm of the parent MZI is designed to be 100 μm longer than the other arm creating an intentional imbalance between the two arms of the parent MZI. The phase shifter length of each child MZM is 3 mm. To prevent any current flowing along the waveguides, 2 μm long intrinsic sections are inserted along the phase shifter for every 18 μm of PN junction, creating a 90% phase shifter fill factor. This results in 2.7 mm effective phase shifter length. The SPP configuration of the child MZMs provides several advantages in both the operation and the performance of the IQM. As discussed in the previous section SPP TWMZMs are operated by only one drive signal compared to the conventional DD-TWMZMs where two drive signals are required. This significantly lowers the operation complexity of the IQM, as the modulator can be operated with two drive signals as opposed to four for the case of an IQM with the conventional DD child MZMs. In addition, lowering the number of RF drive signals lowers the foot print of the IQM [72].

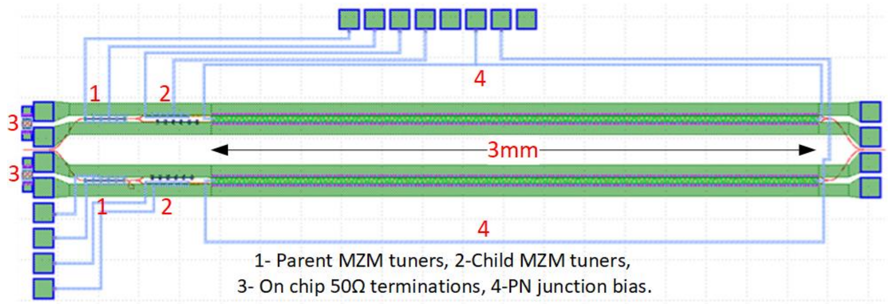

Fig. 4. Schematic of the IQM.

The IQM is based on the SPP TWMZM modulator presented in [70]. However, the modulator design is updated for O-band operation. We use 400 nm wide waveguides which are slightly wider than the strictly single mode width used for O-band operation. This increase in waveguide width, lowers the optical propagation losses in the waveguides. Figure 5 illustrates the PN junction cross-section of the modulator. To accommodate O-band operation and to minimize the change in RC constant of the PN junctions compared to the C-band, the doping width were slightly modified. As the fabrication process is the same as the TWMZM presented in the previous chapter, the electrode design of the modulators requires minimal update. The capacitance of the PN junction is dependent on the geometry (height and width) of the waveguide, and the doping concentration of the PN junction. The height of the waveguide and doping concentrations have remained the same as that of the modulator presented in the previous chapter. The change in waveguide width would results in a slight change in capacitance of the PN junctions. We use a commercial simulation tool to estimate the capacitance of the PN junction. For the simulation, the peak concentration of the P and N are set at 7×10^{17} cm^{-3} and 5×10^{17} cm^{-3}, respectively and we assume Gaussian distribution of the dopant ions in the silicon [97]. The capacitance of the PN junction in a 400 nm wide slab waveguide is simulated to be 230 pf/m at 0 V, and 160 pf/m at -3 V which is within 1% of the values for 500 nm wide waveguide used for C-band applications. As a result, the effects of the change in waveguide geometry and PN junction capacitance on the microwave loss and characteristic impedance of the travelling wave electrodes are minimal. The travelling wave electrodes of the modulator are in the symmetric coplanar stripline configuration made of aluminum alloy. The thickness of the metal layer is set to 2 μm in the foundry process, the width of ground and signal lines are set at 60 μm and the spacing between them is set to 36 μm. These width and spacing values of the electrode result in 50 Ω characteristic impedance when the PN junctions are biased at 3 V. 50 Ω terminations formed using doped silicon are place near the termination pads of the electrodes, for on chip termination. The electrodes are connected to the 50 Ω terminations by placing gold wire balls, using a wire bonder machine.

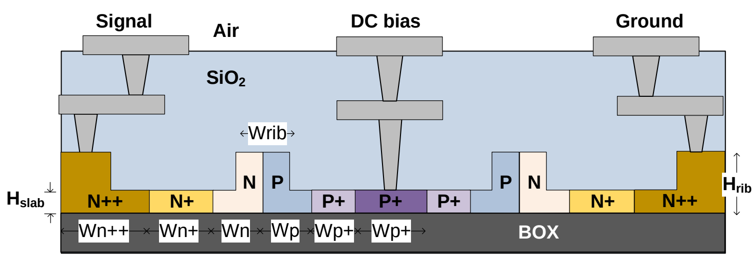

Fig. 5. The PN junction cross-section of the modulator, with dimensions: Wrib =0.4 μm, Wn++ = 7 μm, Wn+ =0.78 μm, Wn = 0.42 μm, Wp = 0.4 μm, Wp+ = μm, Wp++ = 28.6 μm, Hrib = 0.22 μm, Hslab= 0.09 μm.

As shown in Fig. 4, four thermo-optic tuners are used to bias the modulator. A thermo-optic tuner is placed on each arm of the child MZMs to control the bias of each MZM individually. However only one tuner for each child MZM is electrically connected and operational. The second tuner is added to ensure that both arms of child MZMs have equal optical losses. Similarly, two tuners are placed on each arm of the parent MZM to control the bias of the parent MZM. Figure 6 (a-d) shows the layout, image, and cross section of the thermo-optic tuners. The tuners are formed by connecting resistive segments along the waveguide in parallel [98]. Each segment consists of two resistors created by doping the silicon slab on each side of the waveguide using the N++ dopant level with peak concentration of 1×10^{20} cm^{-3}. Each resistive segment is 29 µm long. Since the core of the waveguide is not doped, the effects on optical loss are negligible. Due to the parallel connection of the resistive segments, the overall resistance of the tuners is minimized while the length of the tuners along the waveguides are maximized which results in more power efficient operation. The parent MZM utilizes a tuner with 5 segments, while the child MZMs use tuners with 6 segments. This results in the parent tuners having a slightly higher resistance compared to the child MZMs tuners.

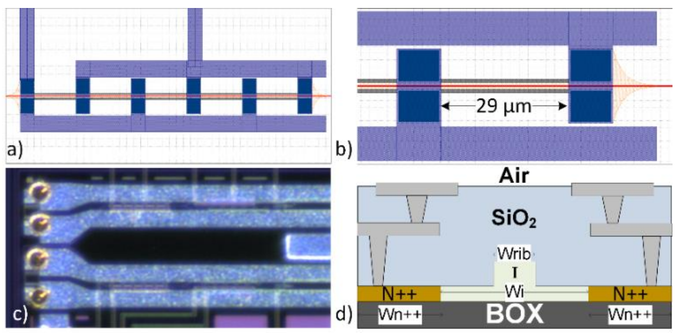

Fig. 6. (a) Close up top-view of the parent tuner, (b) single section of the thermo-optic tuners, (c) micro-image of the tuners and ball bonded on-chip 50 Ω termination, and (d) cross section of the thermo-optic tuners, Wrib = 0.4 µm, Wi = 2 µm, Wn++ = 1 µm.

3.2 Device Characterization

In this section we present the DC and small signal performances of the IQM. To characterize and operate the modulator, we first need to bias the modulator properly. Commercial IQMs usually include monitor photodetectors (**MPD**) on each arm of the parent MZM to control the biasing of the IQM. Since, we did not include any MPD in our design, we bias the modulator by monitoring the output power. First, we couple light into the chip and monitor the output power of the IQMs. Then the parent and child MZM tuners are used to maximize the output power of the IQM by ensuring both arms of the MZM are in-phase. Next, we use one of the parent MZM's tuners to achieve a 90° phase shift between the two arms, which translates to an output power lower than the maximum power by 3 dB. And finally, the two child MZMs are biased at null, by minimizing the output power. When both child MZMs and the parent MZM are biased at maximum the insertion loss of the IQM excluding the grating coupler and routing losses are measured to be 4.1 dB.

Figure 7 (a) shows the IV curve of the child and parent MZM's thermo-optic tuners. As seen from the slope of the IV curve, the tuner's resistance slightly varies with applied voltage which suggests they are non-ohmic at higher voltages. The phase-change ($\Delta\Phi$) versus voltage of the tuners is shown in Fig. 7(b). The child tuners achieve a π phase-shift at 1.7 V while the parent tuners achieve a π phase-shift at 1.9 V. The power consumption of the child and parent tuners for a π phase shift are 14.3 mW and 16.2 mW, respectively, suggesting that due to their lower total resistance, and longer length the child heaters are more power efficient than the parent heaters. We encountered a small drift in the child MZMs bias points during operation of the device, this is attributed to the small separation between the arms of the child MZMs, which causes the tuners to effect both arms of the MZMs. On the other hand, the parent MZM bias was less affected by thermo-optic cross talk. Figure 7 (c) shows the phase change versus DC voltage of the PN junction phase shifters of the child MZMs. The DC $V\pi$ of each child MZM is measured to be around 12 V. As shown in Fig. 7(c) the PN junction phase shifters have a nonlinear phase change versus voltage, which results in different behavior of a SiP modulator compared to a LiNbO3 and InP modulator [99]. For higher modulation formats such as PAM-4 and 16QAM that employ multi-amplitude levels this non-linearity can result in higher error rates, therefore a non-linear compensation is used [73].

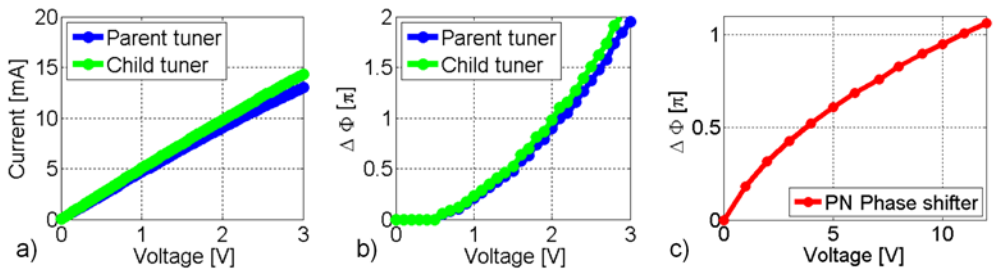

Fig. 7.(a) IV curve of the child and parent MZM's thermo-optic tuners, (b) the phase-change (ΔΦ) versus voltage of the thermo-optic tuners, and (c) the phase shift versus voltage of MZM's PN junction phase shifter.

Next, we characterize the small signal response of the IQM by measuring the response of each child MZM individually. This is done by first biasing the parent modulator at the top of transmission curve (i.e. both arms of parent MZM are in phase). Next, to measure the top child MZM, we bias it at quadrature point, while the bottom child MZM is biased at null using the thermo-optic tuners, this procedure is repeated for the bottom child MZM. Figure 8 presents the electro-optic S_{21} and electrical S_{11} measurements of both child MZMs for various PN junction bias voltages. The measurements are taken by terminating the travelling wave electrode on chip, by bumping on-chip 50 Ω terminations to the electrodes as shown in Fig. 7(b). Both modulators are measured to have over 30 GHz of bandwidth when the PN junction phase shifters are reversed biased at -3 volts.

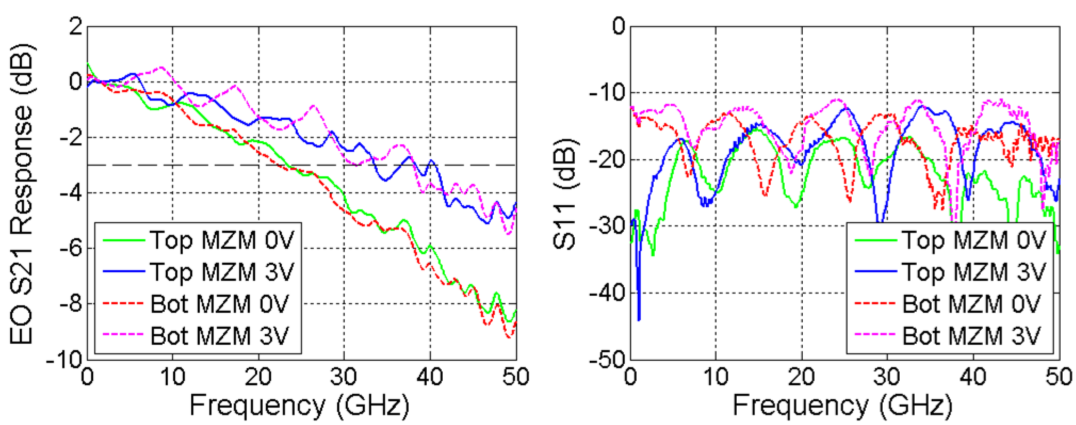

Fig. 8. EO and S11 response of the IQM.

3.3 Transmission Experiment

We investigate the performance of the modulator in a coherent transmission system. Figure 9 shows the schematic of the experimental setup. A 12 dBm tunable wavelength O-band laser is used to couple light into the SiP chip through vertical grating couplers (**GCs**). The insertion loss of two GCs connected back-to-back is measured to be 10 dB at 1305 nm. The excess losses due to routing waveguides from GCs to the IQM are estimated to be 3.8 dB. When both child MZMs and the parent MZM are biased at maximum the insertion loss of the IQM is measured to be 4.1 dB.

Two RF drive signals are generated using two 8-bit DAC channels operating at 88 GSa/s, and the drive signals are amplified using two matched 45 GHz RF amplifiers. Two RF tunable delay lines (**TDL**) are used to compensate for any skew between the two signals caused by mismatched RF cables and adapters in the two paths. The two signals are then applied to the IQM using 50 GHz RF probes. The modulated optical signal is amplified using a praseodymium-doped fiber amplifier (**PDFA**) to 0 dBm average optical power. The signal is then fed into an O-band coherent receiver. Since we did not have access to balanced O-band PDs we use four single ended PDs instead of two balanced PDs. The common mode rejection operation is instead done using DSP. The coherent receiver used for this experiment was built using discrete components, however silicon photonic based integrated coherent receivers both in C band and O band have been demonstrated [43-44]. Additionally, waveguide coupled silicon germanium photodetectors with more than 50 GHz 3-dB BW and 1 A/W responsivity have been demonstrated in [37-42], which further proves the feasibility of coherent transceivers in silicon photonics platform.

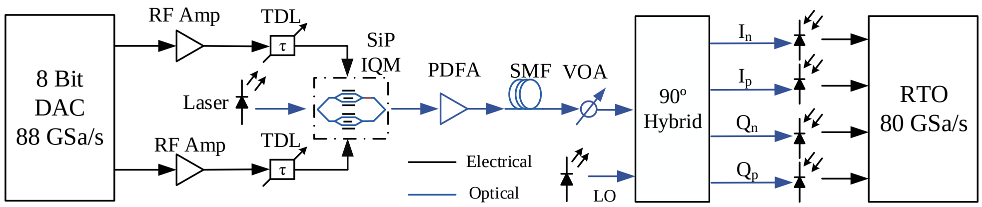

Fig. 9. Schematic of the experimental setup. **TDL**: Tunable delay line, **SMF**: single mode fiber, **VOA**: variable optical attenuator, **RTO**: real time oscilloscope.

Fig. 10 shows the transmitter and receiver DSP stacks used in this experiment. As the target application of the O-band IQM is short reach links within a datacenter, we employ simple DSP on both the transmitter and the receiver sides. The transmitter DSP starts with QPSK or 16QAM symbol generation. The generated symbols are then pulse shaped using a gaussian filter at 2 samples per symbol followed by resampling from 2 samples per symbol to 88 GSa/s which is the DAC sampling rate. Next, digital pre-emphasis using a finite impulse response (**FIR**) filter is applied on the data samples for equalization of the combined frequency response of the DAC and the RF amplifiers. Finally, the amplitude levels of the electrical 16QAM signal are controlled to pre-compensate for the non-linear transfer function of the SiP IQM and achieve equidistant amplitude levels in the optical domain. Next, data samples are quantized and uploaded to the DAC memory. On the receiver side, since single ended PDs were used instead of balanced PDs, the DSP starts by common mode rejection to get the useful signal-LO beating product. This is followed by IQ power imbalance compensation to compensate for the PD + TIA responsivity and gain variations. Next, quadrature phase error correction is done to correct any imperfections in the optical 90° hybrid and ensure orthogonality of the I and Q signals. The complex received signal is then resampled from 80 GSa/s (the sampling rate of RTO) to 2 × the symbol rate and synchronization and time recovery is applied. Finally, an equalizer with 15 taps is applied to the received signal and error counting is performed. As the device is operated in O-band there is no need for chromatic dispersion compensation even for 20 km transmission and over 10 nm away from the zero-dispersion wavelength of the SMF fiber used. This was confirmed by comparing the taps spread over time for back to back and 20 km received signal.

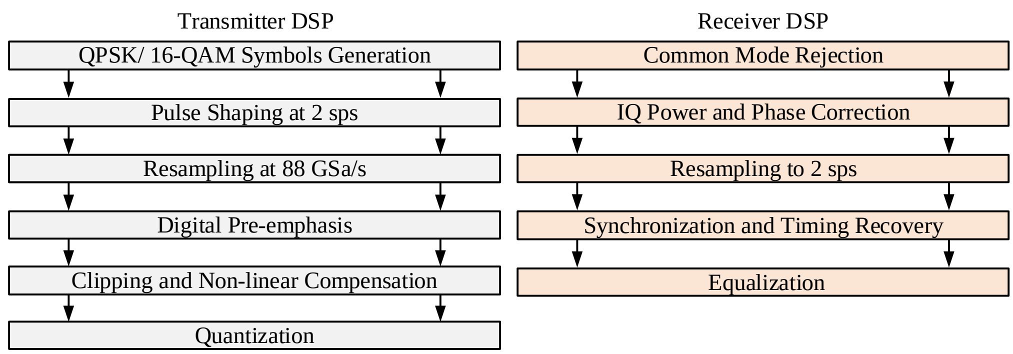

Fig. 10. Transmitter and receiver DSP stack.

Figs. 11(a) and (b) show the QPSK and 16QAM constellations at 56 and 40 Gbaud after 20 km of single mode fiber, respectively. The drive voltage of the modulators was 4.5 Vpp for the 56 Gbaud QPSK constellation and 4 Vpp for 40 Gbaud 16QAM. The 16QAM electrical drive signals were intentionally attenuated at the input of the RF amplifiers in order to limit the operation of the amplifiers to their linear gain region. The launched optical power in both cases was 0 dBm. The insertion loss of the 20 km SMF-28 spool was measured to be 7.5 dB, resulting in received optical power of -7.5 dBm at the input of the coherent receiver. The LO power for all of the transmission experiments was set at 2 dBm. Fig. 11(c) shows the BER versus the symbol rate for QPSK and 16QAM modulation. We achieve below hard decision (**HD**) forward error correction (**FEC**) threshold transmission of 77 Gbaud QPSK and 45 Gbaud 16QAM over 20 km of SMF without the need for chromatic dispersion compensation.

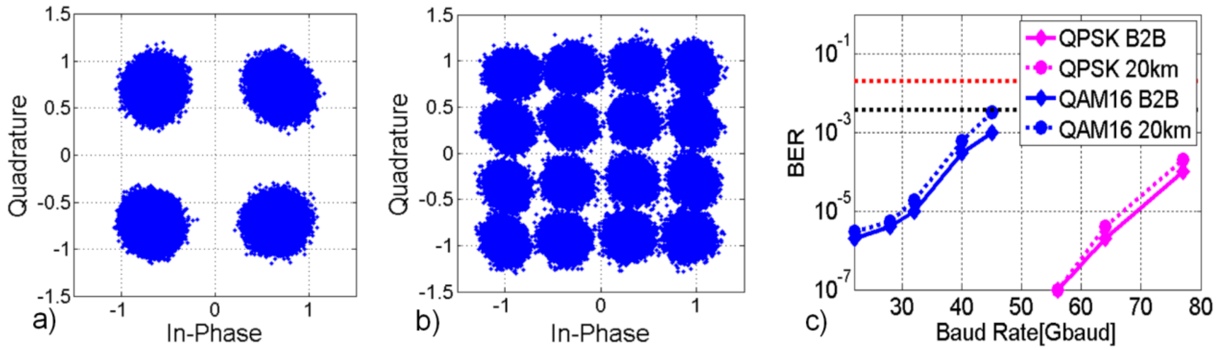

Fig. 11. (a) 56 Gbaud QPSK constellation after 20 km of SMF fiber, (b) 40 Gbaud 16QAM constellation after 20 km of SMF, and (c) BER versus the baudrate for QPSK and 16QAM modulation. The black and red horizontal dashed lines present the HD-FEC and soft decision (SD) FEC threshold respectively.

Next, we investigate the performance of the IQM for various drive voltages. Figs. 12 (a) and (b) show the BER performance of the transmission system versus drive voltage applied to the IQM for QPSK and 16QAM, respectively. We achieve below HD-FEC transmission of 77 Gbaud QPSK, with 3 Vpp which is comparable to EML or InP based TOSA's drive voltages [100-101], while we were able to transmit 45 Gbaud 16-QAM below HD-FEC with 4 Vpp drive voltages and 3 Vpp below soft decision (**SD**)-FEC. It should be noted that this (180 Gb/s) is the highest achieved bitrate with 3 Vpp drive voltage using a SiP modulator. The performance of the modulator is limited by the excess on-chip routing losses and the GC losses. We expect the performance of the modulator could be further improved by only modifying the layout of the modulator to decrease these losses. Next, we reduce the received signal power using a variable optical attenuator and measure the BER while the local oscillator power is kept constant at 2 dBm. The receiver sensitivity for the 77 Gbaud QPSK modulation at the HD-FEC threshold is approximately – 17 dBm of signal power. On the other hand, we successfully achieve below HD-FEC transmission of 45 Gbaud 16QAM with -11 dBm of received signal power. At the higher symbol rate, the transmission system is also limited by the PD+TIA and RTO bandwidth. The error floor is dominated by the transmitter noise. The two main contributing factors are the low drive voltage of the modulator, and high insertion loss of the transmitter due to grating coupler and routing losses. Since the modulator is driven by only a fraction of the Vπ value, the maximum extinction ratio achieved is consequently lower, in addition due to the excess routing and coupling losses on the SiP chip the signal is further attenuated.

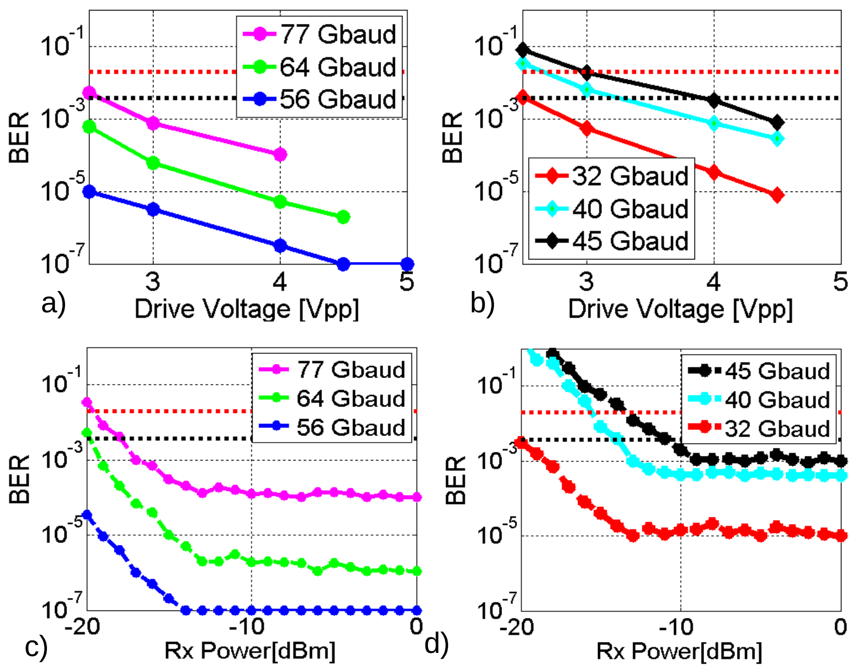

Fig. 12. BER performance of the transmission system versus drive voltage applied to the IQM for (a) QPSK and (b) 16QAM. BER performance of the transmission system versus received optical power for (c) QPSK and (d) 16QAM.

3.4 Conclusions

In this chapter, as an initial step we looked at utilizing the coherent modulation formats for short reach applications. Given the low fabrication cost and small footprint of SiP integrated circuits, a SiP coherent transceiver can be an outside the box solution for the 1 Tb/s systems. We successfully achieved below HD-FEC, 180 Gb/s 16QAM and 154 Gb/s QPSK transmission over 20 km of SMF-28. Furthermore, we demonstrate that 77 Gbaud QPSK transmission can be achieved with a low drive voltage of 3 Vpp. To the best of our knowledge this is the highest achieved bitrate transmission and lowest drive voltage combination using a SiP modulator. The maximum single wavelength transmission baudrate could easily be improved by adding a second polarization which is common for coherent transmission systems. And hence, this work supports the idea that SiP based intra-datacenter coherent solutions could be a possible candidate for next generation short reach interconnects.

Chapter 4

Dual Parallel Travelling Wave electrode Mach-Zehnder Modulator

In this Chapter, we present a C-band SiP DP-MZM utilizing the SPP-TWMZM design presented in Chapter 1. We explore the performance of this device in an intensity modulation/direct detection system, employing PAM-4. DP-MZMs are traditionally used for IQ modulation and coherent transmission as shown in Chapter 3. However, the dual parallel architecture can be used to generate PAM-4 signals in the optical domain without the use of electrical DAC and digital signal processing (**DSP**). Differential and integral non-linearity of the device are investigated, and a driving scheme and biasing method, to improve the linearity and PAM operation of the device is presented. Next, the measured second harmonic distortion (**SHD**) and two-tone third order intermodulation distortion (**IMD3**) spurious free dynamic range (**SFDR**) are measured and presented. We operate the device at 100 Gb/s PAM-4 on a single wavelength. Further, we characterize the chirp parameter of the device under various voltages and discuss its effects on transmission.

4.1 Device Design, Fabrication and PAM-4 Operation

Similar to the modulator presented in the previous chapter, this DP-MZM was fabricated in a MPW run at IME A*STAR on a silicon on insulator wafer with a 220 nm thick silicon layer and a 2 µm buried oxide layer. Each of the child MZMs have SPP configuration based on our previous work in [70] and are designed to operate in the C-band. All the design parameters such as doping densities, PN junction geometries, electrode length and geometry were identical to [70] as presented in Section 2.2. However, the active phase shifter length of each MZM was changed to 3.95 mm to accommodate the extra optical routing in the dual parallel design. Relative to [70], the phase shifter length reduction results in slightly higher $V\pi$ and lower optical insertion loss. Figure 13 demonstrates the layout of the DP-MZM. Balanced C-band 3-dB Y-branches are used at the input and output of the DP-MZM to divide and combine the light going in and out of each branch. The insertion loss of each Y-branch is measured to be 0.3 dB. This DP-MZM is designed to have balanced branch lengths, to ensure that the outputs of MZI-1 and 2 are in-phase at the combining Y-branch of the DP-MZM. To further correct the phase difference between the two branches and ensure that both arms are in-phase a thermo-optic tuner is placed after the output of MZM-1. The design of the thermos-optic tuner is similar to the one presented in section 3.1. However, the waveguide width has been changed from 400 nm to 500 nm to accommodate low loss single mode operation at C-band. This increase in waveguide width has a negligible effect on the resistance of the tuner. Ideally, due to their push-pull operation, SPP-MZMs are expected to have no phase modulation at their output. However, in case of a doping imbalance in the phase shifter between the arms of the SPP-MZM, there will be residual phase modulation. If the phase modulation is negligible relative to the amplitude modulation, the DP-MZM can be operated to achieve PAM-4.

However, if the phase modulation is significant when the outputs of inner MZMs are combined at the outer MZM the phase modulation can result in an out of phase combination of the two signals [102]. To evaluate the phase modulation of each inner MZM, their chip parameter is measured and presented.

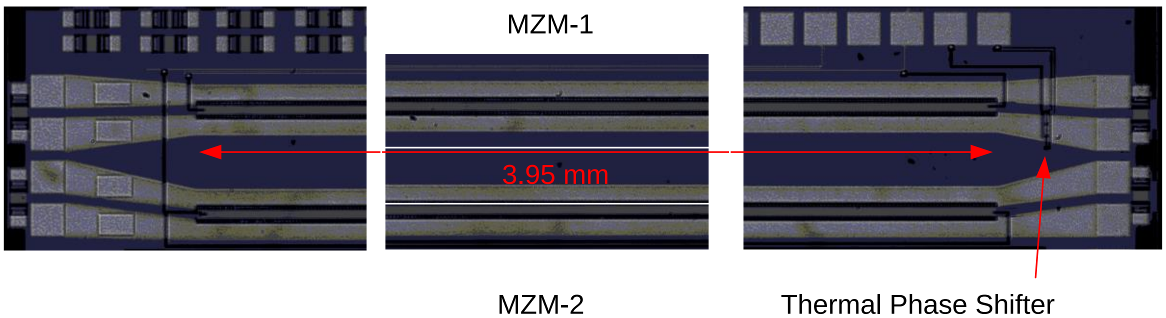

Fig. 13. Micrograph of the C-band DP-MZM.

Figure 14 illustrates the setup required to generate PAM-4 signals using the DP-MZM. Two independent non-return to zero (**NRZ**)-OOK signals; S1 and S2 are generated using a pulse pattern generator (**PPG**) with the maximum baud rate of 50 Gbaud. S1 is then amplified by 6 dB with respect to S2, such that S1 and S2 represent the most significant bit (**MSB**) and the least significant bit (**LSB**), respectively. Two tunable RF delay lines are used to accurately align the transition of each bit stream. S1 and S2 are applied to MZM-1 and MZM-2, respectively. MZM-1 and MZM-2 are independently biased such that the smallest power out of each MZM is equal.

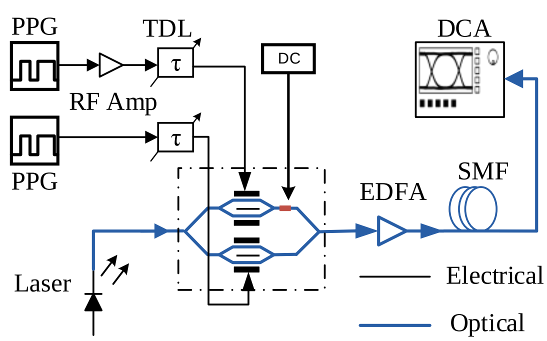

Fig. 14. PAM-4 modulation setup. (TDL: Tunable delay line, DCA: Digital Communication Analyzer, EDFA: Erbium doped fiber amplifier, SMF: Single mode fiber)

4.2 Device Characterization and Performance

Due to higher number of power levels in PAM-4 the non-linearity of the PAM transmitter plays a significant role in achieving higher baud rates and equidistant power levels. As PAM-4 is replacing OOK, it is crucial to have a universal benchmark for evaluating the linearity performance of PAM transmitters. Differential non-linearity (**DNL**) and integral non-linearity (**INL**) are the two measures of linearity commonly presented for DACs. The same methodology can be applied to the presented DP-MZM to evaluate the linearity of the device as a 2-bit optical DAC. In addition, at higher baud rates the effects of intermodulation distortion and compression result in degradation of the modulated signal as observed in the eye diagram and BER measurements presented in the next section. Microwave linearity of optical modulators such as SFDR and third-order IMD3 are often studied to evaluate the performance of optical modulators at higher baud rates and for microwave photonics applications.

4.2.1 Measures of Linearity

In this section we present the linearity performance of the DP-MZM to evaluate its potential for PAM-4 generation and transmission.

As expected the two parallel MZMs exhibit, very similar $V\pi L\pi$ performance of 3.5 and 3.47 V-cm which agrees with our single MZM characteristic presented in [70] and [71]. The phase shift of each of the two SPP-MZMs under different voltages were measured and are illustrated in Fig. 15 (a). The transmission curve of the DP-MZM with the assumption that the Y-branches have 50/50 splitting ratio and both inner MZMs are under the same bias voltage is shown in Fig. 15 (b). Fig. 15 (b) illustrates the transfer function of DP-MZM using the measured phase shift.

INL is defined as the maximum deviation of the DAC's analog output (transfer function) from an ideal linear fitted line in terms of the LSB, and can be calculated as [103]:

$$INL = \left(\frac{V_B - V_{zero}}{V_{LSB}} \right) - B \ , \tag{3}$$

where V_B is the analog output corresponding to the digital binary input B, and V_{LSB} is the ideal spacing between two adjacent analog outputs. In an ideal DAC, all intensity steps equal V_{LSB} and the INL will be 0. Differential non-linearity is used to quantify DAC's output precision and is defined as the difference between an actual step height and the ideal value of LSB [103]:

$$DNL = \left(\frac{V_B - V_{B-1}}{V_{LSB}} \right) - 1 \ , \tag{4}$$

As shown in Fig. 15 (b), due to the inherent non-linear transmission function of MZMs, achieving equidistant power levels of PAM-4 signal is quite challenging. When DP-MZM is operated at its full dynamic range (green dotted line in Fig. 15 (b)) the INL and DNL are estimated to be 0.58 and 0.33 LSB, which result in very uneven PAM-4 intensity level distribution. Therefore, some linearization techniques are required to further improve the operation of PAM-4 transmitter. To improve the linearity of a DP-MZM and mitigate the effects of its nonlinear transfer function we reduce the operating dynamic range of the device to 0.63 Vπ which corresponds to 6 Vpp (red dotted line in Fig. 15(b)) by restricting the drive voltages of MZM-1 and MZM-2 to 0.42 Vπ and 0.21 Vπ (4 Vp-p and 2 Vp-p respectively), and biasing each MZM such that the 0 levels of both MZMs are at the same level; for which the resulting INL and DNL are calculated to be 0.21 and 0.11 LSB, respectively. A lower dynamic range would result in a better linearity performance of the device; however, it will also decrease the height of each step, which in practice result in lower extinction ratios, and ultimately degrades the bit error rate performance. It should be noted the reduction in dynamic range is dependent on the phase shifter's VπLπ value and can vary for different doping densities. However, the biasing scheme presented can be applied to any DP-MZM.

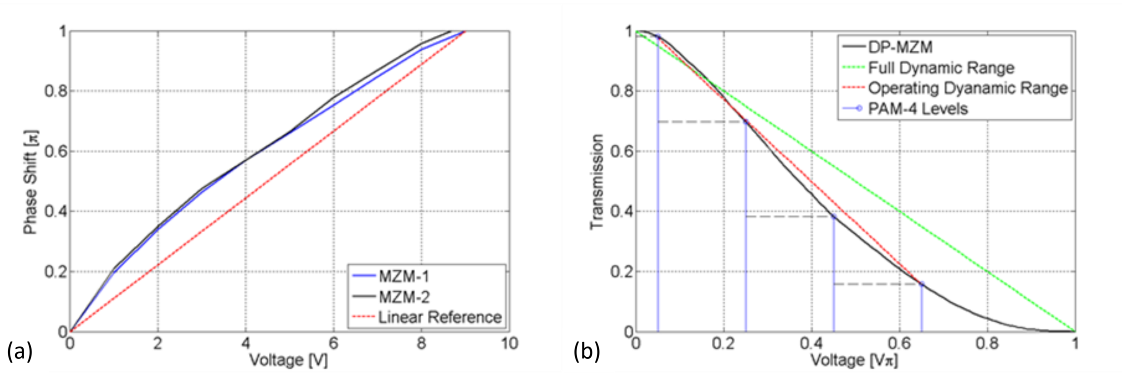

Fig. 15. (a) Phase shift vs. voltage of each MZM; (b) DP-MZM transfer function with both child MZMs at the same bias voltages.

4.2.2 Spurious Free Dynamic Range

We further examine the SHD and IMD3 SFDR performance of the DP-MZM. Figure 16 demonstrates the SFDR measurement setup. A 14 dBm TE polarized light from a high power tunable laser is coupled into the DP-MZM and the output light is then amplified to 3 dBm using an erbium doped fiber amplifier (**EDFA**). A 35 GHz photodetector followed by a 40 GHz RF electrical spectrum analyzer (**ESA**) are used to detect the signal. Two RF sources are combined and then applied to the DP-MZM using 40 GHz RF probes.

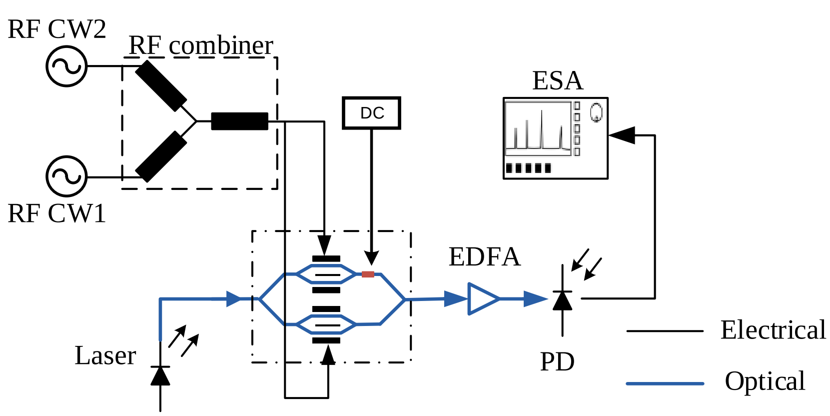

Fig. 16. SFDR measurement setup. (CW: Continues wave, ESA: Electrical Spectrum Analyzer)

Figure 17 (a), shows the RF spectra for two tone IMD3 of the DP-MZM. The RF input signals are centered at 10.05 GHz with 100 MHz spacing. From the measurement resolution bandwidth of 4 kHz, the noise power density is calculated to be -122 dBm/Hz and is used to obtain SFDR. Figure 17 (b), illustrates the second and third harmonic SFDR of the device for different input signal powers. The amplified spontaneous emission (**ASE**) noise of the EDFA can cause a slight increase in the noise floor and can be lowered by passing the output through a filter or lowering the optical losses due to on-chip routing hence eliminating the need for the EDFA. The SFDR SHD and SFDR IMD3 are measured to be 75 dBm/Hz$^{1/2}$ and 86 dBm/Hz$^{3/2}$ which are similar to reported values for LiNbO3 and SiP modulators [104-105]. This indicates that the second and third harmonics are suppressed sufficiently and the SFDR of the device is more than adequate to prevent intermodulation distortion. These values can be further improved by adjusting the power splitting ratio at the outer MZM as shown in [106].

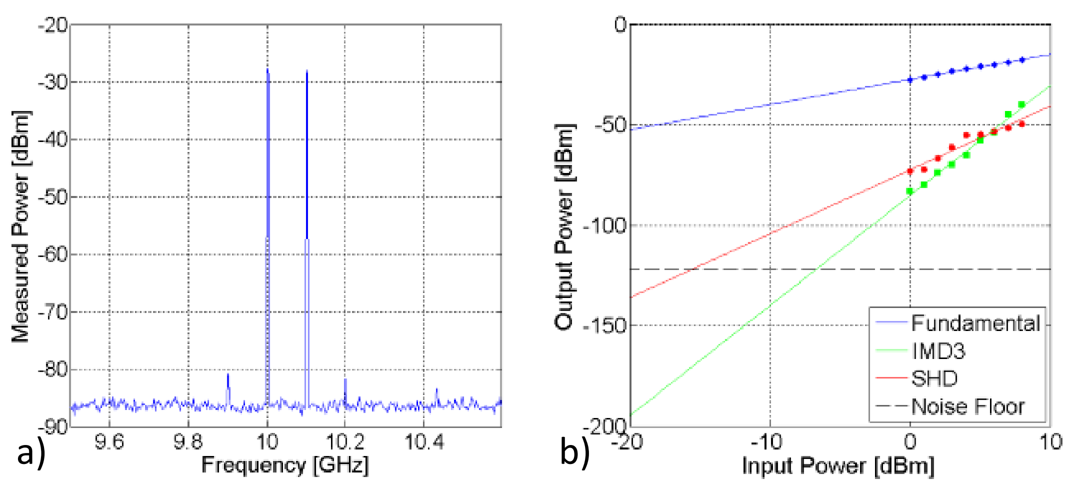

Fig. 17. (a) Measured RF spectrum of the DP-MZM for 0 dBm input power, (b) output power vs. input power of second harmonic distortion and third intermodulation distortion, with measured spurious-free dynamic ranges of -75 dB Hz $^{1/2}$ and -86 dB Hz$^{3/2}$ for SFDR SHD.

4.2.3 Small Signal and Chirp Measurements

To evaluate the modulation efficiency of the DP-MZM we examine the small signal electro-optic response of each of the MZMs separately. Two high frequency RF probe with a GSSG configuration are used to drive the transmission line of each MZM at one side and to terminate the line with 50 **Ω** at the opposite end. A 50 GHz lightwave component analyzer (**LCA**) is used to characterize the small signal properties of each of the MZMs at their operating DC bias voltages. Figure 18 (a) curves are normalized to the response at a reference frequency of 1.5 GHz. The observed bandwidth of each MZM is lower than the measured values in [70] which could be due to different tapering of the electrodes and difference in transitions between the PN-junction loaded and unloaded sections compared to [70]. Nevertheless, the observed 31.5 and 30 GHz bandwidths at operating conditions of MZM-1 and MZM-2 have been shown to be sufficient for 50 Gbaud OOK transmissions [107]. The S11 responses of both modulators shown in Fig. 18 (b) indicate that the reflection caused by impedance mismatch are sufficiently low and a good impedance matching is achieved.

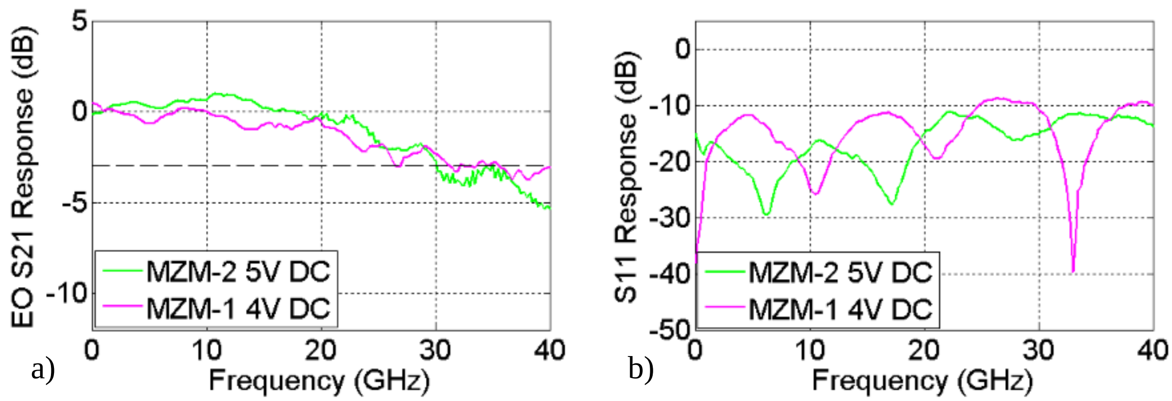

Fig. 18. (a) EO S21 Response of MZM-1 and MZM-2, with measured 3 dB bandwidth of 27 and 30 GHz for MZM-1 and MZM-2, respectively, (b) S11 response of MZM-1 and MZM-2.

Since the device is designed to operate close to 1550 nm, fiber dispersion plays a significant role in quality of signal transmission through fiber. To evaluate the susceptibility of the DP-MZM to dispersion, we investigate the small signal chirp parameter of the device, by measuring its EO response after propagating through a 36 km long dispersive SMF-28 fiber. The dispersion of the SMF-28 fiber and the modulator chirp result in resonance dips. Figure 19 (a) shows the corresponding EO response when both MZMs are biased at their operating DC voltages. The relationship between the resonance dips of the EO response and the chirp and dispersion parameters of the system are given by [108]:

$$f_u^{\,2} L = \frac{c_0}{2D\lambda^2}\left(1+2u-\frac{2}{\pi}\arctan\left(\alpha\right)\right), \qquad (5)$$

where f_u is the uth order resonance dip of the EO response, c_0 is the speed of light, D is the dispersion parameter of the fiber, λ is the operating wavelength and α is the chirp parameter. Using linear regression; $f_{u2}L$ verses $2u$ is plotted in Fig. 19 (b). The slope and position of the line yield the dispersion and chirp parameter. At the operating biases described previously both MZM-1 and MZM-2 have very similar chirp parameters of -0.58 and -0.62. We repeat the EO measurements of each MZM under different bias voltages and their corresponding chirp value is presented in Fig. 19(c). It is observed that both MZM have very close negative chirp parameter. This negative chirp is beneficial in counteracting the fiber dispersion when the output of the device is propagated through various lengths of fiber [109]. In the next section we validate this by transmitting through different lengths of single mode fiber.

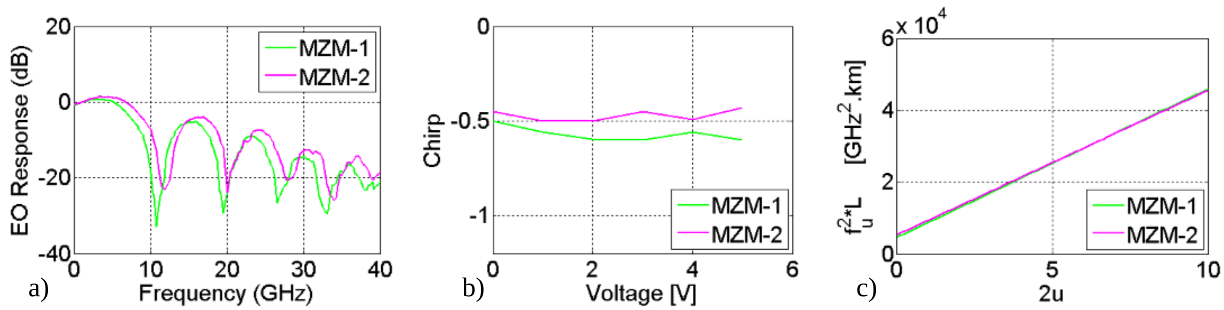

Fig. 19. (a) EO response of MZMs after 36 km of SMF, (b) linear regression of product of measured resonance frequency and length, (c) measured chirp of MZM-1 and MZM-2.

4.3 Transmission Experiment

In this section we examine the performance of the DP-MZM for PAM-4 transmission. Based on the linearity discussions in previous sections of this chapter , MZM-1 and MZM-2 are driven by 4 and 2 Vp-p drive voltages. A 14 dBm tunable laser is used to couple light into the modulator. The total insertion loss of the device is measured to be 16.5 dB, which includes the grating coupler and routing losses of 8.5 and 2.4 dB, resulting in a device insertion loss of 5.6 dB. The modulated output of the device is then amplified using an EDFA and detected by a 65 GHz sampling head of the digital communication analyzer (**DCA**). Figure 20 shows back to back NRZ-OOK and PAM-4 eye diagrams for 28 and 50 Gbaud and 50 Gbaud eye diagrams after 2 and 5 km. The OOK eyes presented are obtained by driving MZM-2 with a 2 Vp-p drive voltage (S2) which corresponds to the LSB of the PAM-4 format, while MZM-1 was biased at NULL such that its output corresponds to 0 PAM-4 power level. An error free operation up to 40 Gb/s were measured. The vertical eye closure penalties (**VECP**) for PAM-4 eye diagrams are noted below each eye diagram.

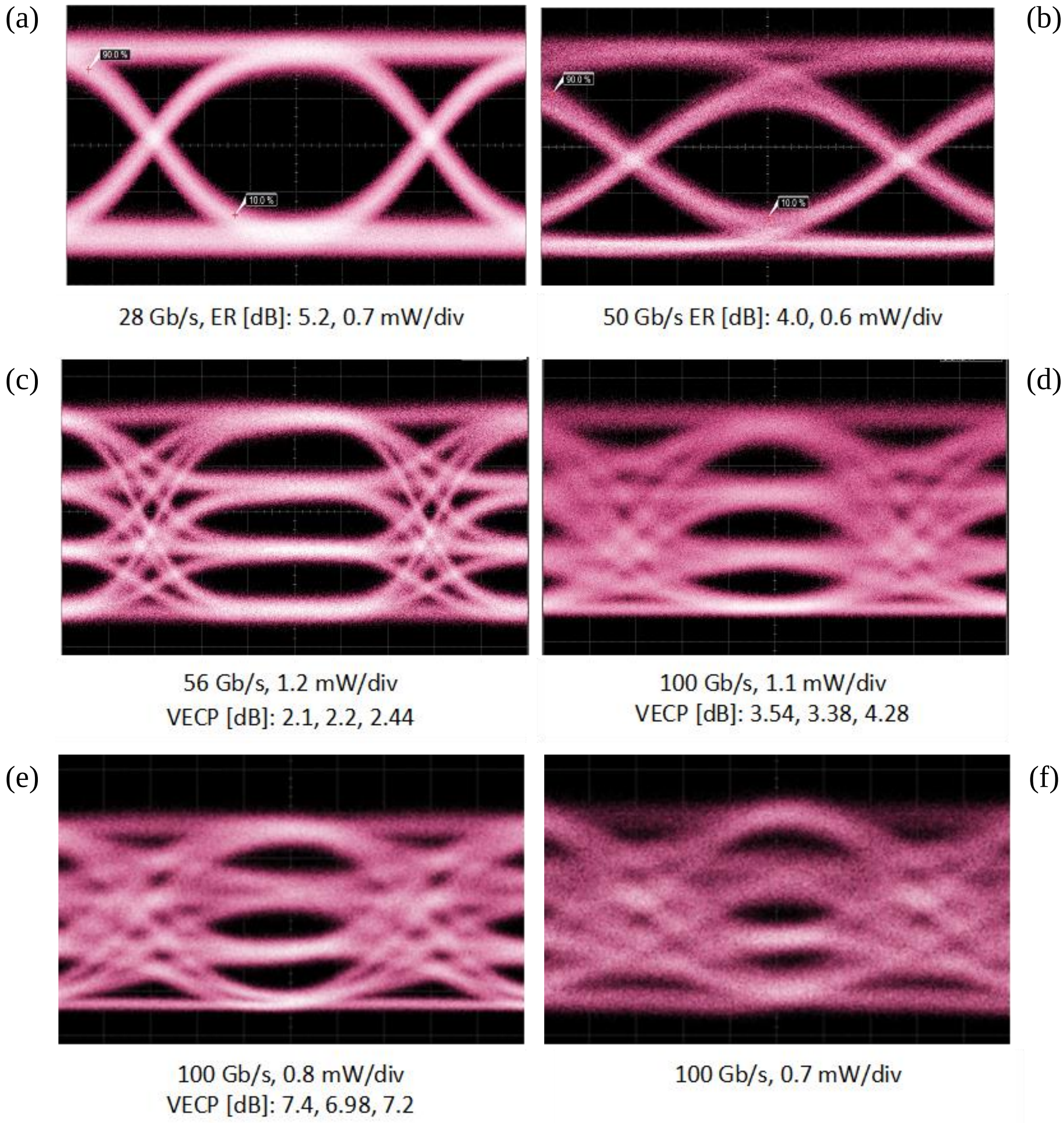

Fig. 20. Back to back (a) 28 Gbaud PAM-2; (b) 50 Gbaud PAM-2; (c) 28 Gbaud PAM-4 (d); 50 Gbaud PAM-4; (e) 50 Gbaud PAM-4 after 2 km and (f) 50 Gbaud PAM-4 after 5 km.

The eye diagrams presented in Fig. 20 confirm that the biasing and RF amplitude swings of each MZM result in 4 equally spaced power levels. The BER of the transmission system is estimated by assuming Gaussian distribution of each level [85]. To have a better quantitative evaluation of the device’s transmission performance, we numerically calculate the BER of the device for various PAM-4 baud rates using the method presented in [85]. The median power and distribution of each PAM-4 level were measured from the eye diagrams after collecting enough samples. Figure 21, demonstrates the estimated BER for different baud rates. We further propagate the modulated signal through various lengths of SMF 28 fiber. A successful 50 Gbaud transmission of PAM-4 over 2 km of SMF below pre-FEC hard decision threshold of 4.4×10^{-3} is achieved [110]. Considering the 7% over head of the FEC, the transmitted payload is 46.5 Gbaud. The measured negative chirp of the device is beneficial in eliminating the effects of SMF dispersion.

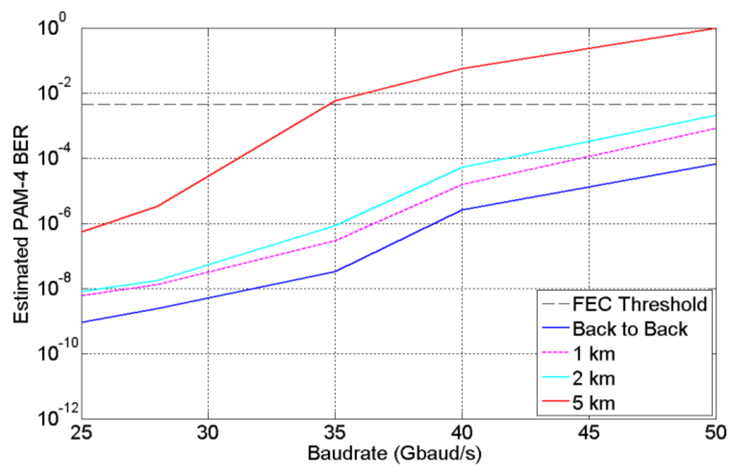

Fig. 21. Estimated BER of PAM-4 modulation versus baud rate after various fiber propagation lengths.

4.4 Conclusions

In this chapter, we use a similar DP-MZM structure as the previous chapter. However, we use the modulator for on-chip generation of PAM-4 signals. We present the detail design of the device and discuss the driving method used to generate PAM-4 signals using the DP-MZM. We experimentally study the differential and integral non-linearity of the modulator, and present methods to optimize the modulator operation and achieve equidistant PAM-4 amplitude levels. We characterize the chirp of the modulator to assess the impact of phase modulation on the performance of the device. And finally, we achieve a pre-HD-FEC error free 100 Gb/s single wavelength PAM-4 transmission through 2 km of SMF without any DSP and dispersion compensation. The study presented in this chapter, provides a compelling argument for modifying the modulator structures for higher order modulation formats such as PAM-4, in opposed to relying on electrical DACs for generating high order modulation formants.

Chapter 5

Multi Electrode Mach-Zehnder Modulator

In this Chapter, we present PAM-4 generation and transmission in the C-band using a SiP SPP Multi-Electrode Mach-Zehnder modulator (**ME-MZM**) with a 3-dB EO bandwidth greater than 45 GHz. We present the analytical study of the modulator, and its small and large signal characterization. The linearity of the transfer function of the ME-MZM along with the PN junction phase shifters are investigated. We next experimentally demonstrate the generation of 168 Gb/s PAM-4 signals using the ME-MZM driven by two OOK electrical signals which are conditioned using minimal DSP which includes pulse shaping at symbol rates up to 84 Gbaud, RF spectral pre-compensation filter, clipping, and quantization. Furthermore, we investigate the transmission performance of the ME-MZM compared to a conventional SiP SPP TWMZM over various lengths of fiber. This allows us to quantitatively compare the PAM-4 signal generation in optical domain achieved by utilizing the ME-MZM, versus TWMZM which requires the PAM-4 signal to be generated in electrical domain. Additionally, we experimentally demonstrate that by utilizing ME-MZM functionality which requires only OOK drive signals, higher baud PAM-4 generation can be achieved. We further present the power consumption per bit of each modulator for various bitrates and modulation formats. The result of this analysis shows that ME-MZM offers a more efficient solution for higher baud PAM-4 compared to TWMZM.

5.1 Device Design and Characterization

The schematic of the structure and the analytical model of a loss less ME-MZM are presented in Fig. 22.

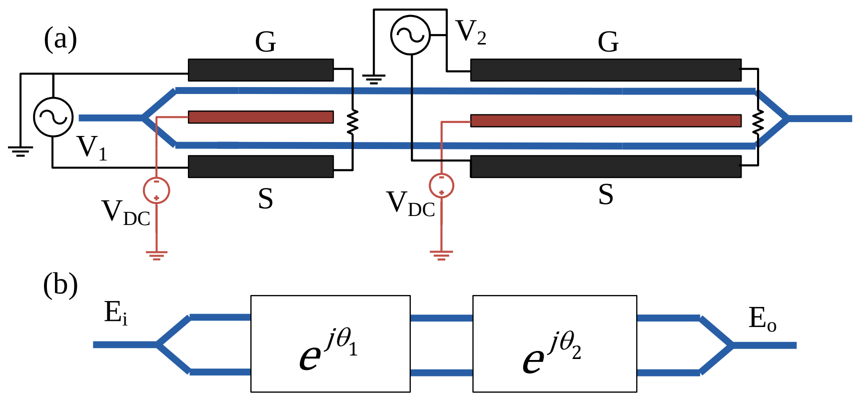

Fig. 22. (a) The schematic of the ME-MZM and (b) analytical model of a SPP ME-MZM.

Since the two segments of the ME-MZM can be driven independently, the output electric field of ME-MZM can be written as:

$$E_o = \frac{E_i}{2} e^{j(\theta_1+\theta_2)} \tag{6}$$

where, E_i is the input electric field, θ_1 and θ_2 are the phase changes from modulating each segment. From (6), the output light intensity of the ME-MZM, ignoring loss, is:

$$I_o = \frac{|E_i|^2}{2}(1+\cos(\theta_1+\theta_2)) \tag{7}$$

Since each individual segment of the ME-MZM can be driven independently, the device can operate as a 2 bit optical digital to analog convertor (**DAC**) to generate PAM-4 signals while driven by two OOK (binary) electrical signals. Ideally, when both segments of the ME-MZM are driven by the signals with the same peak to peak amplitude, the phase shift value of the longer segment would be double that of the shorter segment. The optical power transmission of an ideal (i.e. linear and loss less) ME-MZM as a function of the phase shift of each segment is shown in Fig. 23 (a). Figure 23 (b) shows the transfer function of ME-MZM. As shown in Fig. 23 (a), the transfer function of a MZM is sinusoidal. To improve the linearity of the modulator and to realize equally spaced PAM-4 amplitude levels, the drive voltage dynamic range (**DR**) should be adjusted to the linear region of the transfer function [73]. This is achieved by properly biasing the segments of the ME-MZM to the midpoint of the transfer function as well as reducing the drive voltages of each segment. By limiting the DR of the modulator to 0.6π as shown in Fig. 23 (b) using the red dashed line the differential and integral non-linearity of the ME-MZM are improved from 0.44 and 0.27 (full DR) to 0.146 and 0.09.

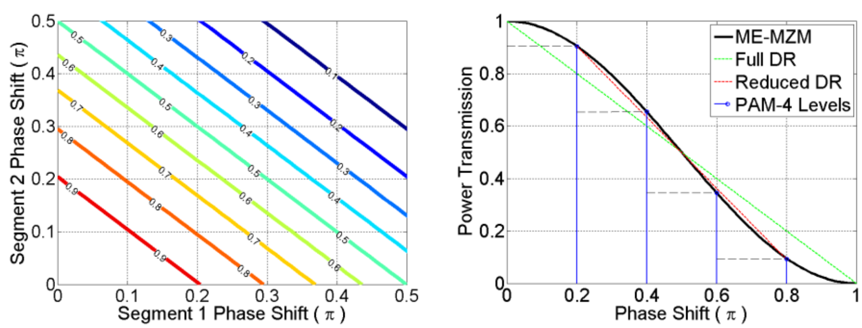

Fig. 23. The optical power transmission of a lossless linear ME-MZM as a function of (a) the phase shift of each segment and (b) total phase shift of a ME-MZM with linear phase shifters.

Figure 24 illustrates the micrograph of the ME-MZM and TWMZM. The electrode design and the PN junction of the modulators are identical to each other and are presented in detail in my master thesis [71] and in [70]. Both devices were fabricated on a SOI wafer, with a 220 nm silicon layer thickness and a 2 μm thick buried oxide layer in the same fabrication run at IME A*STAR. The ME-MZM is designed such that equally spaced PAM-4 amplitude levels are achieved using two binary electrical driving signals with the same peak to peak amplitude. To implement this, the longer segment of the ME-MZM is twice the length of the shorter segment. This ideally will result in the longer segment having a Vπ value that is one half of the shorter segment's Vπ.

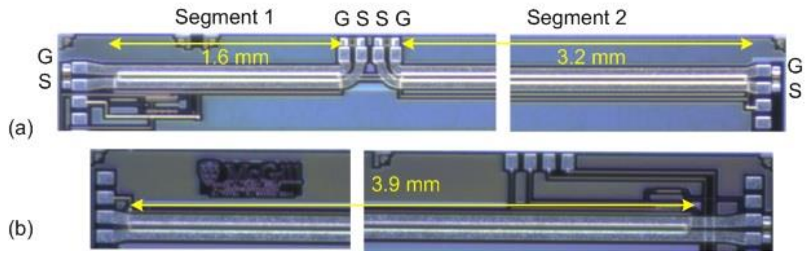

Fig. 24. Micrograph of (a) the ME-MZM and (b) the TWMZM.

Figure 25 (a) illustrates the measured phase shift for each segment of the ME-MZM and the TWMZM. Ideally, when both segments of the ME-MZM are driven by the signals with the same peak to peak amplitude, the phase shift value of the longer segment would be double that of the shorter segment. However, from Fig. 25 (a) it is clear that SiP phase shifters are not linear. We reconstruct Fig. 23 with the measured phase shift values of the ME-MZM not considering propagation losses. The optical power transmission of the ME-MZM as a function of the phase shift of each segment and the transfer function of the ME-MZM is shown in Figs. 25 (b) and 25 (c), respectively. By limiting the DR of the modulator to 0.6π (as shown in Fig. 25 (c) using the red dashed line) the integral and differential non-linearity of the SiP ME-MZM as a 2-bit DAC are 0.315 and 0.35 for full DR and 0.15 and 0.075 for the operating DR presented in Fig. 25 (c), respectively. Interestingly these values of INL and DNL are slightly better than an ideal case. This is due to the fact that the transfer function of the SiP ME-MZM is more linear between 0.2 Vπ - 0.8 Vπ than the ideal case.

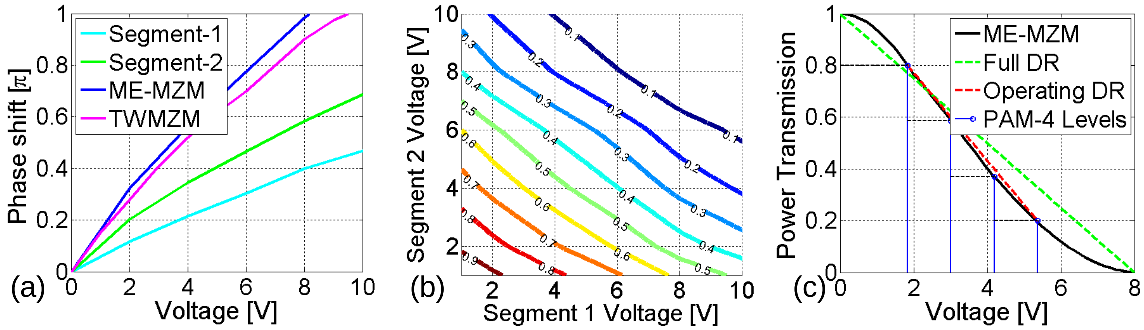

Fig. 25. Measured values of the: (a) Phase shift vs. voltage of ME-MZM and TWMZM, (b) the optical power transmission of the presented ME-MZM as a function of the voltage applied to each segment and (c) transfer function of the SiP ME-MZM (ignoring losses).

The insertion loss of the ME-MZM and TWMZM are measured to be 4.3 and 3.3 dB, respectively. Vertical shallow etched grating couplers are used to couple light in and out of the SiP chip. A 14 dBm tunable laser is used as an input for the modulators. All travelling wave electrodes of both modulators are terminated using external 50 GHz, 50 Ω termination through the RF probes. A 200 μm intrinsic section is placed between the two phase-shifter segments of the ME-MZM, to isolate the two segments and accommodate the input and termination of each electrode. The electro-optic response of each segment of the ME-MZM are measured using a LCA and are shown in Fig. 26 (a). Similarly, the EO S21 response of the TWMZM is shown in Fig. 26 (b). The electrical input of the modulator is connected to the RF port 1 of the LCA, and the modulated output optical signal is connected to the optical receiver port of the LCA. The noise floor of the LCA's measurements is reported to be < - 59 dB (W/A) at 50 GHz for EO measurements. Due to the shorter length of the ME-MZM electrodes, lower microwave attenuation and lower velocity mismatch, the EO 3-dB bandwidth of the ME-MZM segments are significantly higher than that of the TWMZM. In addition, due the extra electrode routing, the total electrode length of the TWMZM is 4.5 mm which results in higher loss. Consequently, the higher achievable bandwidth of the ME-MZM will allow the modulator to achieve higher modulation rates. It should be noted that by decreasing the length of the TWMZM the bandwidth of the device can be improved however this will result in higher Vπ. The electrical S11 of the ME-MZM segments and the TWMZM are shown in Figs. 26 (c) and 26 (d) respectively. The S11 measurements of both modulators are well below -10 dBm. Which confirms both modulators' characteristic impedance is close to the targeted 50 Ω impedance.

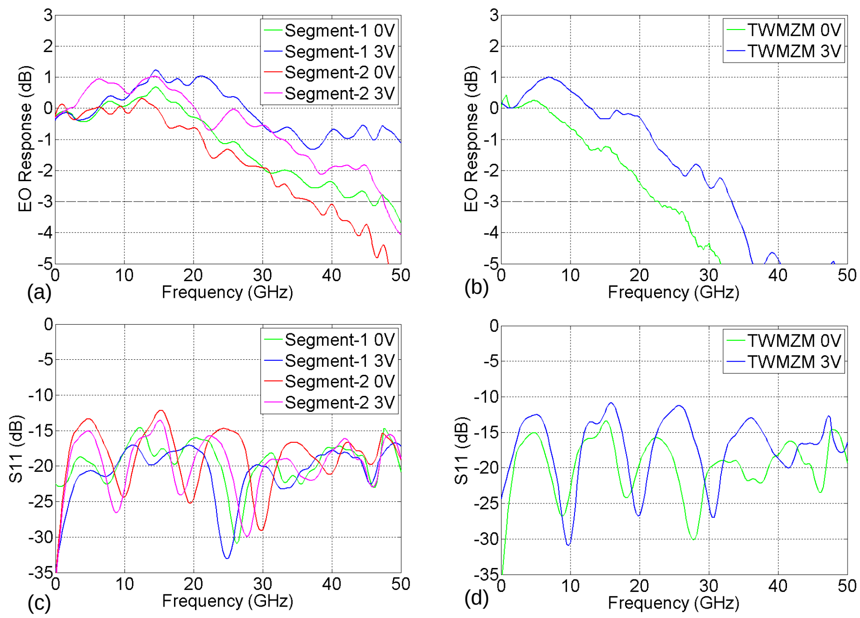

Fig. 26. Electro-optic response of the (a) ME-MZM and (b) TWMZM, and the electrical S11 response of the (c) ME-MZM and (d) TWMZM

5.2 Large Signal and Transmission Experiment

As recent studies have shown, using DSP is a possible and in some cases necessary solution to achieve 50 Gbaud PAM-4 transmission [85-86]. In this section we compare the performance of both modulators and particularly focus on the transmission improvement achieved using DSP on the transmitted and received signal. We parametrically investigate the large signal transmission performance of the TWMZM and ME-MZM under two conditions. First in condition 1, the large signal performance of the devices without any DSP is presented, using a pulse pattern generator (PPG) to operate the modulators. In this setup, we use the optical sampling head of the digital communication analyzer (**DCA**) as the receiver as shown in Figs. 27 (a)- 27(c). Next in condition 2, we present the large signal performance with offline DSP using an electrical DAC and an analog-to-digital convertor (**ADC**). The transmission performance of the devices is investigated by applying DSP on both the transmitted signal and the received signal. To perform error counting and apply DSP on the received signal in condition 2, instead of the DCA, a 50 GHz, 0.65 A/W photodetector is used for the optical to electrical conversion, and a real-time oscilloscope is used to capture the transmitted data and perform error counting. In condition 1, we use binary electrical signals to drive the modulator, hence in the case of the TWMZM, PAM-4 operation could not be achieved. In the second condition, we investigate the PAM-4 performance of each device. Specifically, we investigate the quality of the signals when the PAM-4 levels are generated in the electrical domain using the electrical DAC and they are applied to the TWMZM versus when the PAM-4 levels are generated in the optical domain using the ME-MZM structure.

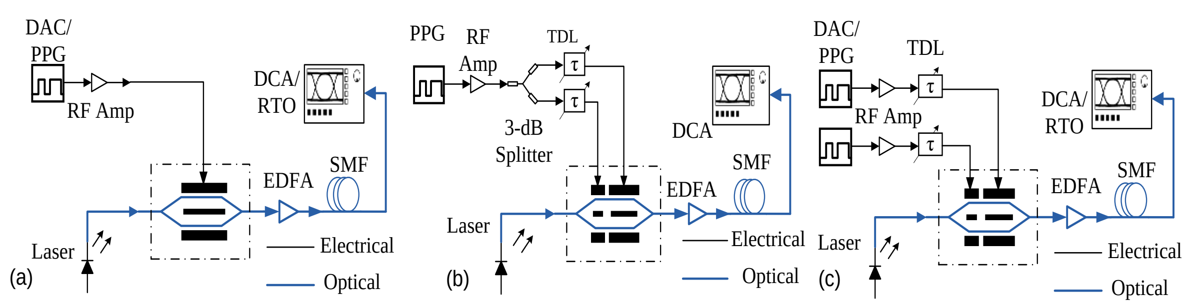

Fig. 27. Schematic of the experimental setup for (a) OOK and PAM-4 modulation using TWMZM (b) OOK modulation using ME-MZM and (c) PAM-4 modulation using ME-MZM.

5.2.1 Condition 1: Transmission without DSP

For OOK transmission in condition 1, a pseudo random bit sequence (**PRBS**)-31 signal from the PPG is amplified using a 40 GHz RF amplifier. In the case of the TWMZM, the driving signal is applied directly to the modulator after amplification. Figure 27 (a) illustrates the experimental setup schematic for OOK modulation using the TWMZM. When driving the ME-MZM as shown in Fig. 27 (b), a single OOK signal is divided into two branches using a 50 GHz 3-dB splitter. Matched RF cables and RF amplifiers are used to ensure that both signals have the same RF path length and tunable delay lines are used to time align the two signals such that the signal driving the second segment has a delay equal to the length of the first segment plus the intrinsic section separating the two segments. This delay can be calculated by dividing the first segment length (1.6 mm) plus the intrinsic section (0.2 mm) by group velocity of the optical mode. In this configuration, both segments are operated using the same driving voltage. Fig. 27 (c) describes the configuration used to generate PAM-4 signals using the ME-MZM. In this scenario, two independent OOK PRBS signals are generated using the PPG and applied to each segment of the ME-MZM. To compensate for the nonlinearity of the phase shifters shown in Fig. 25 (a) and to obtain equally spaced PAM-4 levels, the drive signal for the longer segment is amplified to 5 Vpp and the signal driving the shorter segment is amplified to 3.8 Vpp. Both segments of the modulator are biased at 3.5 V. The RF tunable delay lines are used to time align each signal visually using the DCA such that the bit transition of each signal overlaps. In all three configurations the modulated optical signal was then amplified using an EDFA, and propagated through various lengths of fiber. The 80 GHz optical sampling head of the DCA is used as the receiver. The received optical power is kept constant at 5 dBm. Figure 28 demonstrates the OOK eye diagrams of both the ME-MZM and TWMZM and the PAM4 eye diagram of ME-MZM at 40 Gbaud with their corresponding measured Q-factor and vertical eye closure penalty (**VECP**) values.

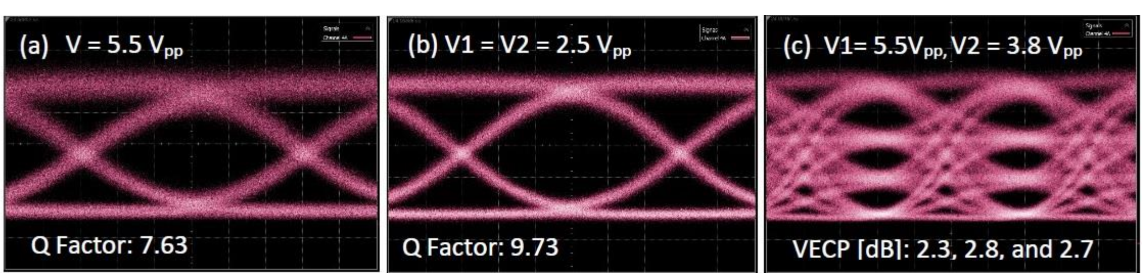

Fig. 28. 40 Gbaud OOK eye diagram of (a) TWMMZM (b) ME-MZM and (c) PAM-4 eye diagram of ME-MZM.

As shown in Section 5.1 the higher bandwidth of the ME-MZM and longer effective phase shifter length should allow it to reach higher baud rates compared to the TWMZM, however to properly compare the two modulators we need to consider the operating conditions and the drive voltages applied to each modulator. To quantify the performance of each modulator under various drive voltages and symbol rates, we measure the Q-factor of the OOK eye diagram using the DCA. Additionally, for the PAM-4 modulation using ME-MZM, we estimate the BER performance at various symbol rates and transmission distances using the method presented in [85]. Figure 29 (a) and 29 (b) present the back to back OOK Q-factor of each modulator and Fig. 29 (c) shows the PAM-4 BER of the ME-MZM over various fiber lengths. The dashed horizontal black lines in Figs. 29 (b) and 29 (c) represent the KP4 HD-FEC threshold at 2.0×10^{-4}. When using OOK modulation, the bias voltage applied to both modulators is adjusted to Vpp/2 + 0.5 V to ensure that PN junctions are always in reverse bias. Referring to Fig. 29 (a) it can be seen that the ME-MZM achieves a significantly higher Q factor than the TWMZM at the same drive voltages, however it should be noted that the ME-MZM is operated using 2 drive signals. The better performance of the ME-MZM can be attributed to its longer overall phase shifter length (approximately 1 mm longer) and the lower microwave loss of each segment compared to the TWMZM. In Fig. 29 (c) the drive voltages for the short and long segments of the ME-MZM are 3.8 and 5 Vpp, and we achieve a 50 Gbaud below FEC, PAM-4 transmission over 1 km of fiber without any DSP. We attribute the better performance of the modulator through 500 m of fiber compared to back to back transmission to the small negative chirp of the SPP modulators which results in compensating the fiber chromatic dispersion in fiber [70, 72]. These measurement results will be compared to the condition 2 results in the next section to quantify the improvement achieve using DSP.

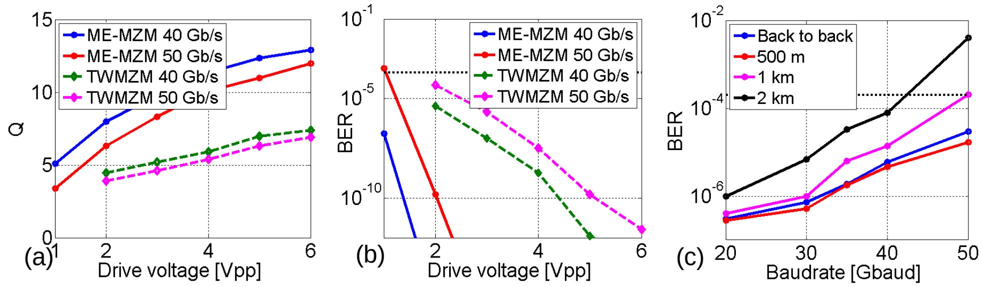

Fig. 29. Back to Back OOK Q-factor of (a) ME-MZM and TWMZM, (b) OOK BER of ME-MZM and TWMZM and (c) the PAM-4 BER of ME-MZM over various length of SMF.

5.2.2 Condition 2: Transmission with DSP

In condition 2, the PPG is replaced by the DAC as shown in Figs. 27 (a) and 27 (c). This study will allow us to quantify the improvements achieved by using DSP on transmission performance of each modulator. For OOK modulation, two identical PRBS signals are generated using two DAC channels. Matched RF cables along with TDLs are used to ensure that the signals are time aligned. In this scheme, the RF 3-dB splitter is not required as the DAC can generate identical PRBS signals on different channels. The DAC operates at 1 sample per symbol at 84 GSamples/s. The transmitter DSP includes, symbol generation, pulse shaping at symbol rates up to 84 Gbaud, RF spectral pre-compensation filter up to the RF amplifier outputs, clipping, and quantization [111]. It is to be noted that pulse-shaping at 84 Gbaud is performed by the DAC with an appropriately chosen equalizer and without intentional pulse shaping in the digital domain. For PAM-4 transmission using TWMZM, the signal amplitude levels are adjusted using the DAC to compensate for the MZM transfer function and the RF amplifier’s gain non-linearity. The generated signal is amplified to 5.5 Vpp and applied to the modulator. On the receiver side, we replace the DCA with a 50 GHz, 0.65 A/W photodetector for optical to electrical conversion and a 63 GHz real time oscilloscope (**RTO**) to capture the modulated signals and store it for the offline receiver DSP and error counting. The receiver DSP consists of: sampling the signal at 160 GSa/s, matched filtering at 2 × baud rate, clock recovery, followed by receiver equalizer and symbol decision. The received eye diagrams are generated offline using MATLAB. The driving signal amplitudes for 56 Gbaud are the same as the condition 1; however due to stronger equalization at 84 Gbaud, the maximum achievable peak-to-peak voltage after the RF amplifiers is 4 Vpp and as a result for PAM-4, the binary electrical signals applied to the shorter and longer segments are 3 and 4 Vpp, respectively. For OOK generation, the two signals driving each segment have the same amplitude. Figure 30 shows OOK and PAM-4 eye diagram of the ME-MZM at 56, and 84 Gbaud.

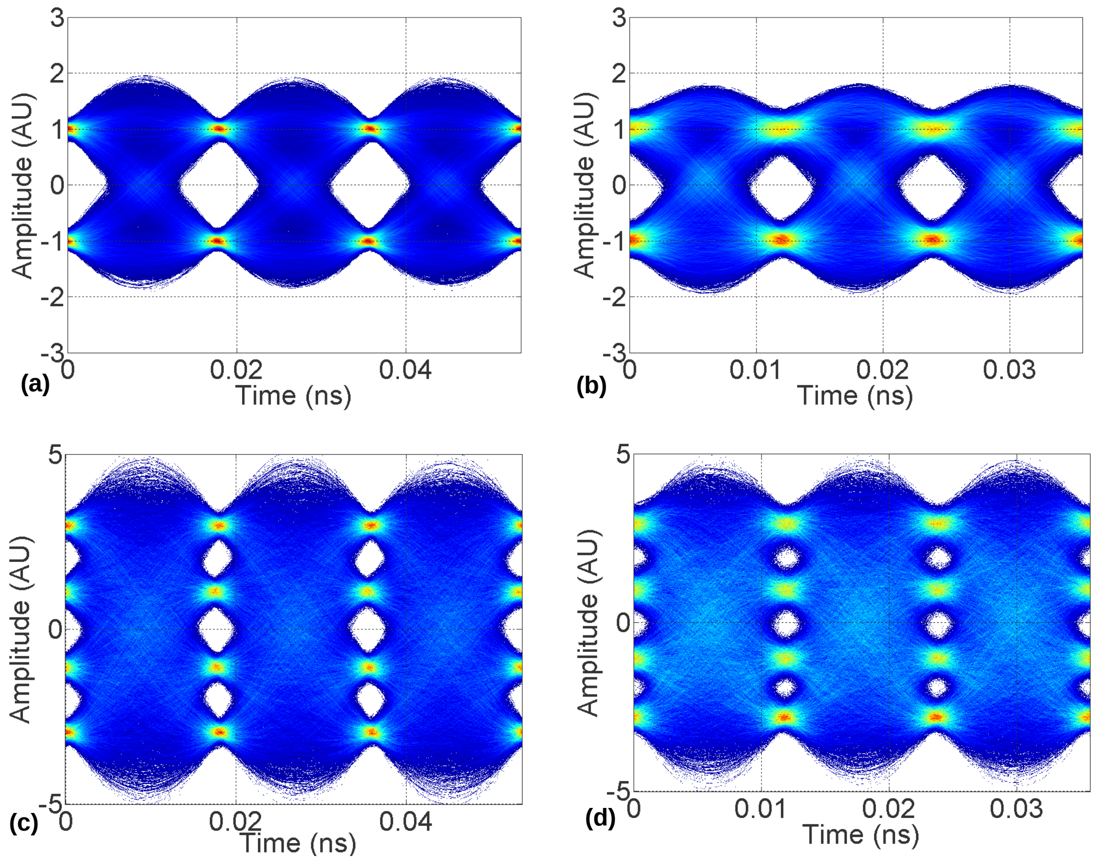

Fig. 30. (a) 56 Gbaud OOK, (b) 84 Gbaud OOK, (c) 56 Gbaud PAM-4 and (d) 84 Gbaud PAM-4 eye diagram of the ME-MZM.

Using the receiver DSP, we can further optimize the vertical decision-making threshold for each PAM-4 level hence improving the performance of each device. We experimentally study three main parameters of the transmission system: 1) the modulator driving voltage, 2) the modulation baud rate and 3) the transmission distance for PAM-4. As shown in Fig. 31, both modulators are capable of 84 Gbaud OOK transmission with Q factors that correspond to a BER below the FEC threshold. Figure 31 (a) shows the 84 Gbaud OOK BER performance of each device for various transmission lengths and drive voltages. As demonstrated, ME-MZM performs noticeably better than the TWMZM. Similarly, we investigate the PAM-4 transmission performance of both devices for various baud rates and drive voltages in Fig. 31(b) and 31(c). It can be seen from Figs. 29 and 31, that using DSP, both modulators can be operated using lower drive voltages yet maintain the same BER performance.

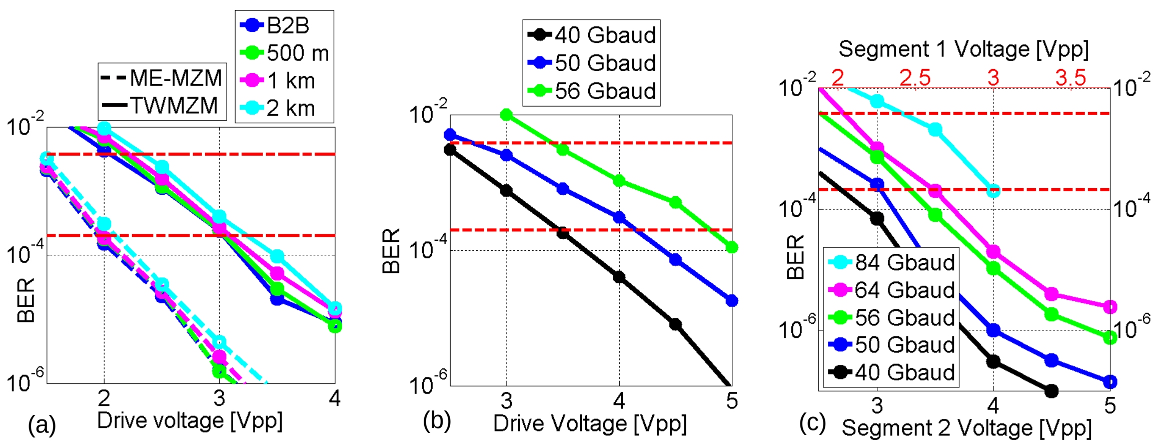

Fig. 31. OOK BER of (a) ME-MZM and TWMZM over various length of SMF, (b) PAM-4 BER of TWMZM, and (c) the PAM-4 BER of ME-MZM versus drive voltage. Dashed lines indicate the HD-FEC threshold of 3.8×10^{-3} and the KP-4 FEC threshold of 2.0×10^{-4}.

Several factors contribute to superior performance of the ME-MZM compared to TWMZM. First, the lower microwave loss of ME-MZM electrodes enable higher symbol rate operation compared to TWMZM. Additionally, the smaller length of the electrodes results in a lower velocity mismatch between the optical and microwave signals resulting in higher EO bandwidth. We also note that the overall total phase shifter length of the ME-MZM is longer than the TWMZM, which results in a lower Vπ for the device. However, this increase in length results in higher insertion loss compared to TWMZM.

As shown in Section 5.1, ME-MZM generates PAM-4 signals by combining two OOK electrical driving signals in the optical domain. It should be noted that, in the electrical domain, the PAM-4 drive signals that the DAC generates have lower Q-factor than the OOK drive signals; as a result, the ME-MZM performs better since its structure enables it to be driven by better quality drive signal. With the ME-MZM, we achieve an 84 Gbaud PAM-4 generation below the KP-4 FEC threshold of 2.0×10^{-4}, which to the best of our knowledge, is the highest baud rate ever reported using a silicon photonic modulator. We further examine the transmission performance of the two devices over various lengths of single mode fiber. Figure 32 presents the BER performance of the system for various bauds and transmission distances. Two OOK signals of 4 Vpp and 3 Vpp, amplitude are applied to the longer and shorter segment of the ME-MZM respectively, and the TWMZM is driven by a 5 Vpp PAM-4 signal

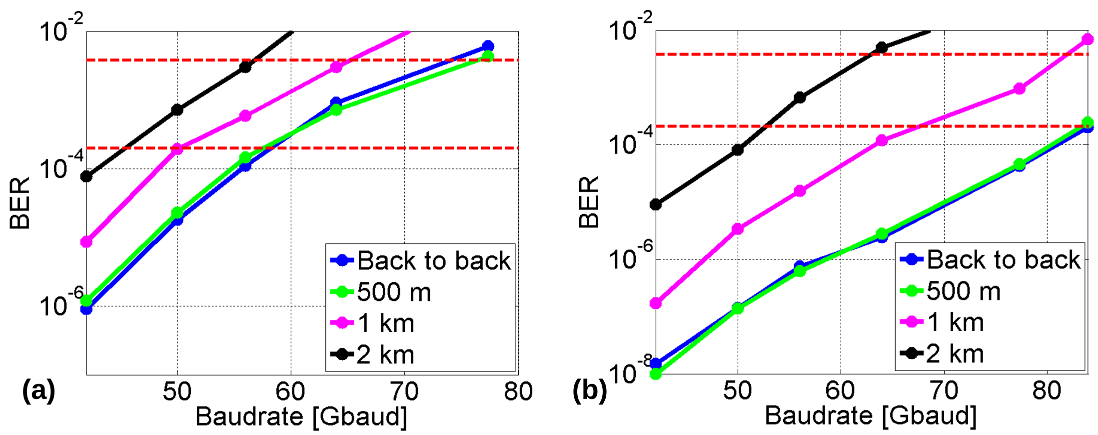

Fig. 32. BER performance of the (a) TWMZM and (b) ME-MZM for various bauds and transmission distances. Dashed lines indicate the HD-FEC threshold of 3.8×10^{-3} and the KP-4 FEC threshold of 2.0×10^{-4}.

Using the ME-MZM, we report a successful transmission of 56 Gbaud PAM-4 signal over 1 km of SMF below KP4 FEC threshold. As both devices are designed for C-band operation, at higher distances, the BER is significantly affected by the fiber chromatic dispersion. We expect an O-band device to perform considerably better at higher distances.

Assuming the energy consumption is dominated by the resistive loss, we estimate the energy per bit consumption of both modulators using the method shown in [80]. The energy consumed by each electrode can be estimated by $P = \sum_{i=1}^{N} \frac{V_{i,RMS}^2}{R}$, where, N is the number of segments or electrodes and V_{rms} is the root-mean-square of the voltage driving the i^{th} segment. Table I presents the lowest energy consumption per bit (pJ/bit) of each modulator at different bauds achieving a BER below the KP4 FEC threshold. It is to be noted that the energy consumption reported is only for the modulator itself.

Table I. Power consumption per bit (pJ/bit) of each modulator.

Baud [Gbaud]	ME-MZM				TWMZM			
	OOK, V_{rms1}, V_{rms2} [V]	OOK (pJ/bit)	PAM-4, V_{rms1}, V_{rms2} [V]	PAM-4 (pJ/bit)	OOK, V_{rms} [V]	OOK (pJ/bit)	PAM-4 , V_{rms} [V]	PAM-4 (pJ/bit)
40	0.53, 0.53	0.28	1.06, 0.80	0.44	0.70	.25	.24	.38
50	0.53, 0.53	0.22	1.23, 0.88	0.46	0.70	.2	.59	.51
56	0.53, 0.53	0.20	1.23, 0.88	0.41	0.70	.18	.767	.56

It can be seen that at lower bauds, and OOK format, TWMZM provides a more efficient option compared to ME-MZM. This is due to that fact that ME-MZM requires 2 driving signals. However, using PAM-4 modulation and higher bauds, ME-MZM provides an advantage over TWMZM. At 56 Gbaud PAM-4 the ME-MZM energy consumption per bit is estimated to be 0.41 pJ/bit while TWMZM's power consumption is 0.56 pJ/bit. To achieve a higher PAM-4 baud using a TWMZM, a significantly higher drive voltage is required to compensate for the lower bandwidth of the device. However, ME-MZM can be driven by considerably lower drive voltages. Furthermore, the length of the ME-MZM segments can be optimized for a certain baud to allow for the most efficient power consumption.

5.3 Conclusions

In this chapter, we present the design, analysis and transmission performance of a multi electrode Mach Zenhnder modulator for multi amplitude optical signal generation. We achieve the highest reported PAM-4 signal generation of 168 Gb/s using 2 OOK electrical drive signals using DSP. We further investigate the transmission properties of the device under various driving conditions and compare the performance of the device with a similar TWMZM. We experimentally show that ME-MZM structure enables higher baudrate transmission due to its higher EO bandwidth compared to a similar single electrode TWMZM. Without any digital signal processing and using a conventional PPG, the ME-MZM is capable of generating 100 Gb/s PAM-4 signal.

Chapter 6

Silicon Photonic Mach-Zehnder Modulator Architectures for on Chip PAM-4 Signal Generation and Transmission

6.1 Introduction

In this chapter, we present four O-band Silicon photonic (SiP) modulators based on 3 different Mach-Zehnder interferometer structures presented in previous chapters, to generate multi-amplitude modulation formats. Each modulator is capable of 112 Gb/s PAM-4 transmission below the HD-FEC threshold of 3.8×10^{-3}. We investigate and compare the performance advantages of generating PAM-4 using various structures of MZM optically as opposed to generating PAM-4 in the electrical domain using conventional electrical DACs and MZMs. The two variants of optical DACs are a DP-MZM with one series push pull TWMZM on each arm, and a ME-MZM. As the objective of this chapter is to accurately assess the performance of each modulator structure and identify a optimized design, we have made several changes to the DP-MZM and ME-MZMs that were presented in previous chapters. Further we explore the advantages and disadvantages of each architecture for PAM-4. First, we present the optical design of the modulators and investigate the effects of non-linearities of the MZM transfer function and PN junction phase-shifters on performance of the PAM-4 generation for each modulator architecture. Next, we examine the effects of microwave loss and 3-dB bandwidth (BW) on the overall performance of the modulators for the updated phase shifter and travelling wave electrode lengths. We use the simple figure of merit BW/V_π, to compare the performance of the modulators for specific baudrates and drive-voltages. Finally, we parametrically examine the transmission performance of each modulator and present an optimized modulator design for DAC -less and DSP less 112 Gb/s PAM-4 transmission. Furthermore, we present the highest transmitted symbol rate using an O-band SiP modulator reported to date.

6.2 Device Design, Fabrication and Characterization

We investigate the PAM-4 performance of three different types of Mach-Zehdner modulator structures that were presented in the previous chapters, namely the TWMZM, DP-MZM and ME-MZM. All modulators are designed and driven in series-push pull (SPP) scheme as detailed in chapter 2 and [70], where a positive phase shift in one arm is accompanied by a negative phase shift of equal strength in the other arm. One advantage of the SPP MZM is that it requires one RF signal to drive the modulator. This noticeably lowers the system complexity, when operating the DP-MZM and the ME-MZM for PAM-4 modulations, since addition of any RF signal requires further microwave analysis and can trigger unwanted cross talk between channels. All presented modulators are designed for the transmission of 112 Gb/s PAM-4 on a single carrier. Consequently, the main target specification for our designs is to have EO bandwidth for each modulator ≥ 35 GHz. This benchmark bandwidth value is chosen based on the target baudrate, PAM-4 spectral efficiency and considering our transmission system components, such as RF amplifiers and photodetectors. It should be mentioned that, this bandwidth can be further optimized for specific symbol rate, and driver circuitry. To unbiasedly evaluate the performance of different modulator structures we use the same phase shifter and electrode design for all three types of modulators. As a result, we present four modulators as follows: a) TWMZM with 3mm long phase shifter, b) a DP-MZM with 3 mm long inner TWMZMs, c) a ME-MZM with two, 1.5 mm long phase shifters and finally d) ME-MZM with two 3 mm long phase shifters. We present two ME-MZM variations to be able to unbiasedly compare the performance of the three types of modulators. The shorter ME-MZM has the same phase shifter length and hence the same $V\pi$ as the TWMZM and DP-MZM, while the longer ME-MZM has the same electrode length and hence similar bandwidth as the presented TWMZM and DP-MZM. The schematic of the all three modulators types is shown in Fig. 33. Two vertical grating couplers are used to couple light in and out of the SiP chip. Back to back insertion loss of the two GCs is measured to be 9.5 dB. A low-loss, compact Y-branches are used as splitters/combiners to form the interferometer. A resistive thermo-optic tuner is used to control the phase and biasing of the modulators. The insertion loss of the TWMZM, DP-MZM, shorter ME-MZM and longer ME-MZM are measured to be 3.3, 4.1, 3.4 and 6.3 dB, respectively.

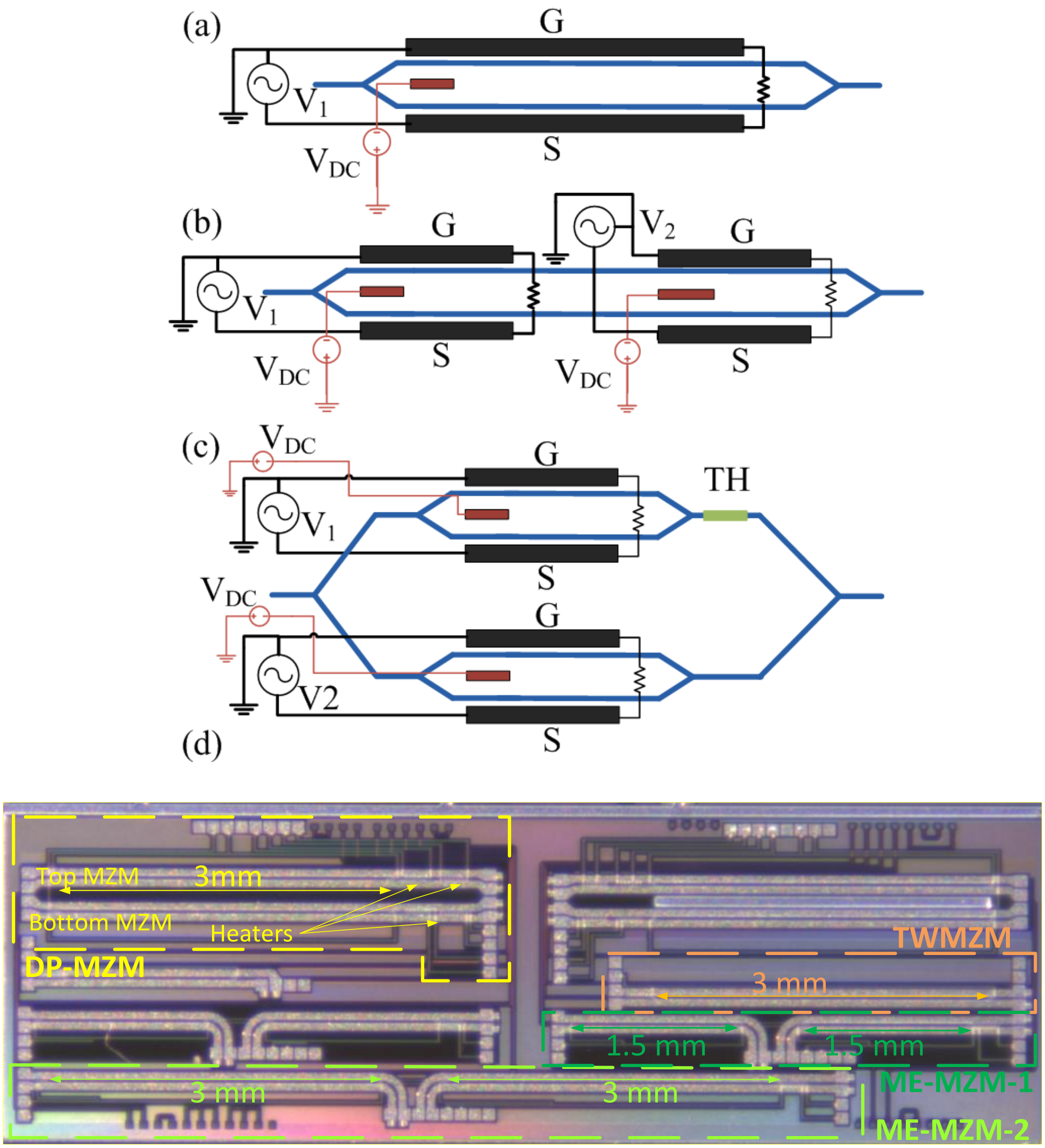

Fig. 33. a) Schematic of a) TWMZM, b) ME-MZM, c) DP-MZM and d) Micrograph of the silicon photonic chip. (TH: Thermo-optic tuner)

6.2.1 PN Junctions

In this section we review the optical design of the modulators and point out few updates that were applied to the modulators compared to the ones presented in the previous chapters. All four modulators were fabricated on a SOI wafer with a 220-nm thick silicon layer, a 2 μm thick buried oxide layer and a high resistivity 750 Ω-cm silicon substrate in the same multi-project wafer run at IME-A*STAR. The PN junction cross section of all modulators are similar to the cross section presented in Fig. 1 presented in chapter 2. However, the dimensions of the modulators have been slightly updated from the values presented in the previous chapters to further optimize the performance of the modulators at O-band. Table II shows the values for all the dimensions noted in Fig 1. To reduce optical propagation losses in the waveguides at 1310 nm, the width of the rib waveguides was set at 400 nm which is slightly wider than a strictly single mode waveguide with 220 nm height at O-band. Intrinsic regions are inserted periodically with fill factor of 90% along the phase shifter to minimize the current flow in the longitudinal direction (normal to the picture).

Table II. Waveguide and PN junction dimensions.

Dimension	Value	Dimension	Value
W_{rib}	0.4 µm	H_{rib}	0.22 µm
W_{n++}	7 µm	H_{slab}	0.09 µm
W_{n+}	0.78 µm	H_{metal}	2 µm
W_n	0.42 µm	L_{pn}	18 µm
W_{P++}	28.6 µm	$L_{intrinsic}$	2 µm
W_{p+}	0.8 µm	Λ	90%
W_p	0.4 µm	H_{BOX}	2 µm

The highly doped levels (P++ and N++) are used to create ohmic contacts, and the intermediate doping levels (P+ and N+) are used to reduce series resistance of the PN junction and minimize the optical losses due to high concentration of dopants since. The intermediate doping levels have negligible effect on the capacitance of the junctions since the capacitance is created mainly at the junction of P and N. Furthermore, the intermediate doping levels can be used to optimize the microwave losses by adding an extra level of control to the series resistance of the junctions. On the other hand, the change in effective index and loss due to the plasma dispersion effect is dictated by the P and N doping levels due to the optical mode being tightly confined near the waveguide core. The peak concentration of the P and N for this process are 7×10^{17} cm^{-3} and 5×10^{17} cm^{-3}, respectively [107]. Fig 34 shows the measured phase-shift versus applied voltages for 1.5 mm, 3 mm and 6 mm long phase shifters. The measurements are taken at 1310 nm.

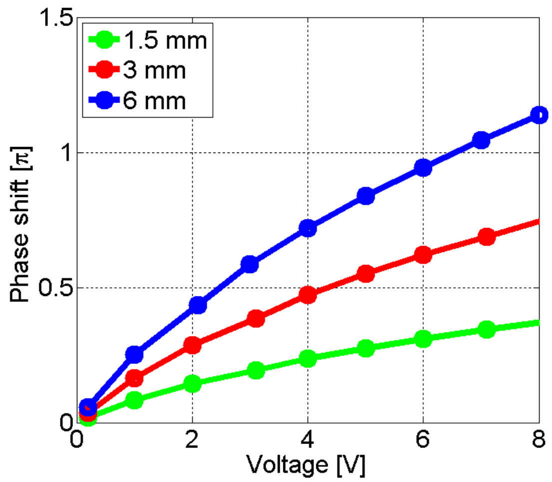

Fig. 34. Phase shift versus voltage of various phase shifter lengths.

As seen in Fig. 34 the phase shift due to plasma dispersion effect does not increase linearly with applied voltage. This non-linearity is measured to be more pronounced in the O-band compared to the C-band. Furthermore, beyond 8V reverse bias, the width of the PN junction depletion region does not change drastically, therefore the change in concentration of the carriers which induces change in n_{eff} of the waveguide is very small. Consequently, the phase change is not strong enough beyond 8V and as a result a full π phase change cannot be achieved with smaller phase shifter lengths. For OOK modulation, this will have no negative consequence on the transmission performance of the modulator; however, for a multi-amplitude modulation format such as PAM-4 this requires further non-linearity compensation to achieve equidistant amplitude levels. This non-linearity is further discussed in the next sections. A resistive heater is used on one arm of each MZM to control the biasing and operating conditions. In the case of the DP-MZM, three tuners are used, one for each inner MZM to apply proper biasing of the modulators and one on the outer MZM to ensure in-phase combination of the two branches. The detailed design of the thermos-optic tuners is presented in Chapter 3.

6.2.2 Microwave Characterization

Since we fabricated the modulators in the same process as in [70], the electrode design of the modulators requires minimal update. To summarize: three main criteria need to be met in the design of the electrodes to enable the targeted BW. First, the PN junction loaded electrodes should have 50 Ω characteristic impedance, to minimize any RF back reflection. Second, microwave losses must be minimized since the main limiting factor in BW performance of the modulators are RF loss, and finally, the optical group velocity and microwave phase velocity should be closely matched. We follow the same design methodology presented in [70] to optimize the CPS travelling wave electrodes for the O-band modulators and to calculate microwave losses and velocity mismatch limitation. Since the process parameters are the same (i.e. doping density, metal trace material, metal thickness etc.), the conductor and dielectric losses remain the same. It should be noted that the effects of change in the waveguide geometry and doping dimensions on the PN junction capacitance and series resistance versus the C-band case in [70] are minimal and can be neglected. The capacitance of the PN junctions is simulated to be 230 pf/m at 0 V, and 160 pf/m at -3 V which is within 1% of the values for 500 nm wide waveguide used for 1550 nm applications. On the other hand, the group index of the optical TE mode at 1310 nm is simulated to be 3.96, while the microwave effective index of the PN junction loaded electrodes varies from 4 to 3.7 between 1 to 50 GHz. This results in a slightly higher velocity mismatch between the optical group velocity and microwave phase velocity compared to C-band TWMZM. Taking into consideration the changes mentioned above and to maintain 50 Ω characteristic impedance, we arrive at 60 μm electrode width and 35 μm spacing. However due to higher velocity mismatch and considering our required ≥ 35 GHz EO bandwidth, the electrode length must be kept ≤ 4.1 mm. Fig. 35 shows the measured EO S21 and S11 curve of all modulators at 0 V and -3V reverse bias normalized to 1.5 GHz. The difference between the segments of the ME-MZMs are mainly caused by their difference in lengths. For example, as shown in Fig. 33(d) the second segment of both ME-MZMs are slightly longer than their first segments to accommodate the optical routing to the GCs and also the thermo-optic tuners.

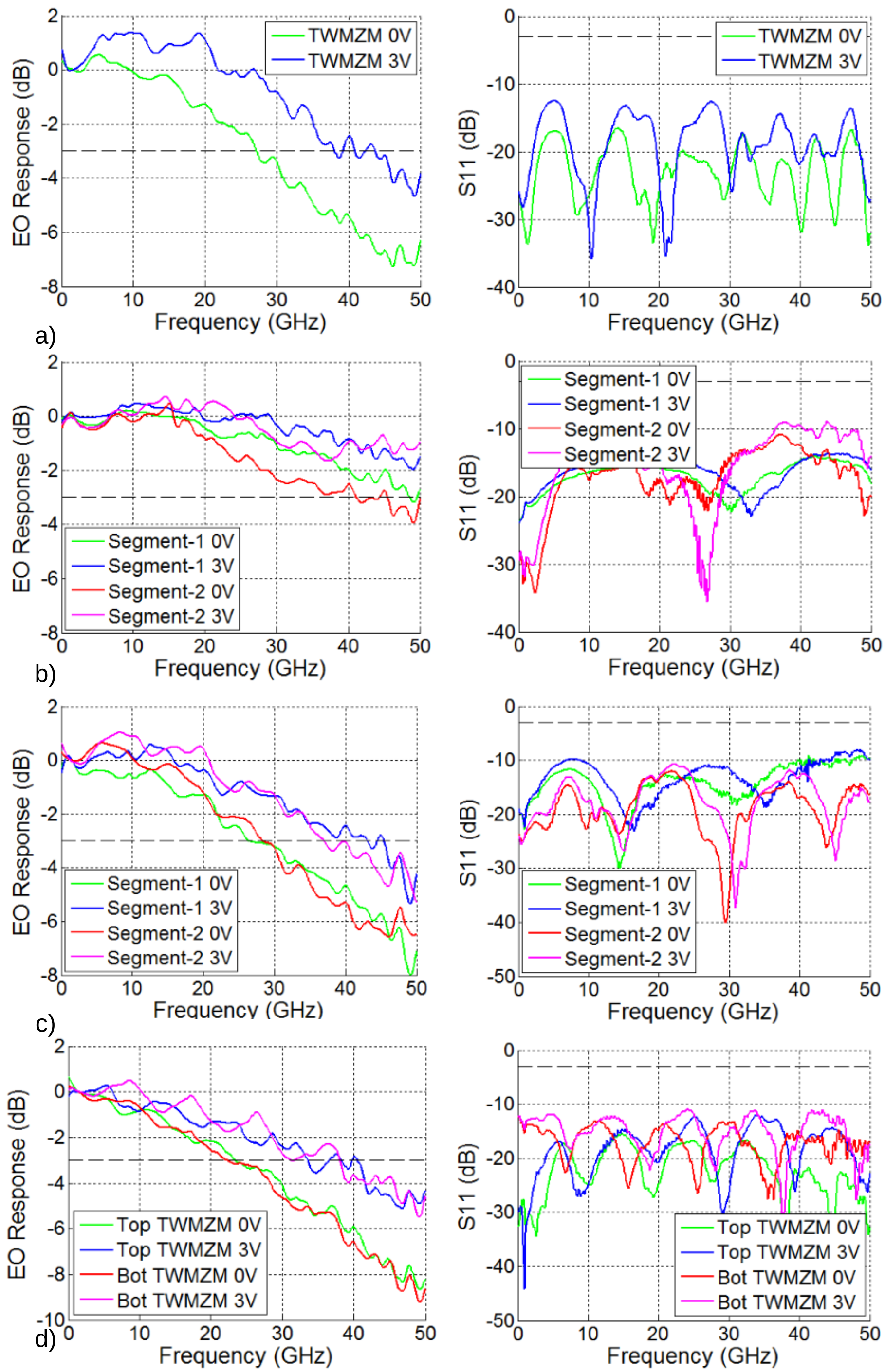

Fig. 35.EO and S11 response of a) TWMZM, b) ME-MZM with 1.5 mm long phase shifter, c) ME-MZM with 3 mm long phase shifters and, d) DP-MZM.

6.2.3 Transfer Function and Linearity

DP-MZMs and ME-MZM function as optical DACs. For PAM-N they are operated as N-bit DACs. Therefore, similar to electrical DACs, linearity is an important factor of their performance. On one hand a MZM's transfer function is a nonlinear cosine function, on the other hand SiP PN junction phase shifters are also nonlinear. This creates extra challenges for PAM-N modulation using SiP MZMs. In this section we present the measured transfer function of the SiP MZM and characterize their differential nonlinearity and integral nonlinearity. The DNL and INL were previously introduced in section 4.2. Here we introduce them in terms of output optical intensity of the modulator to better show their dependence on the transfer function of the modulator. Furthermore, we investigate the ratio of level separation mismatch (RLM) for each modulator. The DNL is defined as the ratio of an actual analog step to the ideal value of the LSB.

$$DNL = \left| \frac{I_{N+1} - I_N}{I_{LSB}} - 1 \right| \tag{8}$$

where I_N is the output intensity at level N corresponding to the digital input voltage V_N, and I_{LSB} is the ideal amplitude of the least significant bit. DNL allows us to assess the extinction ratio penalty of each of the four PAM-4 levels. DNL varies between 0 and 1, where 0 is the ideal case. INL, on the other hand is the ratio of an actual measured output intensity to the ideal output.

$$INL = \left| \frac{I_N - I_{zero}}{I_{LSB}} - N \right| \tag{9}$$

It should be noted that INL is defined for the drive voltage operation range not the entire transfer function range. RLM indicates the vertical linearity of the signal and is a measurement for mismatch between PAM-4 levels [33].

$$R_{LM} = \frac{6.S_{\min}}{V_3 - V_0} \tag{10}$$

where $S_{\min}$ is half of the swing between adjacent symbols, V_3 and V_0 correspond to the first and fourth PAM-4 levels.

$$S_{\min} = \frac{1}{2}\min\left(V_3 - V_2, V_2 - V_1, V_1 - V_0\right) \tag{11}$$

similarly, V_2 and V_1 correspond to the third and second PAM-4 levels. In an ideal scenario RLM =1, while the 100 GbE PAM-4 specifications require RLM$\geqslant$0.92. To investigate the linearity of each of the presented modulators, we first point out the difference between their transfer function. The transfer function of a conventional MZM is [112]:

$$\frac{I_o}{I_i} = \frac{1}{2}\left[1 + \cos(\theta)\right] \tag{12}$$

where θ is the phase change in radians. For OOK modulation, an MZM is usually operated at quadrature point to achieve maximum linearity for the transfer of drive voltage to optical power, when the MZM is driven to V_π. For PAM-4 however, if the MZM is driven to V_π, the 4 amplitude levels will not be equidistant, due to sine wave form of the MZM transfer function. To mitigate the non-linearity of MZM, a common practice is to limit the operation voltage of the MZM to the linear part of the transfer function. It should also be noted that reducing the operation range of a transfer function results in overall extinction ratio (**ER**) reduction of the PAM-4 levels, hence a careful study of the ER penalty is important in improving the transmission performance of the MZM.

Fig. 36, shows the transfer function of the presented SiP TWMZM using the measured phase-shift presented in Fig. 34 versus an MZM with a linear phase shifter (red curve). As shown in Fig. 35, due to the nonlinearity of the SiP phase shifters, the transfer function of the SiP TWMZM is not a perfect sine wave and therefore is not symmetric with respect to quadrature point ($I_o = 0.5 \times I_{in}$) where I_o is the optical intensity at the output of the modulator. As a result, to improve the linearity of the SiP TWMZM for PAM-4 operation, in addition to reducing the operation range (i.e. drive voltage), the bias point of the MZM should be adjusted accordingly. Since the shape of the transfer function is dependent on the PN junction, the bias point of the presented MZMs is empirically found to be at $I_o = 0.54 \times I_i$, slightly higher than the quadrature point. For example, as shown in Fig. 36 if the SiP MZM is operated at quadrature point ($I_o = 0.5 \times I_{in}$) and driven by $0.5 \times V_\pi$, the DNL and INL are 0.23 and 0.21, respectively. However, by changing the operation point to $I_o = 0.55 \times I_i$ (shown as green dashed line) the DNL and INL are reduced to 0.13 and 0.12, respectively. This significantly improves the BER performance of the system in which the SiP MZM is used. From Fig. 36, it can be observed that reducing the driving range (DR) of the modulator to $0.5 \times V\pi$ only reduces the transmission range to $0.76 \times I_{in}$ instead of I_{in}. As a result, the four intensity levels of PAM-4 are 0.96, 0.69, 0.42 and 0.2 and the RLM is 0.87, while if the modulator is driven by V_π and bias at quadrature the intensity levels are 1, 0.63, 0.05 and 0. It is clear that in this condition the two lowest intensity levels are very close, while the two middle levels are far apart. This can result in up to 1 dB ER reduction. Due to their high $V\pi$, SiP MZMs are often driven with fraction of their $V\pi$, for example in [113], [114] a 50 Gb/s OOK error free modulation is achieved by driving the modulator to 12% of the measured $V\pi$. In the next sections we experimentally evaluate the effects of reducing the driving voltage on the transmission performance of the presented modulators.

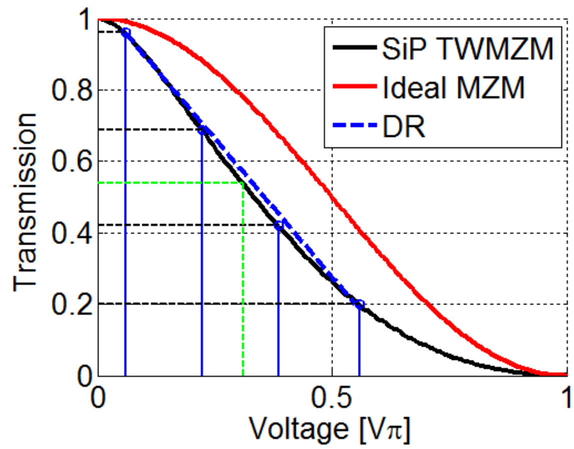

Fig. 36. Transmission spectrum of SiP TWMZM and a MZM with linear phase shifters. (DR: Dynamic Range). Dashed green line identifies the bias point at 0.55 × Ii.

As shown in Chapter 5, the transfer function of ME-MZM differs from that of single electrode MZM. A ME-MZM operates by summing the phase-shift of each segment to create the PAM levels, while a DP-MZM operates by summing the output intensity of each child MZM. The transfer function of ME-MZM ignoring losses, can be written as:

$$\frac{I_o}{I_i} = \frac{1}{2}\left[1 + \cos(\theta_1 + \theta_2)\right] \tag{13}$$

where, θ_1 and θ_2 are the phase changes from modulating each segment. Fig. 37 shows the transmission of ME-MZM as a function of the drive voltages of the two segments. The red dot indicates the biasing point of the device, and the black dots indicate the 4 intensity levels of PAM-4 adjusted such to compensate for the non-linear transfer function of the device. The four intensity levels of the longer ME-MZM are 0.94, 0.7,0.4 and 0.16 while the PAM-4 intensity levels for the shorter ME-MZM are 0.89, 0.71, 0.5 and 0.3 respectively. The RLM values of the longer and shorter ME-MZM are 0.92, and 0.915 respectively. The ME-MZM with 3 mm long segments has a more linear transmission function than the ME-MZM with 1.5 mm long phase shifters. As a result, the DNL and INL of the longer ME-MZM are 0.05 and 0.07 for the transmission range of

0.8 I_i, while the DNL and INL of the shorter ME-MZM are 0.07 and 0.09 for the transmission range of 0.6I_i.

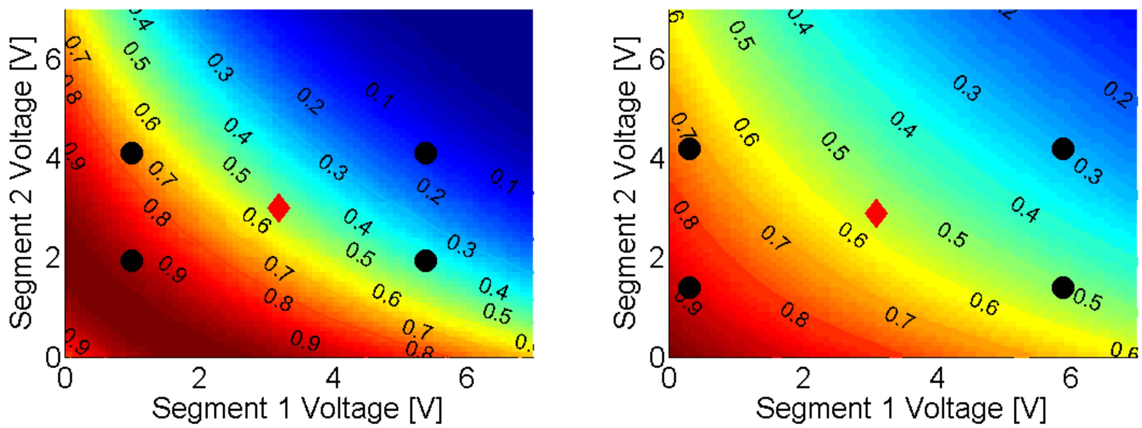

Fig. 37. a) The transmission spectrum of ME-MZM with 3 mm phase shifters, and b) transmission spectrum of ME-MZM with 1.5 mm phase shifters as function of the drive voltages of the two segments. The black circles on the graphs mark the PAM-4 levels, and the red diamond shows the bias point of the modulators.

Similarly, the transfer function of the DP-MZM when both arms of the outer MZM are in phase, can be written as:

$$\frac{I_o}{I_i} = \frac{1}{2}\left[\frac{1}{2}\left[1+\cos(\theta'_1)\right] + \frac{1}{2}\left[1+\cos(\theta'_2)\right]\right] \tag{14}$$

where θ'_1 and θ'_2 are the phase changes from the top inner MZM and bottom inner MZM, respectively. Fig. 38 shows the transfer function of DP-MZM as a function of the two drive voltages of inner MZMs. From the curvature of the graph, it can be seen that DP-MZM has a more linear transmission than the TWMZM or the shorter ME-MZM even though it has the same Vπ value. This can be explained by looking at the driving range of the inner MZMs. The inner MZMs are driven by a smaller fraction of their Vπ, compared to the ME-MZM and TWMZM; hence they are operating in a more linear regime. Also, as shown in (9), the output intensity of the DP-MZM is the sum of the output of both inner MZMs, and summation is a linear operation, hence the DP-MZM is expected to have a more linear transmission compared to a ME-MZM with the same phase shifter length. The red dot on Fig. 7 indicates the bias point of the device where the intensity is close to 0.57, slightly above the quadrature point of the device. The four black dots, indicate the four intensity levels of PAM-4, at 0.31, 0.51, 0.7 and 0.9 of I_i. The calculated DNL and INL for of the DP-MZM are 0.05, while the R_{LM} is 0.966.

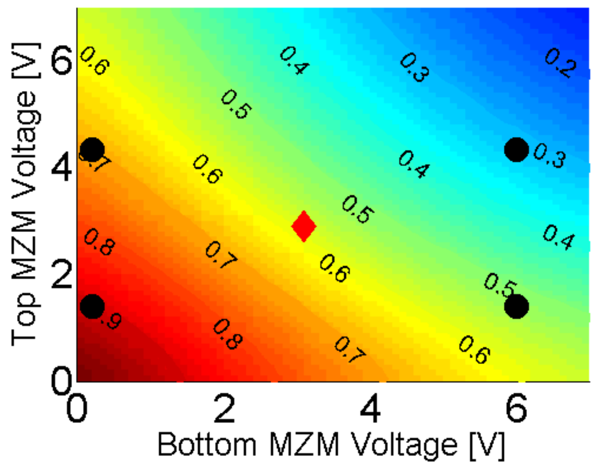

Fig. 38. Transmission spectrum of DP-MZM as a function of the drive voltage of top and bottom inner MZMs.

We use a simple figure of merit (**FOM**) BW/ V_π to evaluate the overall expected performance of the modulators compared to each other, where BW is the 3 dB electro-optic bandwidth of the modulator. Modulators with higher FOM are expected to perform better, since a large BW allows the modulator to achieve higher baudrate while lower V_π indicates more efficient phase shifter. From the analysis and characterization of the modulators in this section, the calculated FOM for the TWMZM, DP-MZM, shorter ME-MZM and longer ME-MZM are 3, 2.9, 3.7 and 5.4 GHz/V, respectively. The improved FOM of the ME-MZMs are the result of their segmented electrode design. Using multiple electrodes, results in shorter segment lengths and ultimately lower microwave losses, allowing the ME-MZM to have higher BW for longer phase shifter lengths. The shorter ME-MZM has the same total phase shifter length as the TWMZM and the DP-MZM, while its electrodes are shorter, resulting in same V_π as the TWMZM and DP-MZM but significantly higher BW. On the other hand, the longer ME-MZM has similar electrode length as the TWMZM and ME-MZM but with twice the phase shifter length, resulting in similar BW but lower V_π.

6.3 Transmission Experiment

In this section we investigate the transmission performance of each device for OOK and PAM-4 modulation. First, we present the transmission performance of the modulators without using DSP. For OOK modulation we use a bit pattern generator (**BPG**) to drive the modulators and a bit error rate tester (**BERT**) for BER measurements. For PAM-4, we use a 63 GHz real-time oscilloscope (**RTO**) to capture the received data, since the BERT is not capable of PAM-4 error measurements. Next, we repeat the experiment by replacing the BPG with an 8-bit electrical DAC operating at 88 GSample/s and apply DSP to the modulator's drive signal. Fig. 39 illustrates the experimental setup for each modulator.

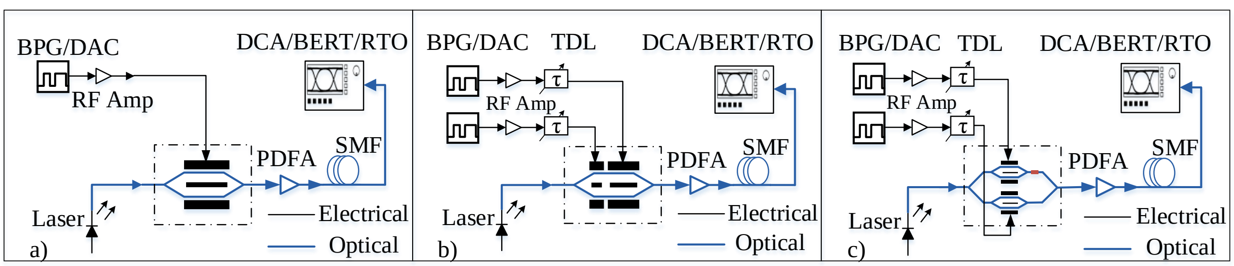

Fig. 39.The experimental setup of (a) TWMZM, (b) ME-MZM, and (c) DP-MZM.

6.3.1 Transmission Without DSP

As shown in Fig. 39 the electrical driving signal is generated using a BPG, and is then amplified using a 45 GHz RF amplifier. In the case of TWMZM the amplified signal is directly applied to the modulator using a 50 GHz RF probe. For the DP-MZM and ME-MZM, the delay and skew settings of the BPG along with RF TDLs are used to time align the two BPG channels before applying them to the modulators through the RF probes. All four modulators are biased at -3 V. For ME-MZM, the time delay for the drive signal of the second segment can be estimated by dividing the sum of the length of the first segment and the separation between the two segments by the optical group velocity. For DP-MZM, both drive signal path lengths should be the same, and this is achieved by using matched RF cables, and matched RF amplifiers. The TDLs are then used to fine tune the two signal streams. A 13 dBm tunable O-band laser is used as a source for the modulators. The modulated signal is then amplified to 5 dBm using a praseodymium-doped fiber amplifier (**PDFA**) and propagated through various lengths of fiber. The PDFA is used to compensate for the high insertion loss of the grating couplers, and routing losses. In addition, using a transimpedance amplifier (**TIA**) with the photodetector (**PD**) can significantly improve receiver sensitivity and reduce the optical power needed at the PD. Fig. 40 demonstrates the 40 Gbaud OOK optical eye diagrams of the modulators driven by 3 V_{pp} drive signals. The presented eyes are captured using the 80 GHz optical sampling head of the digital sampling oscilloscope (**DSO**). From Fig. 40 it can be seen that both ME-MZM modulators achieve higher extinction compared to TWMZM and DP-MZM. This can be attributed to the lower microwave loss of the shorter ME-MZM and the longer phase-shifter length (lower $V\pi$) in the case of longer ME-MZM. It should however be noted that the ME-MZMs and DP-MZMs are operated with two drive signals which increases complexity versus TWMZM.

For OOK modulation, two identical PRBS signals with the same V_{pp} are applied to both ME-MZM segments and in the case of DP-MZM's, to the two child MZMs. A 50 GHz, 0.65 A/W photodetector is connected to the BERT to receive the signal and measure the BER. Fig. 41 illustrates the BER measurement of each modulator for various baud rates and drive signal voltages in the back-to-back (B2B) and over 10 km of standard single mode fiber (SMF). The dotted horizontal red and black lines indicate the KP4-FEC threshold at 2.4×10^{-4} and HD-FEC threshold at 3.8×10^{-3}.

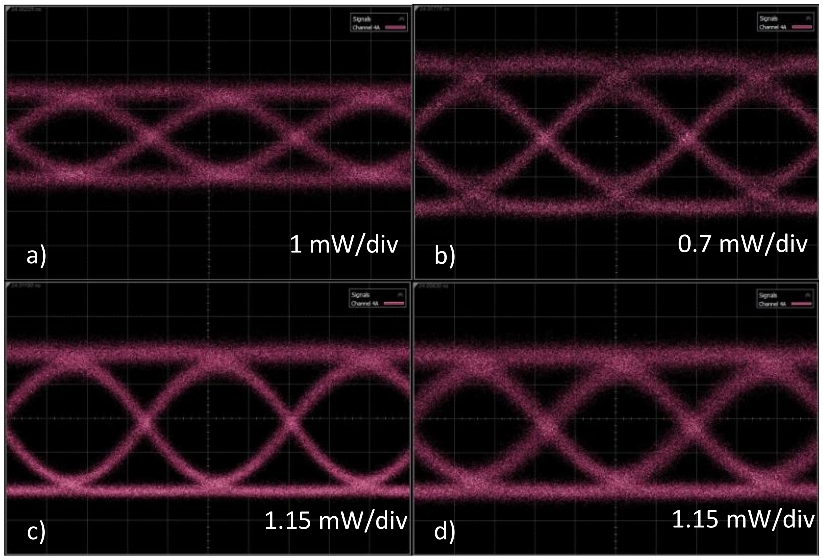

Fig. 40. 40 Gbaud OOK eye diagram of a) TWMZM, b) DP-MZM, c) ME-MZM with 1.5 mm segments, and d) ME-MZM with 3 mm segments.

As expected from the BW/ Vπ values presented in previous section, the ME-MZMs perform noticeably better compared to the TWMZM, and DP-MZM. It should also be noted that in the case of the shorter ME-MZM, the system is not bandwidth limited, however due to the high Vπ values, the improvement in performance is not significant compared to the longer ME-MZM. DP-MZM's inferior performance can be attributed to two factors, first the slightly lower FOM value of the device compared to the other three modulators, and second, the drift of the biasing heaters.

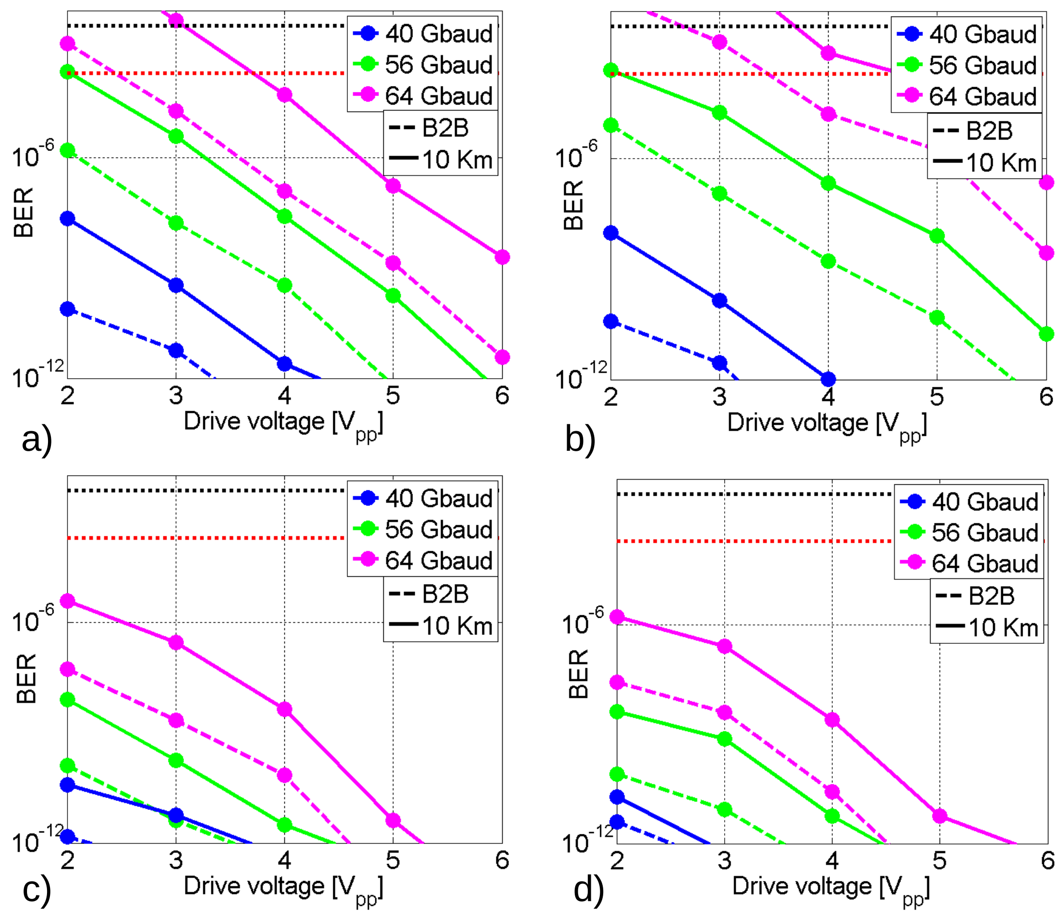

Fig. 41. BER measurements of a) TWMZM, b) DP-MZM, c) ME-MZM with 1.5 mm segments and d) ME-MZM with 3 mm segments.

To achieve PAM-4 modulation using DP-MZM and ME-MZM two independent OOK PRBS signals are applied to the modulators as shown in Fig. 39(b-c). Since the BERT is not capable of PAM-4 error counting, we perform the error counting offline, by capturing the received signal using the RTO. Additionally, as our BPG can only transmit OOK signals the TWMZM can't be used to achieve PAM-4 without the use of DSP. Figure 42 shows the 40 Gbaud PAM-4 eye diagrams of modulators captured using the DSO. The presented eyes are captured using the drive conditions presented in Figs. 37 and 38. For the longer ME-MZM the modulator is biased at 3.2 V and the two drive voltages are 4.4 V and 2.1 V. For shorter ME-MZM the bias voltage is set at 3.0

V and the drive voltages are 5.7 V and 2.7 V. Similarly, for the DP-MZM, the bias voltages of both inner MZMs are set at 3.0 V and the drive voltages are 5.8 V and 3 V.

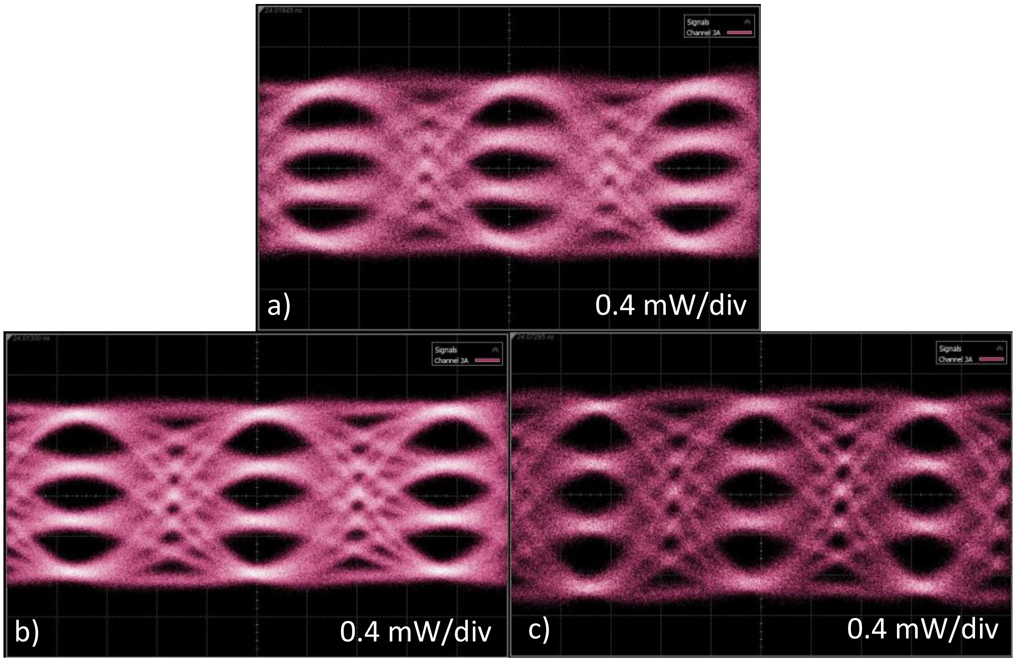

Fig. 42. 40 Gbaud PAM-4 eye diagrams of a) DP-MZM, b) shorter ME-MZM, and c) longer ME-MZM.

The longer ME-MZM achieves a higher extinction ratio compared to the other two modulators while driven by lower amplitude drive signals, thanks to its longer phase shifter length. Fig. 43 shows the BER performance of each modulator for various baudrates and drive voltages in the back-to-back (**B2B**) and 10 km transmission. All three modulators are capable of generating 56 Gbaud PAM-4 signals without the use of DSP. However, from Fig. 43 several important observations can be made. The shorter ME-MZM achieves below FEC transmission up to 64 Gbaud. This superior performance can be attributed to the higher BW of this modulator. On the other hand, the BER performance of the shorter ME-MZM is more sensitive to drive voltages compared to the longer ME-MZM. From Fig. 43(b) it can be observed that lowering the drive voltage affects the BER performance of shorter ME-MZM more severely than the longer ME-MZM. This is due to the larger V_π value of the shorter ME-MZM. On the other hand, maximizing the drive voltage (7 V_{pp} and 3.3 V_{pp}), negatively impacts the BER performance at 56 Gbaud and 64 Gbaud. This can be explained by referring to the linearity discussion in the previous section and in Fig. 37(a). By increasing the drive voltages, the modulator suffers more from the non-linearity of its transfer function, resulting in PAM-4 amplitude levels that are not equidistant which in turn results in higher error counts. Using both of the ME-MZMs, we achieve 10 km transmission at 56 Gbaud below HD FEC threshold, which is highest baud rate achieved using an O-band SiP modulator.

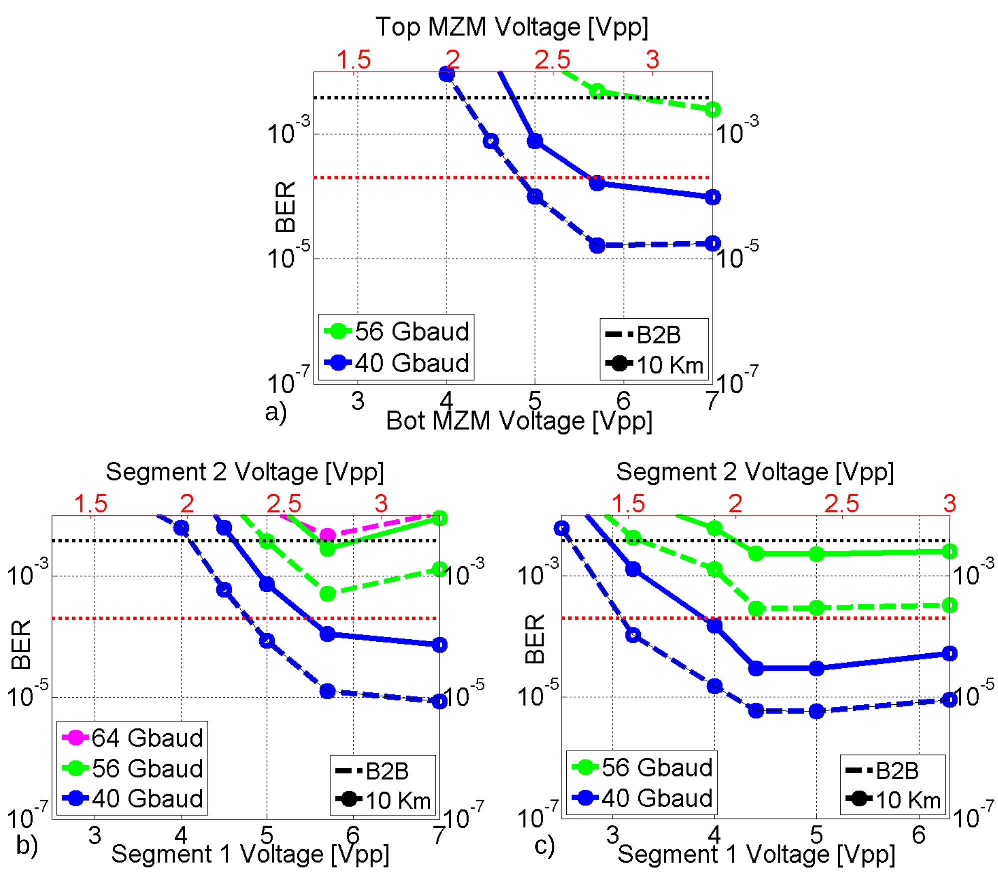

Fig. 43. PAM-4 BER performance of a) DP-MZM, b) shorter ME-MZM and c) longer ME-MZM. The dotted horizontal red and black lines indicate the KP4 FEC threshold at 2.4×10^{-4} and HD FEC threshold at 3.8×10^{-3} respectively.

The longer ME-MZM can achieve below FEC transmission while driven by lower drive voltages, compared to the other two modulators due to its longer phase shifter length. Like the other two modulators at higher drive voltages, the BER performance deteriorates slightly because of nonlinearity.

6.3.2 Transmission With DSP

DSP is widely used in long haul communication systems, while for short reach communication the use of DSP is still a topic of debate. However, in recent years and because of the growing bandwidth demand and adaptation of PAM-4 for 400 Gb/s systems, DSP is viewed as a necessary enabler of higher modulation formats, and higher baudrates. In this section we investigate the improvements achieved using DSP.

To quantitatively assess the improvements achieved by applying DSP, we replace the BPG with an 8-bit, 88 GSample/s electrical DAC, while the rest of the experimental setup remains the same. We use the same transmitter DSP presented in chapter 5 and in [111] which includes raised cosine pulse shaping, RF pre-emphasis up to the output of the RF amplifiers, and quantization. For the case of PAM-4 modulation using TWMZM, the PAM-4 signal is generated in the electrical domain using the DAC. PAM-4 amplitude levels are adjusted using the DAC to compensate for the TWMZMs non-linearity. For the DP-MZM and ME-MZM cases the modulators are driven by OOK signals. On the receiver side, we use the RTO to capture the modulated signal and perform offline signal processing which consists of: sampling the received signal at 160 GSample/s, matched filtering, clock recovery, receiver equalization and symbol decision. Fig. 44 demonstrates the BER performance of the modulators for various drive voltages and symbol rates.

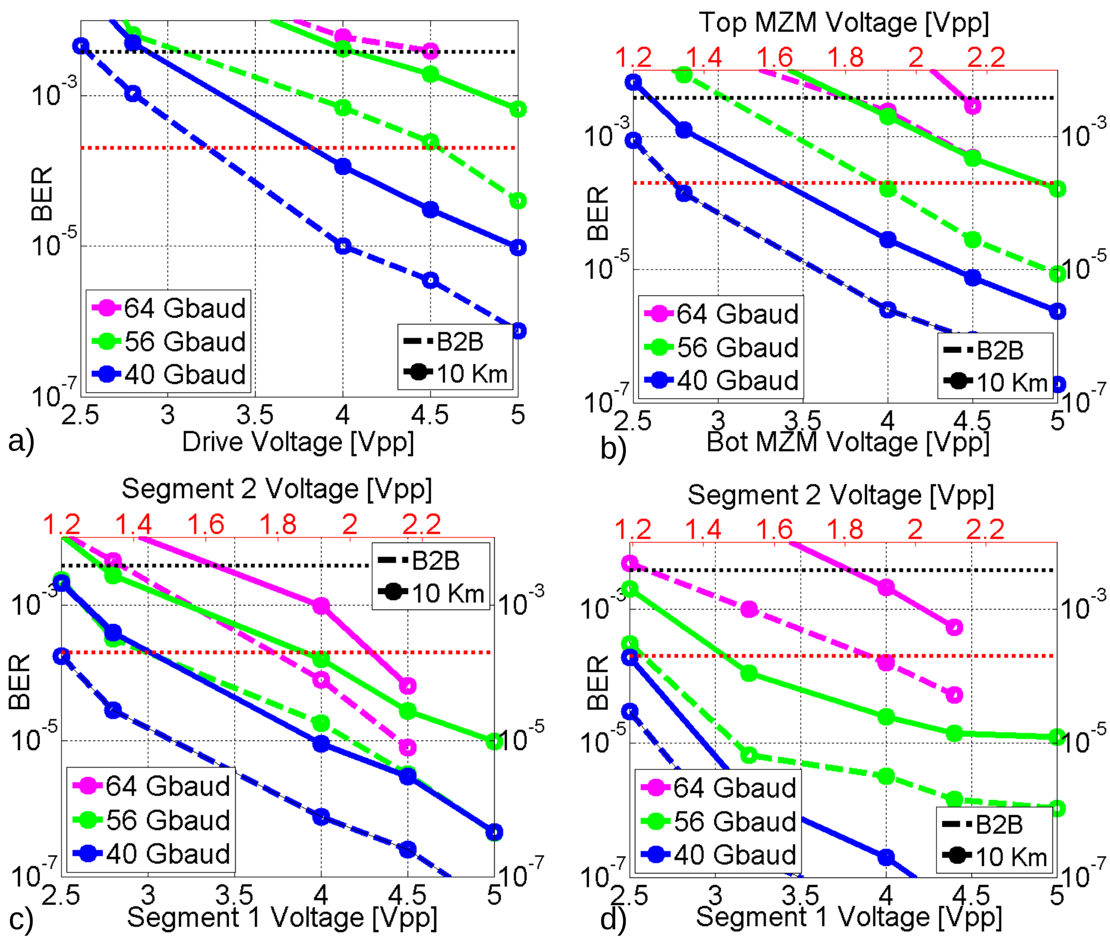

Fig. 44. PAM-4 BER performance of the a) TWMZM, b) DP-MZM, c) shorter ME-MZM, and d) longer ME-MZM. The dashed horizontal redlines indicate the KP4 FEC threshold at 2.4×10^{-4} and HD-FEC threshold at 3.8×10^{-3} respectively.

From Fig. 44 it is clear that DSP significantly improves the BER performance of the system. More specifically at higher symbol rate the effect of equalization is more noticeable, where significant improvements can be observed at 64 Gbaud. It should be noted that due to stronger equalization at 64 Gbaud the maximum achievable peak-to-peak voltage is 4.5 V_{pp}. Both ME-MZMs can be used for 64 Gbaud PAM-4 generation below the KP-4 FEC. Since we are operating close to 1310 nm, the effects of dispersion are minimal, and we are limited mostly by the optical fiber losses. In addition, it is observed that DP-MZM and ME-MZMs provide a substantial improvement over TWMZM. As mentioned previously the TWMZM requires an electrical PAM-

4 signal, however the DP-MZM and ME-MZMs are operated using OOK electrical signals. The superior SNR and ER of the OOK electrical signal has a clear effect on the performance of these devices.

Use of DSP in a commercial TOSA/ROSA results in considerable increase in power consumption. Similarly requiring two drive voltages to operate DP-MZM and ME-MZMs increases the power consumption. To impartially assess the overall performance of each modulator a thorough analysis of modulator and drive circuitry power consumption is required. However, calculating the DAC or the BPG's power consumption is not possible. Hence, we estimate the energy consumed only by the modulator. The energy consumed by each modulator can be estimated by $P = \sum_{i=1}^{N} \frac{V_{i,RMS}^2}{R}$, where, N is the number of drive signal and $V_{i,\mathrm{rms}}$ is the root-mean-square of the ith drive voltage [80] as presented in chapter 5. Table III shows the minimum energy consumption of each modulator to achieve sub HD FEC transmission at various symbol rates. Use of DSP lowers the BER of the modulators as expected, however this effect is more noticeable in the DP-MZM and longer ME-MZM where the modulators are BW limited for high symbol rates. At 56 Gbaud, which is the target symbol rate per lambda for 400 Gb/s systems, the longer ME-MZM is clearly the optimized design, where without the use of DSP, the modulator achieves the lowest power consumption. However, DSP enables the modulator to achieve transmission below KP-4 FEC at 56 Gbaud.

Table III. Minimum energy consumption of each modulator for below HD FEC PAM-4. The Vi,rms values are calculated from the drive voltages shown in Figs. 43 and 44.

PAM-4 Baud [Gbaud]	TWMZM		DP-MZM		ME-MZM (1.5 mm segments)		ME-MZM (3 mm segments)	
	V_{rms} [V]	Power (pJ/bit)	V_{rms1}, V_{rms2} [V]	Power (pJ/bit)	V_{rms1}, V_{rms2} [V]	Power (pJ/bit)	V_{rms1}, V_{rms2} [V]	Power (pJ/bit)
40, Without DSP	NA	NA	1.4, 0.7	0.63	1.6, 0.7	0.78	1.1, 0.5	0.39
40, With DSP	1.0	0.25	0.9, 0.4	0.24	0.9, 0.4	0.24	0.9, 0.4	0.24
56, Without DSP	NA	NA	2.5, 1.2	1.13	2.0, 1.0	0.89	1.4, 0.7	0.44
56, With DSP	1.4	0.36	1.4, 0.7	0.44	1, 0.5	0.21	0.9, 0.4	0.17
64, Without DSP	NA	NA	NA	NA	NA	NA	NA	NA
64, With DSP	NA	NA	1.6, 0.8	0.49	1.4, 0.7	0.38	1.1, 0.3	0.25

6.4 Conclusions

In this chapter, we investigated the performance of different Mach-Zehnder interferometer-based O-band modulators presented in previous chapters for 400 Gb/s short reach transmission system employing PAM-4 modulation. We update the design of modulators in-order to be able to perform impartial and detailed comparison. We present modulators designs and study their transfer function and linearity in detail. We present ideal biasing points and driving conditions for each modulator based on their phase shifter length and transfer function. We use the FOM BW/Vπ, to assess the overall performance of the modulators. Next, we study their transmission performance, and present each modulator's power consumption. Moreover, we explore the advantage of using DSP and its effect on power consumption. We present an optimized design in the form of 2 segments ME-MZM with 3 mm long phase shifters and experimentally show that this modulator provides a clear improvement in transmission system performance compared to the other presented modulators. Additionally, we show that generating PAM-4 signal in optical domain using modified MZM structures such as ME-MZM and DP-MZM result in better transmission performance compared to using traditional single electrode TWMZM.

Chapter 7

Conclusion

7.1 Overview

The rapid increase in datacenter traffic fueled by cloud computing and multimedia applications has created a demand for high speed, power efficient, and compact transceivers for datacenter optical interconnects. The currently deployed 100 Gb/s transceivers operate using 4 ×25 Gb/s configuration and on-off keying modulation format. The next generation Ethernet optical transceivers will operate at 400 Gb/s in the form of 4 × 100 Gb/s. To cope with this substantial increase in single lane bitrate the recently released 400 Gb/s IEEE Ethernet standard has introduced several changes [3]. Pulse amplitude modulation with four levels (PAM-4) has been selected as the modulation format of choice for 400 Gb/s systems. Additionally, the use of a stronger FEC code has been included in the standard. PAM-4 provides up to double the spectral efficiency of OOK, and hence requires a less extreme increase in transceiver component's bandwidth. On the other hand, with the conclusion of 400 Gb/s IEEE Ethernet standard, the discussion about next generation 1 Tb/s systems is heating up. Similar to changes from 100 Gb/s to 400 Gb/s standard it is widely accepted that 1 Tb/s would bring forth significant updates to modulation format, power consumption and transceiver configuration.

The move from OOK in 100 Gb/s standard to PAM-4 in 400 Gb/s standard is a significant update and the first time that the modulation format for the short reach communication systems has changed. As a result, it is necessary to examine how individual components of a transceiver will be affected by this change. Modulators are the most important component in the transmitter side. They are also the component that is directly affected by the change in bitrate and modulation format. As a result, it is vital that a comprehensive study of modulator design be performed for 400 Gb/s systems.

In parallel, silicon photonics has recently become a popular choice for datacenter interconnects. Taking advantage of years of complementary metal oxide semiconductor research and development, SiP provides a low cost, high yield platform for datacenter optical interconnects [115]. Because of the high index contrast between Si and SiO_2, SiP optical components enjoy a relatively smaller footprint, this results in easier integration of photonic integrated circuits (**PICs**) which is desirable to fit in small pluggable transceiver modules such as the QSFP modules used in datacenter interconnects. Furthermore, taking advantage of germanium epitaxy on Si, high responsivity and high bandwidth silicon-germanium photodetectors capable of single wavelength 100 Gb/s PAM-4 transmission and detection have been recently reported [37-42]. By employing these components, SiP integrated coherent receivers and direct detection systems have been demonstrated [43-45].

Traditionally, TWMZM have been a popular choice for TOSAs. TWMZMs offer temperature stability and have very wide optical bandwidth and as a result are excellent options for WDM systems. TWMZMs in LiNbO3 and SiP have been used for PAM-4 and IQ modulation in several recent studies [44], [116-118]. In majority of these cases the PAM-4 signal is generated in electrical domain using a digital to analog convertor and applied to the modulator for EO conversion. In this thesis, we present various Mach-Zehnder modulator-based structures for on-chip optical generation of PAM-4. We further report the highest PAM-4 bitrate generation to date using a ME-MZM structure. Furthermore, we investigate the use of coherent modulation formats for short reach applications using a SiP IQM. We achieve the highest bitrate and drive voltage combination for a SiP modulator, which could suggest with further optimization, SiP IQMs at O-band could provide a power efficient alternative for 1 Tb/s applications.

7.2 Summary of Original Contributions

The rise of silicon photonics as a potential fabless eco-system for optical interconnects has opened the door for a plethora of innovative designs in both active and passive devices. We demonstrate in this thesis that the modulator structure plays a paramount role in the performance and efficiency of the optical transceiver and that it is vital to explore different modulator designs for different modulation formats and applications. Hereafter, we summarize the original contributions achieved in this thesis based on the three modulator structures presented.

7.2.1 Series Push-Pull Travelling Wave Modulator for O-band operation

In chapter 2 we present a SPP-TWMZM that is used as a building block of the other modulator architectures presented in this thesis. An O-band variation of the devices is also presented in chapter 6. The single drive, push-pull operation of the SPP-TWMZM provides several key advantages for developing the DP-MZM and ME-MZM for generation of PAM-4 and high order modulation formats. First, due to the series connection of the PN junctions the total capacitance of the PN junctions are nearly halved in SPP configuration. This significantly lowers the microwave losses of the travelling wave electrodes, and hence a SPP-TWMZM can achieve a higher BW compared to a DD-TWMZM with comparable Vπ. Second, the single drive operation of the device, allows for easier integration of the modulator in PICs. As a result, ME-MZM and DP-MZMs using SPP configuration only require two binary drive signals for PAM-4 generation, while a DD configuration of these devices would require four binary drive signals. This effectively lowers the complexity of the PIC. And finally, the push-pull operation of SPP results in very low chirp and hence negligible phase modulation at the output of the modulator, which enables the DP-MZM operation for PAM-4 generation. Taking advantage of this device we present two modulator structures that can be used for high order modulation.

7.2.2 Dual Parallel Mach-Zehnder Modulator

DP-MZMs have been used for IQ modulation. In this thesis we utilize DP-MZMs for short reach communication. In chapter 3, we present the detailed design of a DP-MZM operating at O-band based on the SPP-TWMZM designs presented in chapter 2. We present the DC and small signal characterization of the device. Furthermore, we discuss the effects of non-linear operation of SiP phase shifters on the modulator operation and discuss possible solutions to mitigate these effects. We further present a low loss, resistive thermo-optic tuner which is used for biasing the modulator. We report below HD-FEC, 180 Gb/s 16QAM and 154 Gb/s QPSK transmission over 20 km of SMF-28. Furthermore, we demonstrate that 144 Gb/s QPSK transmission can be achieved with a low drive voltage of 3 Vpp.

Next, we explore the DP-MZM for PAM-4 operation. For the first time, we demonstrate on chip generation of PAM-4, using DP-MZM driven by two binary drive signals. We discuss the biasing method for PAM-4 operation of the device in detail and discuss the differential and integral non-linearity of the device. We present solutions for lowering the non-linearity of the device and achieving equidistant PAM-4 levels. In a transmission experiment, we report below HD-FEC generation and transmission of 100 Gb/s PAM-4. This showcases the potential of utilizing DP-MZMs for short reach optical interconnects.

7.2.3 Multi-Electrode Mach-Zehnder Modulator

Next, we present a ME-MZM based on the SPP-TWMZM design. ME-MZM operates by combining the phase shifter of each electrode segment to create multi-amplitude modulation formats. As such the design of this device can further be expanded for higher order PAM. For example, by increasing the number of electrode segments to three, the modulator can be used to generate PAM-8. In this thesis we focus on a two electrode ME-MZM for PAM-4 modulation. However, by increasing the number of electrode segments to three, the modulator can be used to generate PAM-8. We present the operation of the device in detail and characterize the linearity and performance of the modulator for PAM-4 generation. We achieve one of the highest PAM-4 bitrate transmission reported on any platform, and experimentally show that optical generation of high order modulation formats can provide clear advantages for short reach interconnects.

Finally, we investigate the performance of all three types of modulators presented in this thesis at O-band. First, we update the electrode and phase shifter lengths of the modulators, such they have the minimum BW requirements for 100 Gb/s single wavelength operation. We present four modulators as follows: a) TWMZM with 3mm long phase shifter, b) a DP-MZM with 3 mm long inner TWMZMs, c) a ME-MZM with two, 1.5 mm long phase shifters and finally d) ME-MZM with two 3 mm long phase shifters. The four modulator designs allow us to preform an impartial study of the transmission performance and power consumption of these devices. We present ideal biasing points and driving conditions for each modulator based on their phase shifter length and transfer function. We discuss the linearity of each modulator based on their transfer function and phase shifter lengths. A simple figure of merit, in the form of BW/V_π, is used to assess the overall performance of the modulators. We perform detailed power consumption study of all the modulators and present an optimized design in the form of 2 segments ME-MZM with 3 mm long phase shifters and experimentally show that this modulator provides a clear improvement in transmission system performance compared to the other presented modulators. Additionally, we show that generating PAM-4 signal in optical domain using modified MZM structures such as ME-MZM and DP-MZM result in better transmission performance compared to using the traditional single electrode TWMZM.

7.3 Future Work

In this dissertation, we explored different solutions for the next generation short reach interconnects and presented an alternative approach for generating high order modulation formats in optical domain. This work, focused on the transmitter side of the transmission system, however there are immense research opportunities for future work on co-integration of electronic and photonic circuits and receiver design. Silicon photonics public foundries have expedited the growth of this technology platform, by providing their services to researches from all over the world. And several major companies such as Intel, HP and IBM have dedicated resources for developing SiP based transceivers for next generation communication systems. This has popularized the field of silicon photonics and has resulted in collaborative work between photonic and electronic designers. We list below some of the prospective research avenues derived from each of the studies presented in this thesis.

Co-integration of Electronic and Photonic Circuits

Any successful solution for future optical networks requires co-integration of electronic driving circuitry and photonic integrated circuits. The presented SiP modulators in this thesis require modified driving circuitry. More importantly any successful transceiver design requires power efficient, and high bandwidth drivers. Hence, the next logical step is to look at the design of modulators and drivers as one task. The study in this thesis provides a detail study of an optimized modulator design for 400 Gb/s and PAM-4 modulation. The next step will be to further expand this study by considering the limitation of the drivers and optimizing the transceiver performance.

Germanium Epitaxy on Silicon

One of the advantages of the SiP platform is the germanium epitaxy which has been overlooked so far. Germanium on SiP can open the door for various innovative designs and ground-breaking research. Germanium has excellent absorption properties at telecom wavelengths. As a result, SiGe PDs have been demonstrated with close to 100% quantum efficiency and very high bandwidth. Furthermore, SiGe EAMs have recently been demonstrated in L-band with ultra-low driving voltages and +30 GHz BW. Similar to MZMs there are possible design modifications that can be applied to SiGe PDs and EAMs for specific applications, to further optimize their performance.

Many different SiP PD designs have been explored in recent years. Each optimizing a certain aspect of the PD performance such as minimizing dark current, optimizing responsivity, maximizing BW, etc. However, a clear optimization for short reach application have yet to be done. Moreover, another avenue of study is to explore the feasibility of using avalanche photodetectors (APD) for short reach interconnects. Silicon photonics provides a unique platform for exploring APD designs. An important metric in evaluating APDs is the excess noise factor (**ENF**). ENF is a measure of the variation in the gain of a photomultiplier and strongly depends on the k-factor, which represents the ratio of impact ionization of electrons to holes. Silicon inherently has one of the lowest k-factors among semiconductor materials and as a result the ENF of Si-based APDs is excellent [119]. By exploiting this, the superior sensitivity of SiGe APDs can be used to improve the power efficiency of the system significantly. However, this sensitivity comes at a cost of lower BW and like any other engineering problem the trade-off requires detail study.

Silicon Photonics for Quantum Information Processing

It is universally agreed upon that the next frontier in the field of information technology will be the development of quantum computers that enable computational power forever inaccessible to transistor-based computers. While universal quantum computing remains an ambitious and long-term objective, quantum-enhanced communication is a short-term spin-off technology that will result from this quest. SiP has recently been used for quantum computing and communication applications [120-123]. This opens the door for new and innovative area of research for SiP scholars. This is important because, SiP provides, easy access, mass production platform for quantum integrate circuits.

References

[1] Cisco Corp., Cisco Global Cloud Index: Forecast and Methodology, 2015-2020, http://www.cisco.com, 2016.

[2] "Cisco Global Cloud Index: Forecast and Methodology, 2016-2021," White Paper-c11-738085, 2016.

[3] IEEE P802.3bs 400 GbE Task Force, http://www.ieee802.org/3/bs/index.html

[4] K. Zhong, X. Zhou, T. Gui, L. Tao, Y. Gao, W. Chen, J. Man, L. Zeng, A. Lau and C. Lu, "Experimental study of PAM-4, CAP-16, and DMT for 100 Gb/s Short Reach Optical Transmission Systems", Optics Express, vol. 23, no. 2, pp. 1176-1189, 2015.

[5] W. Yan, L. Li, B. Liu, H. Chen, Z. Tao, T. Tanaka, T. Takahara, J. Rasmussen, and D. Tomislav, "80 km IM-DD Transmission for 100 Gb/s per Lane Enabled by DMT and Nonlinearity Management," in Optical Fiber Communication Conference, p. M2I.4, Optical Society of America, 2014.

[6] P. Dong, X. Liu, S. Chandrasekhar, L. L. Buhl, R. Aroca and Y. K. Chen, "Monolithic Silicon Photonic Integrated Circuits for Compact 100 Gb/s Coherent Optical Receivers and Transmitters," IEEE Journal of Selected Topics in Quantum Electronics, vol. 20, no. 4, pp. 150-157, July-Aug. 2014.

[7] J. Lin, H. Sepehrian, L. A. Rusch and W. Shi, "CMOS-Compatible Silicon Photonic IQ Modulator for 84 Gbaud 16QAM and 70 Gbaud 32QAM," in Optical Fiber Communications Conference and Exposition (OFC), San Diego, CA, USA, 2018.

[8] L. Chen, C. Doerr, R. Aroca, S. Y. Park, J. C. Geyer, T. Nielsen, C. Rasmussen, and B. Mikkelsen, "Silicon Photonics for 100G-and-beyond Coherent Transmissions," in Optical Fiber Communication Conference, Anaheim, CA, USA, 2016, pp. Th1B.1.

[9] *"IEEE Standard for Ethernet,"* IEEE Std 802.3, Amendment 10, 2017.

[10] E. El-Fiky, M. Osman, M. Sowailem, A. Samani, D. Patel, R. Li, M. Saber, Y. Wang, N. Abadia, Y. D'Mello and D. Plant, "200 Gb/s transmission using a dual-polarization O-Band silicon photonic intensity modulator for Stokes vector direct detection applications," Optics Express 25, 30336 (2017).

[11] P. Dong, X. Chen, K. Kim, S. Chandrasekhar, Y. Chen and J. Sinsky, "128-Gb/s 100-km transmission with direct detection using silicon photonic Stokes vector receiver and I/Q modulator," Optics Express 24, 14208 (2016).

[12] S. Ghosh, T. Takuo, Y. Kawabata, K. Katoh, K. Kikuchi, and Y. Nakamo, "Simple direct-detectio-based Stokes vector receiver circuit on InP," in Optical Fiber Communication Conference, p. Th1A.6, OSA, 2017.

[13] M. Chagnon, M. Osman, D. Patel, V. Veerasubramanian, A. Samani, and D. Plant, "Digital signal processing for dual-polarization intensity and inter polarization phase modulation formats using stokes detection," IEEE Journal of Lightwave Technology, vol. 34, no. 1, pp. 188-195, 2016

[14] T. Hoang, M. Sowailem, M. Osman, C. Paquet, S. Paquet, I. Woods, Q. Zhuge, and D. Plant, "280-gb/s 320-km transmission of polarization-division multiplexed 138 qam-pam with stokes vector receiver," in Optical Fiber Communications Conference, p. W3B.4, Optical Society of America, 2017.

[15] T. Hoang, M. Sowailem, Q. Zhuge, Z. Xing, M. Osman, E. Elfiky, S. Fan, M. Xiang, and D. Plant, “Single wavelength 480 Gb/s direct detection over 80km SSMF enabled by Stokes Vector Kramers Kronig transceiver,” Optics Express, vol. 25, no. 6, pp. 33534-33542, 2017.

[16] D. Che and W. Shieh, “Polarization demultiplexing for Stokes vector direct detection,” IEEE Journal of Lightwave Technology, vol. 34, no. 2, pp. 754{760, 2016.

[17] M. Morsy-Osman, Q. Zhuge, L. R. Chen, and D. V. Plant, "Joint mitigation of laser phase noise and fiber nonlinearity for polarization-multiplexed QPSK and 16-QAM coherent transmission systems," Optics Express 19, B329-B336 (2011).

[18] M. H. Morsy-Osman, M. Chagnon, Q. Zhuge, X. Xu, M. Mousa-Pasandi, Z. A. El-Sahn, and D. V. Plant, "Training symbol based channel estimation for ultrafast polarization demultiplexing in coherent single-carrier transmission systems with M-QAM constellations," in proceedings of European Conference on Optical Communication (ECOC), Paper Mo.1.A.4, 2012.

[19] T. Okoshi, "Recent advances in coherent optical fiber communication systems," Journal of Lightwave Technology **5**, 44-52 (1987).

[20] T. Okoshi, *Coherent optical fiber communications* (Springer Science & Business Media, 1988).

[21] A. Gnauck, P. Winzer, S. Chandrasekhar, X. Liu, B. Zhu, and D. Peckham, "Spectrally efficient long-haul WDM transmission using 224-Gb/s polarization-multiplexed 16-QAM," Journal of Lightwave Technology **29**, 373-377 (2011).

[22] D. A. B. Miller, “Device requirements for optical interconnects to CMOS silicon chips,” in *Photonics in Switching* (Optical Society of America, 2010), paper PMB3.

[23] J. E. Bowers and A. Y. Liu, “A comparison of four approaches to photonic integration,” in Optical Fiber Communication Conference (Optical Society of America, 2017), paper M2B.4.

[24] J. E. Bowers, J. T. Bovington, A. Y. Liu, and A. C. Gossard, “A path to 300 mm hybrid silicon photonic integrated circuits,” in Optical Fiber Communication Conference (Optical Society of America, 2014), paper Th1C.1.

[25] M. Hochberg, N. C. Harris, R. Ding, Y. Zhang, A. Novack, Z. Xuan, and T. Baehr-Jones, “Silicon photonics: the next fabless semiconductor industry,” IEEE Solid State Circuits Mag. 5(1), 44-58 (2013).

[26] W. Bogaerts, M. Fiers and P. Dumon, 'Design Challenges in Silicon Photonics', IEEE Journal of Selected Topics in Quantum Electronics, vol. 20, no. 4, pp. 1-8, 2014.

[27] R. Soref, 'The Past, Present, and Future of Silicon Photonics', *IEEE Journal of Selected Topics in Quantum Electronics*, vol. 12, no. 6, pp. 1678-1687, 2006.

[28] Q. Zhong, V. Veerasubramanian, Y. Wang, W. Shi, D. Patel, S. Ghosh, A. Samani, L. Chrostowski, R. Bojko, and D. V. Plant, “Focusing-curved subwavelength grating couplers for ultra-broadband silicon photonics optical interfaces,” Opt. Express 22(15), 18224-18231 (2014).

[29] N. Abadía, D. Xiangyang, Q. Lu, W. H. Guo, E. El-Fiky, D. V. Plant, and J. F. Donegan, “Novel polarization beam splitter based on p-i-n structure for an indium phosphide platform,” in 2017 19th International Conference on Transparent Optical Networks (ICTON, 2017), paper Tu.A5.1.

[30] Y. Huang, S. Zhu, H. Zhang, T.-Y. Liow, and G.-Q. Lo, "CMOS compatible horizontal nanoplasmonic slot waveguides TE-pass polarizer on silicon-on-insulator platform," Opt. Express 21, 12790–12796 (2013).

[31] R. K. Gupta, S. Chandran, and B. K. Das, “Wavelength-independent directional couplers for integrated silicon photonics,” J. Light. Technol. 35(22), 4916–4923 (2017).

[32] H. Yun, W. Shi, Y. Wang, L. Chrostowski, and N. A. F. Jaeger, “2x2 adiabatic 3-dB coupler on silicon-on-insulator rib waveguides,” Proc. SPIE 8915, 89150V (2013).

[33] J. Xing, Z. Li, Y. Yu, and J. Yu, “Design of polarization-independent adiabatic splitters fabricated on silicon-on-insulator substrates,” Opt. Express 21(22), 26729–26734 (2013).

[34] Y. Wang, W. Shi, X. Wang, Z. Lu, M. Caverley, R. Bojko, L. Chrostowski, and N. A. F. Jaeger, “Design of broadband subwavelength grating couplers with low back reflection,” Opt. Lett. 40(20), 4647–4650 (2015).

[35] A. Ortega-Moñux, L. Zavargo-Peche, A. Maese-Novo, I. Molina-Fernández, R. Halir, J. G. Wangüemert-Pérez, P. Cheben, and J. H. Schmid, “High-performance multimode interference coupler in silicon waveguides with subwavelength structures,” IEEE Photonics Technol. Lett. 23(19), 1406–1408 (2011).

[36] R. A. Soref, “All-silicon active and passive guided-wave components for λ = 1.3 and 1.6 µm,” IEEE J. Quantum Electron. 22(6), 873-879 (1986).

[37] H. Chen, P. Verheyen, P. De Heyn, G. Lepage, J. De Coster, S. Balakrishnan, P. Absil, W. Yao, L. Shen, G. Roelkens and J. Van Campenhout, "−1 V bias 67 GHz bandwidth Si-contacted germanium waveguide p-i-n photodetector for optical links at 56 Gbps

and beyond," Optics Express 24, 4622 (2016).

[38] S. Lischke, D. Knoll, C. Mai, L. Zimmermann, A. Peczek, M. Kroh, A. Trusch, E. Krune, K. Voigt, and A. Mai, “High bandwidth, high responsivity waveguide coupled germanium p-i-n photodiode,” Optics Express, vol. 23, pp. 27213–27220, October 2015.

[39] G. Li, Y. Luo, X. Zheng, G. Masini, A. Mekis, S. Sahni, H. Thacker, J. Yao, I. Shubin, K. Raj, et al., “Improving CMOS-compatible germanium photodetectors,” Optics Express, vol. 20, pp. 26345–26350, November 2012.

[40] A. Novack, M. Gould, Y. Yang, Z. Xuan, M. Streshinsky, Y. Liu, G. Capellini, A. E.-J. Lim, G.-Q. Lo, T. Baehr-Jones, et al., “Germanium photodetector with 60 GHz bandwidth using inductive gain peaking,” Optics Express, vol. 21, pp. 28387–28393, November 2013.

[41] M. Moayedi Pour Fard, C. Williams, G. Cowan, and O. Liboiron-Ladouceur, “High-speed grating-assisted all-silicon photodetector for 850 nm applications,” Optics Express, vol. 25, no. 5, pp. 5107-5118, March 2017.

[42] M. Moayedi Pour Fard, G. Cowan, and O. Liboiron-Ladouceur, “Responsivity optimization of a high-speed germanium-on-silicon photodetector,” Optics Express, vol. 24, no. 24, pp. 27738-27752, November 2016.

[43] C. Doerr, L. Buhl, Y. Baeyens, R. Aroca, S. Chandrasekhar, X. Liu, L. Chen and Y. Chen, "Packaged Monolithic Silicon 112-Gb/s Coherent Receiver," IEEE Photonics Technology Letters 23, 762-764 (2011).

[44] J. Verbist, J. Zhang, B. Moeneclaey, W. Soenen, J. Van Weerdenburg, R. Van Uden, C. Okonkwo, J. Bauwelinck, G. Roelkens and X. Yin, "A 40-GBd QPSK/16-QAM

Integrated Silicon Coherent Receiver," IEEE Photonics Technology Letters 28, 2070-2073 (2016).

[45] H. Zhu, L. Zhou, T. Wang, L. Liu, C. Wong, Y. Zhou, R. Yang, X. Li and J. Chen, "Optimized Silicon QPSK Modulator With 64-Gb/s Modulation Speed," IEEE Photonics Journal 7, 1-6 (2015).

[46] P. Dong, C. Xie, L. Chen, L. Buhl and Y. Chen, "112-Gb/s monolithic PDM-QPSK modulator in silicon," Optics Express 20, B624 (2012).

[47] A. Shastri, C. Muzio, M. Webster, G. Jeans, P. Metz, S. Sunder, B. Chattin, B. Dama and K. Shastri, "Ultra-Low-Power Single-Polarization QAM-16 Generation Without DAC Using a CMOS Photonics Based Segmented Modulator," Journal of Lightwave Technology 33, 1255-1260 (2015).

[48] J. Lin, H. Sepehrian, L. A. Rusch and W. Shi, "CMOS-Compatible Silicon Photonic IQM for 84 Gbaud 16QAM and 70 Gbaud 32QAM," 2018 Optical Fiber Communications Conference and Exposition (OFC), San Diego, CA, 2018, pp. 1-3.

[49] Z. Wang, Y. Gao, J. Cartledge, E. Huante-Ceron, D. Logan and A. Knights, "DSP-Enabled 104-Gb/s 16-QAM Nyquist Subcarrier Modulation Using a Silicon Micro-Ring Resonator," IEEE Photonics Technology Letters 30, 1571-1574 (2018).

[50] J. Ding, S. Shao, L. Zhang, X. Fu and L. Yang, "Silicon 16-QAM optical modulator driven by four binary electrical signals," Optics Letters 42, 1636 (2017).

[51] Po Dong, Xiang Liu, Chandrasekhar, S., Buhl, L.L., Aroca, R., Baeyens, Y., Young-Kai Chen, "224-Gb/s PDM-16-QAM modulator and receiver based on silicon photonic integrated circuits," *Optical Fiber Communication Conference and Exposition and the*

National Fiber Optic Engineers Conference (OFC/NFOEC), 2013 , vol., no., pp.1,3, 17-21 March 2013.

[52] A. Konczykowska, J. Dupuy, M. Riet, V. Nodjiadjim, F. Jorge, H. Aubry and A. Adamiecki, "84 GBd (168 Gbit/s) PAM-4 3.7 Vpp power DAC in InP DHBT for short reach and long haul optical networks", Electronics Letters, vol. 51, no. 20, pp. 1591-1593, 2015.

[53] I. G. López, P. Rito, L. Zimmermann, D. Kissinger and A. C. Ulusoy, "A 40 Gbaud SiGe:C BiCMOS driver for InP segmented MZMs with integrated DAC functionality for PAM-16 generation," 2016 IEEE MTT-S International Microwave Symposium (IMS), San Francisco, CA, 2016, pp. 1-4.

[54] R. Motaghiannezam, I. Lyubomirsky, H. Daghighian, C. Kocot, T. Gray, J. Tatum, A. Amezcua-Correa, M. Bigot-Astruc, D. Molin, F. Achten and P. Sillard, "Four 45 Gbps PAM4 VCSEL based transmission through 300 m wideband OM4 fiber over SWDM4 wavelength grid", Optics Express, vol. 24, no. 15, p. 17193, 2016.

[55] Jim A. Tatum, Deepa Gazula, Luke A. Graham, James K. Guenter, Ralph H. Johnson, Jonathan King, Chris Kocot, Gary D. Landry, Ilya Lyubomirsky, Andrew N. MacInnes, Edward M. Shaw, Kasyapa Balemarthy, Roman Shubochkin, Durgesh Vaidya, Man Yan, and Frederick Tang, "VCSEL-Based Interconnects for Current and Future Data Centers," J. Lightwave Technol. 33, 727-732 (2015).

[56] J. Zhou, C. Yu, and H. Kim, "Transmission Performance of OOK and 4-PAM Signals Using Directly Modulated 1.5-μm VCSEL for Optical Access Network," J. Lightwave Technol. Vol. 33, no. 15, pp. 3243-3249, 2015.

[57] C. Xie, S. Spiga, P. Dong, P. Winzer, M. Bergmann, B. Kögel, C. Neumeyr, and M.C. Amann, "400-Gb/s PDM-4PAM WDM System Using a Monolithic 2×4 VCSEL Array and Coherent Detection," J. Lightwave Technol. Vol. 33, no.3, pp. 670-677, 2015.

[58] A. Roshan-Zamir, B. Wang, S. Telaprolu, K. Yu, C. Li, M. A. Seyedi, M. Fiorentino, R. Beausoleil, and S. Palermo, "A two-segmented optical DAC 40 Gb/s PAM4 silicon microring resonator modulator transmitter in 65nm CMOS," in Proc. IEEE Opt. Interconnects Conf., May 2017, pp. 5–6.

[59] J. Sun, M. Sakib, J. Driscoll, R. Kumar, H. Jayatilleka, Y. Chetrit, and H. Rong, "A 128 Gb/s PAM4 Silicon Microring Modulator," in Optical Fiber Communication Conference Postdeadline Papers, pp. Th4A.7, San Diego, CA, USA, 2018.

[60] R. Li, D. Patel, E. El-Fiky, A. Samani, Z. Xing, M. Morsy-Osman, and D. V. Plant, "High-speed low-chirp PAM-4 transmission based on push-pull silicon photonic microring modulators," Opt. Express 25(12), 13222-13229 (2017).

[61] R. Li, D. Patel, E. El-Fiky, A. Samani, Z. Xing, L. Xu, and D. V. Plant, "A C-band push-pull dual-ring silicon photonic modulator for 20 km SSMF transmission without CD compensation," in *Conference on Lasers and Electro-optics* (Optical Society of America, 2017), paper SM2O.3.

[62] R. Li, D. Patel, A. Samani, E. El-Fiky, Y. Wang, Z. Xing, and D. V. Plant, "Analysis and experimental study of a silicon photonic single MRM-assisted MZI PAM-4 modulator," IEEE Photonics J. **9**(6), 4900607 (2017).

[63] R. Li, A. Samani, E. El-Fiky, D. Patel, Q. Zhong, and D. V. Plant, "56-Gbps OOK transmission using silicon microring assisted Mach-Zehnder interferometer," in

Conference on Lasers and Electro-optics (Optical Society of America, 2016), paper STu4G.4.

[64] R. Li, D. Patel, A. Samani, E. El-Fiky, Z. Xing, M. Sowailem, Q. Zhong and D. V. Plant, “An 80 Gb/s silicon photonic modulator based on the principle of overlapped resonances,” IEEE Photonics J. **9**(3), 4900311 (2017).

[65] R. Li, D. Patel, A. Samani, E. El-Fiky, Z. Xing, M. Morsy-Osman, and D. V. Plant, “Silicon photonic ring-assisted MZI for 50 Gb/s DAC-less and DSP-free PAM-4 transmission,” IEEE Photonics Technol. Lett. 29(12), 1046-1049 (2017).

[66] R. Li, D. Patel, E. El-Fiky, A. Samani**,** Z. Xing, Y. Wang and D. Plant, "Silicon photonic dual-drive MIM based 56 Gb/s DAC-less and DSP-free PAM-4 transmission", *Optics Express*, vol. 26, no. 5, p. 5395, 2018.

[67] J. Verbist, J. Lambrecht, M. Verplaetse, J. Van Kerrebrouck, A. Srinivasan, P. De Heyn, T. De Keulenaer, X. Yin, G. Torfs, J. Van Campenhout, G. Roelkens, and J. Bauwelinck, "DAC-Less and DSP-Free 112 Gb/s PAM-4 Transmitter Using Two Parallel Electroabsorption Modulators," *J. Lightwave Technol*. Vol. 36, no. 5, pp. 1281-1286, 2018.

[68] A. Abbasi, L. Abdollahi Shiramin, B. Moeneclaey, J. Verbist, X. Yin, J. Bauwelinck, D. V. Thourhout, G. Roelkens, and G. Morthier, "III–V-on-Silicon C-Band High-Speed Electro-Absorption-Modulated DFB Laser," *J. Lightwave Technol*. Vol. 36, no2, pp. 252-257, 2018.

[69] H. Zwickel, S. Wolf, C. Kieninger, Y. Kutuvantavida, M. Lauermann, T. de Keulenaer, A. Vyncke, R. Vaernewyck, J. Luo, A. K.-Y. Jen, W. Freude, J. Bauwelinck, S. Randel, and C. Koos, "Silicon-organic hybrid (SOH) modulators for intensity-

modulation / direct-detection links with line rates of up to 120 Gbit/s," *Opt. Express*, vol. 25, pp. 23784-23800, 2017.

[70] A. Samani, M. Chagnon, D. Patel, V. Veerasubramanian, S. Ghosh, M. Osman, Q. Zhong and D. Plant, “A Low-Voltage 35-GHz Silicon Photonic Modulator-Enabled 112-Gb/s Transmission System”, *IEEE Photonics* Journal, vol. 7, no. 3, pp. 1-13, 2015.

[71] A. Samani, "Design and Characterization of 35 GHz Silicon Photonic Travelling Wave Modulator for Next Generation Short Reach Communication Links", McGill University, 2015.

[72] A. Samani, V. Veerasubramanian, E. El-Fiky, D. Patel and D. V. Plant, "A Silicon Photonic PAM-4 Modulator Based on Dual-Parallel Mach–Zehnder Interferometers," *IEEE Photonics Journal*, vol. 8, no. 1, pp. 1-10, Feb. 2016.

[73] A. Samani, D. Patel, M. Chagnon, E. El-Fiky, R. Li, M. Jacques, N. Abadía, V. Veerasubramanian and D. Plant, "Experimental parametric study of 128 Gb/s PAM-4 transmission system using a multi-electrode silicon photonic Mach Zehnder modulator", *Optics Express*, vol. 25, no. 12, p. 13252, 2017.

[74] A. Samani, E. El-Fiky, M. Osman, R. Li, D. Patel, T. Hoang, M. Jacques, M. Chagnon, N. Abadía, and D. Plant, “Silicon Photonic Mach-Zehnder Modulator Architectures for on Chip PAM-4 Signal Generation and Transmission” *Journal of Lightwave Technology*, (Submitted, Manuscript ID: JLT-22637-2018, July 4th, 2018). (Invited).

[75] A. Samani, E. El-Fiky, M. Osman, D. Patel, M. Jacques, R. Li, D. Plant. “180 Gb/s Single Carrier Single Polarization 16-QAM Transmission using an O-Band Silicon

Photonic IQM" *Optics Express*, (Submitted, Manuscript ID: 346077, September 30th, 2018).

[76] Z. Xing, A. Samani, M. Xiang, E. El-Fiky, T. Hoang, D. Patel, R. Li, M. Qiu, M. Saber, M. Morsy-Osman and D. Plant, "100 Gb/s PAM4 transmission system for datacenter interconnects using a SiP ME-MZM based DAC-less transmitter and a VSB self-coherent receiver", *Optics Express*, vol. 26, no. 18, p. 23969, 2018.

[77] A. Samani, M. Chagnon, E. Elfiky, D. Patel, M. Jacques, V. Veerasubramanian, and D. Plant, "Silicon Photonics Modulator Architectures for Multi-Level Signal Generation and Transmission," 2017 Optical Fiber Communications Conference and Exposition (OFC), paper Tu2H.4. Los Angeles, CA, USA. (Top Scored).

[78] A. Samani, D. Patel, S. Ghosh, V. Veerasubramanian, Q. Zhong, W. Shi, D. V Plant, "OOK and PAM optical modulation using single drive push pull silicon Mach-Zehnder modulator", International Group IV Photonics Conference, 27 – 29 August 2014, Paris, France.

[79] D. Patel, A. Samani, V. Veerasubramanian, S. Ghosh and D. V. Plant, "Silicon Photonic Segmented Modulator-Based Electro-Optic DAC for 100 Gb/s PAM-4 Generation," *IEEE Photonics Technology Letters*, vol. 27, no. 23, pp. 2433-2436, Dec.1, 1 2015.

[80] D. Patel, S. Ghosh, M. Chagnon, A. Samani, V. Veerasubramanian, M. Osman and D. Plant, 'Design, analysis, and transmission system performance of a 41 GHz silicon photonic modulator', *Optics Express*, vol. 23, no. 11, p. 14263, 2015.

[81] M. Streshinsky, R. Ding, Y. Liu, A. Novack, Y. Yang, Y. Ma, X. Tu, E. Koh Sing Chee, A. Eu-Jin Lim, P. Guo-Qiang Lo, T. Baehr-Jones, and M. Hochberg, "Low power 50

Gb/s silicon traveling wave Mach-Zehnder modulator near 1300 nm," Opt. Express, vol. 21, no. 25, pp. 30350-30357, 2013.

[82] P. Dong, L. Chen, and Y. Chen, “High-speed low-voltage single-drive push–pull silicon Mach–Zehnder modulators,” Opt. Exp., vol. 20, no. 6, pp. 6163–6169, Mar. 2012.

[83] Y. Ehrlichman, O. Amrani and S. Ruschin, "Improved Digital-to-Analog Conversion Using Multi-Electrode Mach–Zehnder Interferometer," J. Lightwave Technol, vol. 26, pp. 3567-3575, 2008.

[84] Hongtao Chen, M. Galili, P. Verheyen, P. De Heyn, G. Lepage, J. De Coster, S. Balakrishnan, P. Absil, L. Oxenlowe, J. Van Campenhout, and G. Roelkens, "100-Gbps RZ Data Reception in 67-GHz Si-Contacted Germanium Waveguide p-i-n Photodetectors," J. Lightwave Technol. 35, 722-726 (2017).

[85] M. Chagnon, M. Morsy-Osman, M. Poulin, C. Latrasse, J.-F. Gagné, Y. Painchaud, C. Paquet, S. Lessard, and D. V. Plant, “Experimental study of 112 Gb/s short reach transmission employing PAM formats and SiP intensity modulator at 1.3 μm,” Opt. Express, vol. 22, no. 17, pp. 21 018–21 036, Aug 2014.

[86] M. Chagnon, M. Morsy-Osman, M. Poulin, C. Paquet, S. Lessard, and D. V. Plant, “Experimental parametric study of a silicon photonic modulator enabled 112 Gb/s PAM transmission system with a DAC and ADC,” J. Lightw. Technol., vol. 33, no. 7, pp. 1380–1387, April 2015.

[87] M. Poulin, C. Latrasse, J.-F. Gagné, Y. Painchaud, M. Cyr, C. Paquet, M. Morsy-Osman, M. Chagnon, S. Lessard, and D. V. Plant, “107 Gb/s PAM-4 transmission over 10 km using a SiP series push-pull modulator at 1310 nm,” *The European Conference*

on Optical Communication (ECOC), Cannes, 2014, pp. 1-3.

[88] M. Chagnon, S. Lessard, and D. V. Plant, “107 Gb/s PAM-4 transmission over 10 km using a SiP series push-pull modulator at 1310 nm,” in Proc. Of European Conference on Optical Communication, Sept 2014, paper Mo.4.5.3, pp. 1–3.

[89] R. Soref and B. Bennett, “Electrooptical effects in silicon”, *IEEE J. Quantum Electron.*, vol. 23, no. 1, pp. 123-129, 1987.

[90] K. Bédard, A. D. Simard, B. Fillion, Y. Painchaud, L. A. Rusch, and S. LaRochelle, “Dual phase-shift Bragg grating silicon photonic modulator operating up to 60 Gb/s,” Opt. Express 24(3), 2413-2419 (2016).

[91] R. Dubé-Demers, S. LaRochelle, and W. Shi, "Low-power DAC-less PAM-4 transmitter using a cascaded microring modulator," Opt. Lett. Vol. 41, no. 22, pp. 5369-5372, 2016.

[92] L. Chrostowski, and M. Hochberg, Silicon Photonics Design: From Devices to Systems (Cambridge University, 2015).

[93] Xi Xiao, Hao Xu, Xianyao Li, Zhiyong Li, Tao Chu, Yude Yu, and Jinzhong Yu, "High-speed, low-loss silicon Mach–Zehnder modulators with doping optimization," Opt. Express 21, 4116-4125 (2013).

[94] Hui Yu, Marianna Pantouvaki, Joris Van Campenhout, Dietmar Korn, Katarzyna Komorowska, Pieter Dumon, Yanlu Li, Peter Verheyen, Philippe Absil, Luca Alloatti, David Hillerkuss, Juerg Leuthold, Roel Baets, and Wim Bogaerts, “Performance tradeoff between lateral and interdigitated doping patterns for high speed carrier-depletion based silicon modulators,” Opt. Express 20, 12926-12938 (2012).

[95] D. Perez-Galacho, L. Bramerie, C. Baudot, M. Chaibi, S. Messaoudene, N. Vulliet, L.

Vivien, F. Boeuf, C. Peucheret and D. Marris-Morini, "QPSK Modulation in the O-Band Using a Single Dual-Drive Mach–Zehnder Silicon Modulator," Journal of Lightwave Technology 36, 3935-3940 (2018).

[96] Y. Zhang, S. Yang, A. Lim, G. Lo, C. Galland, T. Baehr-Jones and M. Hochberg, 'A compact and low loss Y-junction for submicron silicon waveguide', *Opt. Express*, vol. 21, no. 1, p. 1310, 2013.

[97] R. Ding, Y. Liu, Q. Li, Y. Yang, Y. Ma, K. Padmaraju, A. Lim, G. Lo, K. Bergman, T. Baehr-Jones and M. Hochberg, "Design and characterization of a 30-GHz bandwidth low-power silicon traveling-wave modulator," Optics Communications 321, 124-133 (2014).

[98] D. Patel, V. Veerasubramanian, S. Gosh, W. Shi, A. Samani and D. Plant, "A 4×4 fully non-blocking switch on SOI based on interferometric thermo-optic phase shifters," in Optical Interconnects Conference (2014).

[99] M. Jacques, A. Samani, D. Patel, E. El-Fiky, M. Morsy-Osman, T. Hoang, M. Saber, L. Xu, J. Sonkoly, M. Ayliffe and D. Plant, "Modulator material impact on chirp, DSP, and performance in coherent digital links: comparison of the lithium niobate, indium phosphide, and silicon platforms", Optics Express, vol. 26, no. 17, p. 22471, 2018.

[100] A. Aimone, I. G. Lopez, S. Alreesh, P. Rito, T. Brast, V. Höhns, G. Fiol, M. Gruner, J. K. Fischer, J. Honecker, A. G. Steffan, D. Kissinger, A. C. Ulusoy, and M. Schell, "DAC-free Ultra-Low-Power Dual-Polarization 64-QAM Transmission with InP IQ Segmented MZM Module," in Optical Fiber Communication Conference Postdeadline Papers, OSA Technical Digest (online) (Optical Society of America, 2016), paper Th5C.6.

[101] Hiroshi Yamazaki, Akihide Sano, Munehiko Nagatani, and Yutaka Miyamoto, "Single-carrier 1-Tb/s PDM-16QAM transmission using high-speed InP MUX-DACs and an integrated OTDM modulator," Opt. Express 23, 12866-12873 (2015).

[102] H. Zhu, L. Zhou, T. Wang, L. Liu, C. Wong, Y. Zhou, R. Yang, X. Li and J. Chen, "Optimized Silicon QPSK Modulator With 64-Gb/s Modulation Speed," IEEE Photonics Journal 7, 1-6 (2015).

[103] Y. Ehrlichman, O. Amrani, and S. Ruschin, "Improved Digital-to-Analog Conversion Using Multi-Electrode Mach–Zehnder Interferometer," J. Lightwave Technol., vol.26, no.21, pp. 3567–3575 , 2008.

[104] B. Masella and X. Zhang, 'Linearized optical single sideband Mach-Zehnder electro-optic modulator for radio over fiber systems', Opt. Express, vol. 16, no. 12, p. 9181, 2008.

[105] M. Streshinsky, A. Ayazi, Z. Xuan, A. Lim, G. Lo, T. Baehr-Jones and M. Hochberg, 'Highly linear silicon traveling wave Mach-Zehnder carrier depletion modulator based on differential drive', Opt. Express, vol. 21, no. 3, p. 3818, 2013.

[106] B. Mao, P. Yue, F. Hou and Z. Liu, 'Highly linear dual parallel Mach-Zehnder modulator incorporating MMI couplers', JEOS, RP, vol. 10, 2015.

[107] M. Streshinsky, R. Ding, Y. Liu, A. Novack, Y. Yang, Y. Ma, X. Tu, E. Chee, A. Lim, P. Lo, T. Baehr-Jones and M. Hochberg, 'Low power 50 Gb/s silicon traveling wave Mach-Zehnder modulator near 1300 nm', Opt. Express, vol. 21, no. 25, p. 30350, 2013.

[108] F. Devaux, Y. Sorel and J. Kerdiles, 'Simple measurement of fiber dispersion and of chirp parameter of intensity modulated light emitter', J. Lightwave Technol., vol. 11, no. 12, pp. 1937-1940, 1993.

[109] I. Kaminow, T. Li and A. Willner, Optical Fiber Telecommunications Volume VIA. Burlington: Elsevier Science, 2013.

[110] M. Scholten, T. Coe and J. Dillard, 'Continuously-interleaved BCH (CI-BCH) FEC delivers best in class NECG for 40G and 100G metro applications',2010 Optical Fiber Communication (OFC), San Diego, CA, 2010.

[111] E. El-Fiky, M. Chagnon, M. Sowailem, A. Samani, M. Morsy-Osman and D. Plant, "168 Gb/s Single Carrier PAM4 Transmission for Intra Data Center Optical Interconnects," IEEE Photonics Technology Letters, 29, 3, 314-317, (2017).

[112] G. Agrawal, Fiber-optic communication systems. Hoboken, N.J.: Wiley, 2013.

[113] T. Baehr-Jones, R. Ding, Y. Liu, A. Ayazi, T. Pinguet, N. C. Harris, M. Streshinsky, P. Lee, Y. Zhang, A. Eu-Jin Lim, T. Y. Liow, S. Hwee-Gee Teo, G. Q. Lo, and M. Hochberg, "Ultralow drive voltage silicon traveling-wave modulator," Opt. Express, vol. 20, no. 11, pp. 12014-12020, 2012.

[114] Z. Yong, S. Shopov, J. C. Mikkelsen, R. Mallard, J. C. C. Mak, J. Jeong, S. P. Voinigescu, and J. K. S. Poon, "RF and Thermal Considerations of a Flip-Chip Integrated 40+ Gb/s Silicon Photonic Electro-Optic Transmitter," J. Lightwave Technol, vol. 36, pp. 245-251, 2018.

[115] D. Miller, "Device Requirements for Optical Interconnects to Silicon Chips," Proceedings of the IEEE 97, 1166-1185 (2009).

[116] C. Chen, X. Tang, and Z. Zhang, "Transmission of 56-Gb/s PAM-4 over 26-km Single Mode Fiber Using Maximum Likelihood Sequence Estimation," in Optical Fiber Communication Conference, OSA Technical Digest (online) (Optical Society of America, 2015), paper Th4A.5.

[117] J. Zhang, J. Yu, J. Shi and H. Chien, "Digital Dispersion Pre-Compensation and Nonlinearity Impairments Pre- and Post-Processing for C-Band 400G PAM-4 Transmission over SSMF Based on Direct-Detection," 2017 European Conference on Optical Communication (ECOC), Gothenburg, 2017, pp. 1-3.

[118] Haik Mardoyan, Miquel A. Mestre, Jose Manuel Estarán, Filipe Jorge, Fabrice Blache, Philippe Angelini, Agnieszka Konczykowska, Muriel Riet, Virginie Nodjiadjim, Jean-Yves Dupuy, and Sebastien Bigo, "84-, 100-, and 107-GBd PAM-4 Intensity-Modulation Direct-Detection Transceiver for Datacenter Interconnects," J. Lightwave Technol. 35, 1253-1259 (2017)

[119] M. Ghioni, A. Gulinatti, I. Rech, F. Zappa and S. Cova, "Progress in Silicon Single-Photon Avalanche Diodes", IEEE Journal of Selected Topics in Quantum Electronics, vol. 13, no. 4, pp. 852-862, 2007.

[120] K. Morse, R. Abraham, A. DeAbreu, C. Bowness, T. Richards, H. Riemann, N. Abrosimov, P. Becker, H. Pohl, M. Thewalt and S. Simmons, "A photonic platform for donor spin qubits in silicon", Science Advances, vol. 3, no. 7, p. e1700930, 2017.

[121] M. Akhlaghi, E. Schelew and J. Young, "Waveguide integrated superconducting single-photon detectors implemented as near-perfect absorbers of coherent radiation", Nature Communications, vol. 6, no. 1, 2015.

[122] S. Dorenbos, P. Forn-Díaz, T. Fuse, A. Verbruggen, T. Zijlstra, T. Klapwijk and V. Zwiller, "Low gap superconducting single photon detectors for infrared sensitivity", Applied Physics Letters, vol. 98, no. 25, p. 251102, 2011.

[123] J. A. Richardson, L. A. Grant and R. K. Henderson, "Low Dark Count Single-Photon Avalanche Diode Structure Compatible With Standard Nanometer

Scale CMOS Technology," in *IEEE Photonics Technology Letters*, vol. 21, no. 14, pp. 1020-1022, July15, 2009.